Characterising nanoparticles by lattice vibration frequency

Kieran Homewood-Stone

Masters by Research: Chemistry

Supervisor: Dr Dean Sayle

Date of Submission: 22/09/2020

Student ID: 17904964

Word/Page Count: 20375/44

Abstract

In this study, we simulate that irradiation of nanoceria has potential inducing (breathing mode) lattice vibrations. Irradiation therefore has potential to be used in increasing the catalytic activity of nanoceria structures. If irradiation can be implemented to vibrate atoms off their lattice sites, in a similar manner to temperature, this would enable surface atoms to be more easily extracted. Extracted surface oxygen has potential uses in oxidative catalysis or to modulate oxygen concentration in biological environments with nanoceria as a nanozyme.

Here, Molecular Dynamics (MD) simulation was used to calculate vibration (breathing mode) frequencies of various ceria nanoparticles. Vibration was induced in polyhedral nanoparticles, 665 – 6708 cerium atoms in size, and compared to the vibrations induced in nanocylinders comprising 653 – 6721 cerium atoms. The simulations revealed that breathing mode frequencies decrease with increasing size for both polyhedral and cylindrical nanoparticles in accord with experiment. The simulations also revealed that breathing mode frequencies depend upon the aspect ratio of nanocylinders. The simulations suggest that breathing mode vibrational spectra can be used as a fingerprint to identify the size, shape, and aspect ratio distribution of a ceria nanomaterial sample.

Contents

Acknowledgements

I would like to express my gratitude to my supervisor, Dr Dean Sayle, for accepting me on this research degree as well as for all his support and guidance throughout my master's degree. Nanoparticle simulation was a completely new field of study to me at the beginning of my degree, however with Dean's guidance and experience it has become an area of great interest to me that I have thoroughly enjoyed studying.

I would also like to express my gratitude to Dr Gavin Mountjoy for his assistance with the Fourier Transform analysis data obtained within this study. His demonstration and knowledge of the Fourier Transform analysis method was incredibly interesting and useful.

1. Introduction

1.1 Cerium Oxide Nanoparticles

Nanoparticles are an area of high interest in terms of scientific research. Cerium oxide has properties as an oxidising and reducing agent in catalysis which stems from cerium's ability to switch between two oxidation states, these states being Ce^{3+} and Ce^{4+}. These properties provide versatility for cerium oxide nanoparticles to be used in both oxidation and reduction reactions which provides purpose in a variety of fields such as catalytic converters in the automotive industry[1] or nanomedicine[2] in the medical field.

The ability of cerium to switch between two oxidation states is what provides cerium oxide with oxidising and reducing properties. One factor affecting whether the nanoparticle acts as an oxidiser or reducer is the Ce^{3+}/Ce^{4+} ratio on the surface of the nanoparticle. In environments where an oxidation reaction is required, oxygen can be removed from the cerium oxide nanoparticle; this creates oxygen vacancies within the nanoparticle surface which are stabilised by an increase in Ce^{3+} ions to maintain charge neutrality. Alternatively, if the environment has a high concentration (oxygen partial pressure) of oxygen present and a reduction reaction is required these oxygen vacancies can be filled causing an increase in Ce^{4+} ions. The areas of a cerium oxide nanoparticle surface where these oxygen vacancies are produced and filled are known as the catalytically active sites.

A study conducted by Tarnuzzer et al.[3] investigated the use of engineered ceria nanoparticles as a means of cell protection during radiation therapy within cancer treatment. They reported that the ceria nanoparticles provided a 99% protection of cell death from radiation for healthy cells compared to no protection for tumour cells. They attributed this result to a potential antioxidant property of ceria nanoparticles eliminating free radicals at target sites caused by shifting of oxidation state of cerium from Ce^{3+} to Ce^{4+}, these target sites being more numerous in tumour cells when compared to healthy cells.

The capability to store oxygen during oxygen rich environments and release this stored oxygen in oxygen lean environments is known as a material oxygen storage capacity (OSC). Research into the area has discovered that a material OSC is affected by a variety of factors such as the surface to volume ratio, the surface planes available for interaction during catalysis, the defects present within the material and the cerium oxygen bond length.

1.2 Molecular Vibration

The vibration of an atom can be augmented through the energy present within a medium, introduction of energy into the system increases that vibration whereas removal of energy will reduce the vibration of the atom. This vibration passes into the surrounding atoms and molecules allowing the energy to propagate through the medium. In technical terms, vibration is the mechanical form of repetitive variation between two or more states. These may be regular repeating across a timeframe known as periodic vibration or random. Commonly when thinking of vibration and waves, initial thoughts would be of sounds waves. In the case of sound waves, the energy vibrates molecules in the air allowing the sound wave to travel through it.

The vibration of molecules forms the basis for several analysis techniques for identifying unknown compounds such as Infrared spectroscopy and Raman spectroscopy being two of the most common. In the case of infrared spectroscopy, the vibration of molecular bonds can be induced through the introduction of non-destructive radiation, this radiation is absorbed causing vibration that occurs at different frequencies dependent on the type of bond vibration taking place, such as bending, stretching or rotation.

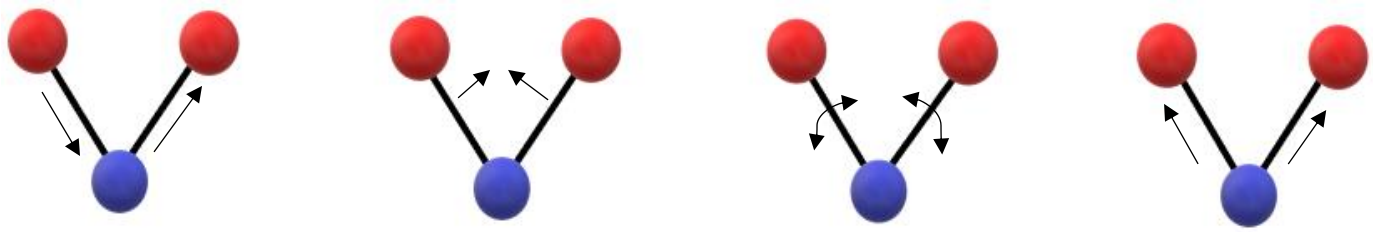

Fig 1. Examples of bond vibrations that occur during Infrared Spectroscopy. (Left to right) asymmetric stretching, scissoring bend, rotation, and symmetrical stretching. Symmetrical stretching is the vibration pattern present within breathing modes and is the only one of the four to not be visible using Infrared spectroscopy but are visible using Raman spectroscopy.

Research conducted into the frequency of vibrations caused by the different functional groups has led to the production of databases on the higher frequency molecular vibrations. These databases can be used as comparison to identify unknown compounds as well as deduce the properties of that compound. In recent years, more research has been performed into lower frequency molecular vibrations such as the breathing modes of nanoparticles.

1.3 Breathing Modes

Breathing modes are a type of molecular vibration within nanoparticles; it involves the symmetrical expansion and contraction of the atoms within a nanoparticle in every direction known as a radial breathing mode due to the radial direction of the vibration. Breathing modes occur in more than just spherical nanoparticles, every shape of nanoparticle has its own radial breathing mode.

A review by Ghavanloo et al.[4] summarised research into the radial breathing modes of a variety of nanoparticles with different geometries such as carbon nanotubes and nanowires. Many of the breathing modes obtained within the studies are identified using Raman spectroscopy which is due to the nature of breathing modes being a symmetrical vibration meaning Infrared spectroscopy would not work.

Infrared spectroscopy relies on a change in dipole moment created by the vibration of the molecule and changes in bond length using the equation:

$$\frac{\partial \mu}{\partial x} \neq 0 \qquad \textit{(Equation 1)}$$

In this equation ‘∂μ’ is the change in dipole moment, and ‘∂x’ is the change in motion of the vibration mode, for a vibrational mode to be infrared active, the value must be ‘not zero’. In the case of cerium oxide, the linear structure of the molecules means that during symmetrical vibration of the breathing mode, a dipole moment is not created. Therefore, the breathing mode vibrations of cerium oxide nanoparticles are not infrared active and cannot be observed using infrared spectroscopy.[5]

The production of perfectly symmetrical nanoparticles is unrealistic due the production of various surface planes upon the nanoparticle during crystallization. Due to the production of these surface planes and their effect on the nanoparticle shape, the perfectly symmetrical vibration of a nanoparticle is also unrealistic. Therefore, the breathing modes observed within this study are more closely related to quasi-breathing modes observed by Sauceda et al.[6] which are the closest vibration to that of breathing mode vibrations. These quasi-breathing modes are inherently more common within cylindrical nanoparticles as their dimensions are not equal meaning that the vibration travels further along one axis than another. As these vibrations are not symmetrical, they can be activated and observed through infrared excitation.

Raman spectroscopy works at lower frequencies through the scattering of light. A photon excites the compound under examination causing it to vibrate and change into a different vibration state, it then ejects a scattered photon. The energy of the scattered photon will be dependent on the new vibrational state, if the new state is of higher energy then the scattered photon will be of a lower frequency to

maintain the total energy of the system. However, if the new state is of lower energy then the scattered photon will be of a higher frequency. Comparison of the scattered photon frequency with a database of known frequency values allows the identification of the unknown compound.

1.4 Size and Shape Effects

The size and shape of a nanoparticle can influence various properties such as the catalytic capabilities[7-13], optical properties[14], melting and recrystallisation that have an impact on the purposes and uses for that nanoparticle. Xu et al.[7] investigated the effect of nanoparticle shape on the catalytic activity of silver nanoparticles. They compared truncated triangular, cubic and near spherical silver nanoparticles and they concluded that the rate of reaction produced by cubic silver nanoparticles is considerably quicker than that produced by the truncated triangular and near spherical silver nanoparticles.

Haruta et al.[8] investigated the size effect of different sized gold nanoparticles deposited on a metal oxide surface. They studied the effect of the nanoparticle size on its catalytic capabilities as a support for oxidation and reduction in the combustion of CO and various other hydrocarbons. They observed an increase in the reactive properties of the previously low reactive gold when it was implemented as nanoparticles. They attributed this increase in reactivity to the production of defects and more reactive planes during downsizing, as opposed to the (111) and (110) planes more commonly in bulk gold.

Current methods of establishing the size and shape of unknown nanoparticles can be expensive and time consuming. Accordingly, vibrational, breathing mode, frequencies of unknown nanoparticles offer a relatively quick and inexpensive method of nanomaterial characterisation.

Choi et al.[15] investigated the effect of particle size on the Raman spectra of titanium oxide nanoparticles. They examined two nanoparticle sizes - 30 nm and 12 nm - and observed both broadening and a shift in the Raman bonds with decreasing particle size. This suggests an influence of particle size on the vibration frequencies of nanoparticles.

Catalytic activity is partially dependent on the atom sites present on the surface of the nanostructure. It is possible that the shifting of atoms from their original lattice sites during vibration, could impact on the catalytic capabilities of that nanostructure. These vibration states can also provide insight into the bond strengths and therefore the formation energy required in vacancy production and in turn the production of potentially reactive surfaces involved in catalysis.

Nanorods have an interesting property that their length can be of a different value from their width or radius in the case of cylindrical nanorods. Whereas with cubic and spherical nanoparticles the length, width and height will be of equal value, nanorods add an additional variable. The aim of this study is to investigate how the length and aspect ratio of cylindrical nanorods affects the vibration frequency of these nanorods using computer modelling and molecular dynamics simulations.

2. Literature Review: Nanoparticles

The surface area to volume ratio is much higher for nanoparticles, this ratio increases as the size of the nanoparticle decreases. Factors such as size, shape and composition potentially have a greater impact at the nanoscale than bulk material, especially factors such as surface planes. These properties are what make nanoparticles an area of high research interest.

The increased effect of size, shape, composition, and surface planes makes nanoparticles versatile for a wide range of processes dependent on the composition of that nanoparticle such as nanomedicines, catalysis agents, fuel cells, and sensors.

2.1 Cerium Oxide and Applications

Research conducted on cerium oxide has led to the identification of many of its useful properties such as its ability to both oxidise and reduce; this has led to its use in many different areas of industry. The ability of cerium oxide to uptake and release oxygen in high temperature environments has led to its use in catalytic processes. This ability is produced by cerium's property to switch between oxidation state which allows the production of oxygen vacancies upon the surface of the nanoparticle as well as the filling of these vacancies.

2.1.1 Automotive Industry

One common place to find nanoparticles is in the automotive industry[16, 17]. The combustion of fuel in automotive is incomplete due to the limitations of oxygen flow and produces harmful by-products, the main three being: hydrocarbons (HC), carbon monoxide (CO) and nitric oxide (NO)[18].

Reaction of incomplete fuel combustion:

$$C_8H_{18} + 19\frac{1}{2}O_2 + N_2 \rightarrow 8CO + 2NO + 9H_2O \qquad \textit{(Equation 2)}$$

Initial catalytic converters were made up of two phases, an initial phase of Platinum (Pt) and Rhodium (Rh). This Pt/Rh phase plays the role of neutralising the NO product into N_2. A second oxidation catalyst plays the role of converting the excess CO and HC into the less harmful CO_2 and H_2O[19].

Modern catalytic converters are known as three-way catalysts (TWC), one material neutralises all three harmful by-products of combustion. This is usually achieved through an initial layer of Pt/Rh or similar material layer on top of an oxidising framework such as cerium oxide. The addition of cerium oxide has many advantages; it aids the stabilisation of alumina surface at high temperatures and the distribution of the Pt/Rh layer across the surface. Cerium oxide has the ability to switch between Ce(III) and Ce(IV) oxidation states through the release and absorption of oxygen. This ability makes cerium oxide useful in a three-way catalyst by allowing it to release oxygen when exhaust fumes are rich and store it when fumes are lean. The oxidation and redox reactions are as follows:

Oxidation

$$2CeO_2 + CO \rightarrow Ce_2O_3 + CO_2 \qquad \textit{(Equation 3)}$$

Redox

$$Ce_2O_3 + \frac{1}{2}O_2 \rightarrow 2CeO_2 \qquad \textit{(Equation 4)}$$

The amount of oxygen that can be absorbed by a material is its oxygen storage capacity (OSC). This controls the oxidation and redox reactions and affects the catalytic capabilities of the material.

2.1.2 Nanomedicine

The research of nanoparticles can also be found in the field of nanomedicine, the use of nanoparticles in the treatment of cancer cells and cell repair is under heavy research. Gold nanoparticles are one of the most common types of nanoparticle used in nanomedicine research; however, advancements in the use of other types of nanoparticle such as cerium oxide still take place[20].

A study conducted by Xu et al.[2] into the effect of cerium nanoparticles as a countermeasure for radiation induced lung injury in mice investigated the lung injury caused to mice by radiation through a sample of mice administered with a high dose of cerium nanoparticles and a sample of mice with a low dose of cerium nanoparticles being compared to a control group of mice with no cerium nanoparticles and found an increase in survival rate for mice exposed to cerium nanoparticles. They attributed this increase in survival rate to the elimination of free radical properties of cerium nanoparticles created through the change in oxidation states and oxygen defects found on the surface of these nanoparticles.

The production of Reactive Oxygen Species (ROS) is a by-product of regular cell metabolism, however these can be damaging to the cells as they have been linked to damage in the cell DNA causing mutations such as strand breaks or incomplete replication. As such it has been increasingly suggested that ROS may be a source for the production of cancer cells within the body[21, 22]. Cancer cells exhibit an increased presence of ROS to compensate for an increased metabolic activity within the tumour cells. Some treatments focus on increasing the levels of the ROS past a threshold where they begin to damage the tumour cells as opposed to promoting growth leading to cell death[23]. However, other studies suggest that the elimination of the ROS is a more effective method.

A study by Xue et al.[24] reported that cerium oxide nanoparticles were effective in eliminating hydroxyl radicals through their antioxidation properties, they also found that there was a relationship between the nanoparticle size and the efficiency of hydroxyl elimination with the efficiency increasing as the nanoparticle size was decreased. Research into this antioxidant elimination has shown that other factors such as the nanoparticle coating[25] and the oxidation states of the cerium present can also affect the ROS elimination activity[26].

Dunnick et al.[26] tested gadolinium oxide doped cerium oxide nanoparticles on their ability to eliminate ROS. The doping limited the Ce^{3+} and Ce^{4+} transitions which was found to reduce the antioxidant properties of the cerium oxide, suggesting that the ability to switch between two oxidation states is a more important factor than the oxidation states present upon the surface of the nanoparticle.

2.1.3 Mechanical Planarization

Cerium oxide is widely used as a polishing agent of glass surfaces, industries such as electronics have a growing requirement for high quality glass surfaces for products such as computer chips. Cerium oxide powders have been implemented in eliminating surface impurities to produce these high-quality glass surfaces. Some studies into this area have suggested that the planarization is purely mechanical caused by the pressure of cerium oxide crystals on the surface along with surface impurities being washed away, whereas other studies suggested chemical interactions as an additional factor with Ce^{3+} ions playing a more active role in the planarization process than Ce^{4+} ions.

However, a study by Janos et al.[27] concluded that the crystallite structure size of the particles of cerium oxide influenced the efficiency of planarization. They reported that the removal rate was found to increase with an increase in crystallite structure size suggesting that the size and shape factors of cerium oxide additionally affect its role in mechanical planarization.

2.2 Nanoparticle Size, Shape and Composition

The size of a nanoparticle has an impact upon the properties of that nanoparticle. As the size is decreased, the surface to volume ratio of the nanoparticle increases. This property can be further tailored through the nanoparticle shape, with different shapes such as nanospheres exhibiting a higher surface to volume ratio than cubic nanoparticles. The shape of a nanoparticle also affects the surface planes present which can have a further impact on the ability to form oxygen vacancies upon the nanoparticle surface, which is fundamental for the OSC (Oxygen Storage Capacity) of that nanoparticle during oxidation and reduction processes.

Na et al.[28] investigated how tuning the size and shape can affect the catalytic capabilities, initially they tested how reducing the size of a nanoparticle affected the catalytic capabilities and found with a reduction in size there was an increase in active sites for catalysis. They then compared how spherical nanoparticles and nanorods converted CO as temperature was increased. They found that the nanorods converted CO more effectively than the spherical and cubic nanoparticles. At 150 °C, the CO conversion for nanorods was approximately 20% compared to 10% for spherical nanoparticles and 2% for cubic nanoparticles. This difference continued as the temperature increased to 250 °C, where the conversion for nanorods increased to 90%, 65% for spherical nanoparticles and approximately 6% for cubic nanoparticles.

Additionally, the composition of a nanoparticle can have an impact on its properties; the introduction of dopants into cerium oxide nanoparticles can affect its capabilities in catalysis. The addition of dopants influences the properties of the atoms already present; this can be through the bonding of cerium to oxygen or the production of vacancies

A study by Gupta et al.[29] investigated the addition of a dopant on the Oxygen Storage Capacity (OSC) of cerium oxide nanoparticles. They reported with the introduction of a doping agent the bond length was increased which led to an increased OSC. They found that the addition of an Mn dopant provided longer Mn – O bonds and increased the length of the Ce – O bonds. They reported an increased OSC from this increased bond length which was further supported by the addition of a Pd dopant which provided further increased bond length that also improved the OSC of the CeO_2 nanoparticles.

2.3 Surface Planes and Oxygen Vacancies

As stated, the ability of cerium ions to switch between Ce^{3+} and Ce^{4+} oxidation states within cerium oxide nanoparticles has an impact on the applications of these nanoparticles. Some of the factors that control the oxidation state of the cerium ions is the number of oxygen vacancies within the nanoparticles which in turn are controlled by the surface planes present.

The surface plane is the configuration that atoms sit upon the surface of a structure be this nanoparticle or bulk. For nanoparticles, each surface plane has different properties dependent on its stability and the atom configuration present.

A study by Conesa[30] found that different surface planes have different stabilities, these are shown in Fig 2. decreasing in stability from left to right:

$$(111) > (211) > (110) > (100)$$

←Stability

Fig 2. Order of surface plane stability as report by Conesa[30]. {211} surface naturally rearranged into a stepped {111} surface.

The surface planes that are exposed on a nanoparticle can be tuned by the shape of the nanoparticle produced. Cubic nanoparticles are entirely {100} surfaces, octahedral nanoparticles have two surfaces present of {111} and {100}[31] and nanorods possess {110} and {100} surfaces[30].

A review by Mullins[32] discussed the structure patterns of cerium oxide nanoparticles as well as the surface planes produced. Fully oxidised cerium oxide has a fluorite crystal structure with the cerium atoms filling FCC-like sites but not as tightly packed. Each cerium atom is bonded to eight oxygen atoms, and each oxygen atom is bonded to a further four cerium atoms. The surface structure and its stability are affected by the charges produced; these surfaces can be classified as per the works of Tasker[33]. For {111} surfaces each layer has an alternating charge with the repeating units leading to no net dipole moment being produced aiding with the stability of the surface, this is classified as a type 2 surface. For {110} surfaces there is zero charge on each layer, these surfaces are classified as type 1 surfaces. Finally, {100} surfaces have alternating charges on each layer similar to {111} surfaces however the repeating units are unsymmetrical leading to an overall net dipole moment being produced reducing stability of the surface. This makes the {100} surface an example of a type 3 surface.

Zhou et al.[34] synthesized a sample of cerium oxide nanoparticles, these nanoparticles consisted of nanorods with sizes ranging from lengths of 100 – 300nm and diameter of 13 – 20nm and irregular nanoparticles with an average diameter of 8nm. Using High-resolution Transmission Electron Microscopy (HRTEM) they studied the surface plane structure of these nanoparticles observing that the nanoparticles produced predominantly {111} or a mix of {111} and {001} surface planes whereas the nanorods produced predominantly {001} and {110} surface planes. Using temperature programmed reduction (TPR) with H_2 they observed that the nanoparticles were more active than nanorods however due to a reduced redox capacity this increased activity was limited and reduced over time. Comparatively they observed that for CO conversion the nanorods displayed a higher activity and oxidation rate than the nanoparticles with one suggestion for this being due to oxygen storage capacity of the surface planes predominantly produced by each shape.

The amount of oxygen vacancies found within the nanoparticles affects the catalytic properties of that nanoparticle. These vacancies improve the catalytic capabilities of the nanoparticle through the ability of these vacancies to move throughout the nanoparticle. This allows oxygen atoms to move towards the surface of the nanoparticle in environments where there is low oxygen, and then in environments where there is a high concentration of oxygen these atoms can be transferred through the structure allowing the uptake of more oxygen.

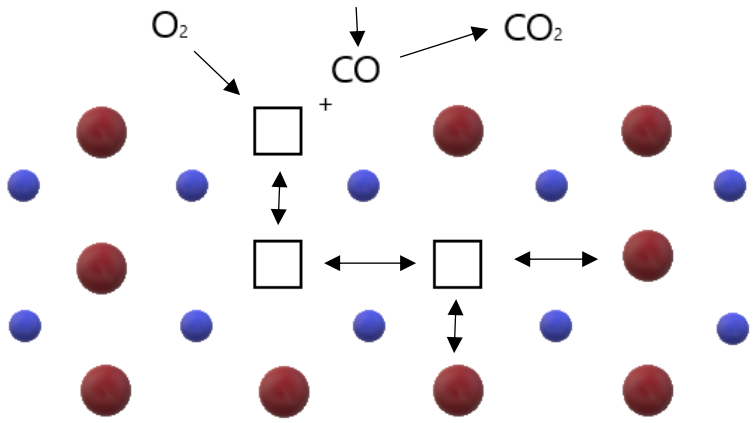

Fig 3. An example of the movement of oxygen atoms through the cerium oxide nanoparticle. Vacancies allow oxygen to move to the surface to interact with CO to produce CO_2; alternatively, oxygen provided by O_2 can be moved into the structure for storage.

Conesa[30] reported that oxygen vacancies improved the oxygen release and uptake in cerium oxide nanoparticles. They found that the surfaces that were easiest to form vacancies within were {100} and {110} surfaces, the most difficult being the {111} surfaces as these are the most stable. A factor in the production of vacancies is the surface charge present, with vacancies being easier to form in polar surfaces where they have the beneficial effect of reducing surface charge.

A study by Liu et al.[35] investigated the effect of oxygen vacancies on the catalytic properties of nanorods. They produced two types of nanorods, one with oxygen vacancies across {111} and {100} surfaces, the

other with reduced oxygen vacancies across {100} and {110} surfaces. They reported that the nanorod with large oxygen vacancies was more catalytically active despite possessing a less reactive (111) surface.

2.4 Crystallization

Crystallization is the process by which disorganised atoms/ions are organised into an ordered structure known as a crystal. Crystallization is split into two stages: nucleation and crystal growth.

Nucleation

Nucleation is a term for the process of a new structure starting to form. The rate of nucleation dictates how long that new structure takes to form, this can be affected by a variety of factors such as the presence of defects, temperature, and the concentration of free particles within the system[36]. There are two forms of nucleation, homogeneous and heterogeneous nucleation:

Homogeneous nucleation consists of the production of a new crystal nuclei without external contact, the rate of this nucleation can be calculated using the following equation[37, 38]:

$$R_{HOM} = MjZexp(-F_H/kT) \qquad \textit{(Equation 5)}$$

In this equation 'F_H' is the free energy change, '*M*' is the number of molecules, '*j*' is the monomer flux, '*kT*' is the thermal energy, and '*Z*' represents the probability that the nucleus goes into a new phase. However, homogeneous nucleation is a lot more difficult to occur, this is due to the nature of newly developed crystals of small size to dissolve.

The formation of homogeneous nuclei can be calculated thermodynamically[39]:

$$total\ free\ energy = sum\ of\ surface\ free\ energy + bulk\ free\ energy$$

For spherical nanoparticles, the following equation can be used:

$$\Delta G = 4\pi r^2 y + \frac{4}{3}\pi r^3 \Delta G_v \qquad \textit{(Equation 6)}$$

In this equation 'ΔG' represents the total free energy, '*y*' is the surface energy density, 'ΔG_v' is the volume energy density, and finally '*r*' is the radius of the nanoparticle.

Alternatively, heterogeneous nucleation is a more common form of nucleation, this occurs on a disorganised surface. The nucleation rate on the disordered surfaces occur at differing rates across various surfaces, this rate can be calculated by the equation[40]:

$$R_{HET} = \sum_{i=1}^{N} j_i Z_i \exp\left(-F_i/kT\right) \qquad \textit{(Equation 7)}$$

In this equation 'j_i' is the monomer flux, 'Z_i' is the Z factor, 'F_i' represents the free energy barrier, and $\sum_{i=1}^{N}$ means these calculations are sum of all the nucleation sites.

Crystal Growth

The second stage of crystallization is termed crystal growth and takes place after nucleation has occurred, it involves the expansion of the crystal nuclei through deposition or rearrangement of atoms. There are various methods and mechanisms describing the different processes for the growth of the crystal.

Beginning with classical growth this method is dependent on the surface reaction and monomer diffusion rate. Nanoparticles that are above a certain size, also known as the critical size, will continue to grow whereas those that are below the critical size may dissolve back into a solution. This process of smaller

crystals dissolving back into the solution is the basis for another method known as Otswald Ripening[41, 42] ,within this mechanism the dissolving of crystals below the critical size allows the constituent atoms to be redistributed onto larger crystals that are above the critical size that have not dissolved, contributing to their growth and therefore increase in size. Another mechanism for crystallization and crystal growth was developed by LaMer et al.[43, 44]. This method involves a sharp increase of monomer concentration within a solution initiating nucleation over a short time period. After this nucleation stage, the growth of the crystal can be controlled via the limitation of the monomer diffusion rate, this method has been used previously to produce nanoparticles[45, 46].

The processes of Coalescence[47] and Orientated Attachment[48] crystallization differ from previous methods of nanoparticle production. As opposed to other methods that separate the growing nanoparticles, coalescence and orientated attachment methods involve the combination of multiple small nanoparticles into a larger single nanoparticle. Focusing on the orientated attachment method, the mechanism begins with the sudden organisation of the atoms into a single crystal plane promoting reduction in the energy of the system. As these crystal planes produce multiple nanoparticles, they begin to interact with the surrounding nanoparticles through van de Waals interaction. The main difference between coalescence and orientated attachment crystallization is that within the former, the nanoparticles combine in any arrangement whereas with the latter, the nanoparticles rearrange across grain boundaries to a lower energy configuration. This method of orientated attachment has been implemented and observed in previous studies such as with the production of titanium dioxide nanorods[49].

The discussed mechanisms above all relate to the production through crystallization of nanoparticles from monomer solutions. However, within this study the recrystallization stage was different as it involved the rearrangement of atoms that were already constructed into an amorphous structure.

Grain Boundaries

Grain boundaries occur at the interface between two crystal planes with differing crystal structure, this creates misorientation between the planes leading to changes within the nanoparticle properties. The grain boundaries are measured by their level of misorientation and possess a tendency to produce defects such as dislocations. There are two main levels of misorientation, firstly low angle which is a term used when the misorientation is less than 15 degrees of rotation. Secondly, high-angle is the term used when the misorientation is greater than 15 degrees of rotation, these high-angle grain boundaries possess a higher level of disorder then low-angle due to a larger grain boundary gap for defect ions.

The various forms of misorientation have been previously studied[50], two examples of these are tilt and twist misorientation. Tilt misorientation involves the rotation of the crystal plane parallel to the boundary plane, whereas twist misorientation involves rotation of the crystal plane perpendicular to the boundary plane. The energy of a low-angle boundary is dependent on the degree of misorientation between the crystal planes, this energy can be calculated using the Read-Shockley equation[51].

The grain boundaries present within a nanoparticle can impact on the properties of that nanoparticle, these properties such as the electrical, magnetic and vibration. This impact can primarily be caused by the defects created by the grain boundaries and the ions that they produce.

A study by Aljawfi et al.[52] investigated the effect of grain boundary defects on the electrical and magnetic properties of chromium doped, zinc oxide nanoparticles. They observed that the structure of the nanoparticle was more ordered at the crystal plane than at the boundary. They further discovered that the defects created by these grain boundaries increase the oxygen vacancies present leading to an increase in the ferromagnetism. However, the defect ions at the grain boundaries additionally produced a form of electrical barrier that increased the resistance across the boundary reducing the electrical properties.

2.5 Vibration

The vibrations of nanoparticles hold the potential as a technique for identification; this has led to interest in terms of research. The relationship between the frequency of the nanoparticle vibration and its morphology could allow the prediction of geometric and behavioural properties from that nanoparticle vibration. Properties such as the size, shape and composition of the nanoparticle will affect its vibration frequency suggesting the potential to identify these properties from the vibration.

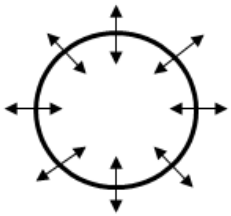

Fig 4. Example of the radial breathing mode of spherical nanoparticles.

The types of vibration that occurs for a nanoparticle can depend on the nanoparticle's shape. Spherical nanoparticles have a radial breathing mode where the atoms within the nanoparticle expand and contract in a symmetrical manner in all directions. An investigation by Hartland[53] into the vibration of spherical gold nanoparticles found that as the diameter of the nanoparticle increased, the frequency of the vibration decreased.

Alternatively, nanorods have at least two vibration modes. They possess a radial breathing mode caused by the symmetrical vibration of the nanorod in all directions. Due to the introduction of length there becomes the possibility of extensional vibration which is the expansion and contraction of the nanorod in a lengthways direction. Large et al.[54] investigated the vibrations in metallic nanoobjects, they identified these various vibration modes in nanorods. They reported on three main vibration modes; the breathing mode, the extension modes and finally a quadrupolar mode caused by expansion of the nanorod in the radial direction along the length of the structure like a wave.

a)

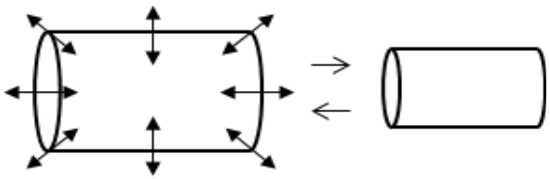

Fig 5a. Example of the radial breathing mode of a nanorod.

b)

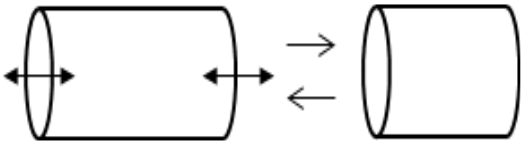

Fig 5b. Example of the extension vibration of a nanorod.

The propagation of vibration through a nanoparticle occurs through the interaction of vibrating atoms interacting with stationary atoms sharing energy across the interatomic bonds causing the stationary atom to begin to vibrate and the bond to lengthen. This mechanism repeats itself causing a wave to spread throughout the nanoparticle until it reaches the surface, where the interatomic bonding pulls the surface atom back causing the bond to shorten and the structure to begin to contract. In the simulation that were conducted the energy within the system does not change, therefore as the number of vibrating atoms increases the individual vibrational displacement in each atom interaction reduces to conserve the energy within the system. This reduction in atom displacement leads to a reduction in the vibration which is observed through a decrease in the pressure fluctuations. This is confirmed by molecular dynamics simulations run by Kogure et al.[55] where they caused vibrations within nanoparticles and found that the number of "hot"/vibrating atoms increased over time spreading throughout the nanoparticle. They also found that the mean velocity of the vibrating atoms decreased over time as well as the number of vibrating atoms increasing.

The relationship between the physical properties of carbon nanoparticles and their radial breathing mode frequencies have been investigated by several papers to develop equations for the calculation of radial breathing mode frequencies. In the works of Jishi et al.[56] the phonon modes of carbon nanotubes are investigated to develop an equation for the calculation of the radial breathing mode using the diameter of the nanotube, this equation is shown below:

$$\omega_{RBM} = \frac{A}{d} \qquad \textit{(Equation 8)}$$

In this equation *A* is a constant commonly reported with a value between 218 – 248 cm^{-1} and d is the diameter of the nanotube. An equation for the calculation of the diameter can be provided by Rafii – Taber et al.[57] as follows:

$$d = \frac{0.246}{\pi}\sqrt{n^2 + mn + m^2} \qquad \textit{(Equation 9)}$$

In this equation '*m*' and '*n*' are integers that represent the chirality and helicity of a single walled carbon nanotube. Although these equations are designed for the calculations of carbon nanotubes it suggests that the radial breathing mode frequency for nanoparticles can be calculated from the physical properties of the nanoparticle.

There are several methods for the inducing and studying of vibrations within nanoparticles.

One of the most common methods is ultrafast spectroscopy; this method uses short laser pulses to obtain data on the frequency of nanoparticle lattice vibrations. It works through the excitation of electrons in the structure causing the lattice temperature to rise; this diffuses through the lattice causing a reduction to a normal breathing state. Excited electrons in the nanoparticle interact with phonons to produce electron-phonon coupling during the vibration. The produced vibrations are impacted by the geometry of the nanoparticle.

Voisin et al.[58] implicated ultrafast spectroscopy to measure the electron interactions of silver, gold and copper nanoparticles. They examined samples of nanoparticles ranging in sizes from 2 – 15nm using femtosecond pump probe technique. The technique allows the gathering of information on the electron-electron scattering, electron-lattice coupling. The oscillations observed through this technique have been found to be similar to the frequencies of the breathing mode of these nanoparticles.

Another method of analysing the lattice vibrations is through Raman spectroscopy, this method works by exciting photons in the nanoparticle causing inelastic and elastic scattering. The elastic scattering photons have the same energy as the incident photon whereas the inelastic scattering photons have a different energy to the incident photon. The vibrations of the structure can be measured through the inelastic scattered photons. The energy difference between the incident photon and the inelastic scattered photon is the energy required to excite the structure to vibrate.

Various methods of Raman spectroscopy can be employed to analyse the vibrations of nanoparticles. Wheaton et al.[59] investigated the use of Extraordinary Acoustic Raman (EAR) spectroscopy to measure single nanoparticles. This method involved the use of two lasers at different wavelengths to incite vibrations within the nanoparticle. They measured the vibrations of nanoparticles between 20 nm and 40 nm and found the peak frequency decreased with nanoparticle size and confirmed the ability to measure the vibration of single nanoparticles using Raman spectroscopy.

2.6 Molecular Dynamics Simulations

Molecular dynamics is a technique used for the computational simulation of compounds and structures. It is based on Newton's laws of motion in relation to the movement and predicted movement of atoms within a simulated system. The use of Newtonian mechanics although simple, can allow the theoretical prediction of nanoparticle properties and behaviour, as well as their catalytic properties and the molecular interactions. The use of molecular dynamics in computational simulation does not circumvent the need for experimental data or research but provides theoretical properties and interactions under desired conditions using coded constraints and force field application.

Molecular dynamics simulation begins with an initial input of atom positions and velocities, additional conditions such as pressure and temperature are then applied. With the atom and environment conditions of the simulation set to the desired values, the new atom positions and velocities are then calculated at each time step and the data produced recorded at designated intervals through the simulation. This recorded data is then analysed for the values of the specified properties of interest to the study being conducted. An important factor in these calculations is the potentials that are used during the molecular dynamic simulations as it provides information on how the interaction between atoms will be calculated during simulation. There are several different potentials that can be used for calculating atom interaction, one example of these is the Buckingham Potential:

$$U_{(r_{ij})} = A \exp\left(-\frac{r_{ij}}{p}\right) - \frac{C}{r^6{}_{ij}} \qquad \textit{(Equation 10)}$$

A and C within the calculations represent constants of attraction and repulsion across the interatomic bond length (*r*) between two example atoms (*i* and *j*). These calculations come together to provide a value for the potential energy ($U_{(rij)}$) between the two atoms. The interatomic potentials used within molecular dynamic simulation to calculate the interactions between atoms are simplified to reduce the amount of computational power required and lowering the cost of computational study.

There are several advantages to using molecular dynamics to simulate experiments via computational means. Firstly, the ease of which results can be obtained through computer simulation. After an initial training period it is relatively easy to use molecular dynamics techniques to simulate a wide range of different systems under a variety of conditions that may be difficult to recreate experimentally. The turnaround time for computational simulation is reduced when comparing to experimental research, data can be obtained within a matter of hours or days that could take months or years to recreate experimentally. The use of coding means that changes to the compounds being simulated are relatively simple to conduct with just a few lines being changed especially when compared to the potentially costly repercussions were this mistake to be replicated within an experimental setting. The use of molecular dynamics also adds portability to the research; advances in remote accessibility means that a researcher can make changes from any location without travelling to the laboratory. This portability and functionality also aid in the aspect of collaborative research with computational files capable of being easily shared amongst other researchers.

The costs of computational research are additionally reduced when compared to the experimental in the long term. An initial production and installation of supercomputer facilities can incur a large cost; however, after this initial cost computer simulation can be used to establish the optimum conditions for a variety of compound production experiments removing the cost of materials for trial and error in experimental stages. The removal of physical chemicals also reduces the health risks to researchers and the additional costs of accidents, incorrectly written code is relatively cheap and easily rectified when caught in initial stages compared to costs incurred by incorrectly mixed chemicals or spillages as well as the health dangers posed to researchers in these situations. There are still health risks posed by computational research however these are more long-term issues such as eye strain alongside further health issues incurred by a sedimentary working style at a desk, however, these can be managed.

There are still disadvantages to computational simulation using molecular dynamics. The initial cost of supercomputer facilities can become considerable dependent on the processing power desired. This initial investment may take a long time to balance out with money saved from experimental research without including the running cost in the form of regular maintenance, energy provisions and regularly updating the software licences. Additionally, the cost of training researchers in the use of computer simulation

techniques and the time it would take is a further disadvantage for the use of molecular dynamics, this training would also require regular updating as new versions of the coding software is released.

Although quicker than experimental methods, the time taken by computational simulation varies upon the complexity of the system being simulated as well as the number of timesteps required for the reaction being simulated. Due to molecular dynamics relying on the calculation of interactions between each atom in the system being simulated being conducted at each timestep period, systems with a high atom count or with multiple compounds present can take longer than simpler systems with less atom interactions to calculate.

Another fundamental flaw in using molecular dynamics simulation is the accuracy and reliability of the theoretical data produced against experimental data. Reason for this is the limited accuracy of over-simplified potentials that sometimes require further fitting to experimental data. Another reason is that defects found within experimentally produced structures can provide differing results than the theoretical values produced from perfect crystals using computational methods. However, updates developed through research has allowed the inclusion of defects such as dislocations and impurities to increase the reliability of theoretical data. This further highlights the need to maintain up to date software and training when using molecular dynamics in research.

3. Theoretical Methods

3.1 Molecular Dynamics

Molecular Dynamics is a method that involves the use of traditional mechanics such as Newton's laws of motion to computationally simulate the interactions of molecules and atoms. Through the use of control parameters such as temperature and pressure, the interactions within a system can be studied under designed conditions. After definition of initial atom position and velocities, potentials and Newton's laws can be applied to calculate the resultant positions and velocities at each step.

Newton's Laws of Motion

As previously stated, within Molecular Dynamics techniques, Newton's laws of motion can be used for the calculation of velocities and positions during simulation. The most relevant of Newton's laws of motion for this study is Newton's second law. This law can be rearranged to incorporate the values of known properties to calculate the new atom positions and velocities within the system during each step of simulation. Beginning with the original equation arrangement:

$$F = ma \qquad \textit{(Equation 11)}$$

Within this equation '*F*' is the force acting upon the atom, '*m*' is the mass of the atom, and '*a*' is the acceleration of the atom in the x, y and z directions. However, within this study, the acceleration of the atom is not initially known, the acceleration is expandable as the change in velocity over time.

$$a = \frac{dv}{dt} \qquad \textit{(Equation 12)}$$

This equation can be rearranged to incorporate known variables:

$$F = m\frac{dv}{dt} \qquad \textit{(Equation 13)}$$
$$F = m\frac{d^2r}{dt^2}$$

Within this equation 'r' is the atom coordinates and 't' is the time. This can then be interpreted to relate to the term of the potential energy of the system, this potential energy term is provided by the designated potentials that are reported in section 3.2:

$$F_{ij} = -\frac{\partial}{\partial r_{ij}} U_{(r_{ij})} \qquad \textit{(Equation 14)}$$

'F_{ij}' is the force of the example atom pair '*i*' and '*j*' and 'U_{ij}' is the potential energy of interactions between example atom '*i*' and '*j*'.

Thermodynamic Ensembles

Ensembles are a collection of possible states in which a system may exist. This produces a distribution of probabilities for the state of the system and its properties. A thermodynamic ensemble focuses on the thermodynamic properties in the production of this distribution of probabilities dependent on which properties are being studied. The two types of thermodynamic ensembles that were implemented within this study are known as NVT and NVE ensembles based upon the thermodynamic properties that are kept constant within the simulation.

NVT ensembles are characterised by set values for the number of moles (N), the volume (V), and the temperature (T). A simple method to control the temperature is through the rescaling of the velocities which can be done using equations of motion such as those produced by Nosé[60] or the Langevin method[61]. These equations incorporate terms for friction and random force. In this study the NVT ensemble was used in the nanoparticle preparation stages to maintain the temperature of the system at the desired constant during simulation.

Alternatively, NVE ensembles are characterised by set values for number of moles, volume, and the total energy of the system (E). In these simulations the system is assumed to be isolated so that it is unaffected by energy or particles from the environment. At each timestep, the position and velocity of each particle can be calculated to provide the trajectories. These trajectories allow the calculation of all future positions and velocities with the total energy of each state assigned probability based upon where its total energy value falls within the desired range. This ensemble was implemented during the vibration stage as it allows the calculation of the most probable future atom positions and velocities at each timestep.

3.2 Potentials

Forcefields are a crucial element within molecular dynamics calculations as they govern the atomic interactions within the simulation. They have many functions within the simulation such as controlling the reduction of potential energy between atoms and their neighbours through attraction and repulsion or the interactions of atom pairs during bonding. The potentials can be adapted to establish the potential energy of an entire simulated system rather than just individual atom to atom interaction.

There are various potentials that can be used in molecular dynamics simulations. In this study the two potentials that were applied were the Buckingham potential[62] for the melt, recrystallization, and cooled simulations. Additionally, an adapted variation of the Morse potential was applied for the equilibration and the final vibration simulations.

Buckingham Potential

The Buckingham potential involves taking terms for the attraction and repulsion to calculate the potential energy of the entire atom interaction:

$$U_{(r_{ij})} = A\ exp\left(-\frac{r_{ij}}{\rho}\right) - \frac{C}{r_{ij}^6} \qquad \textit{(Equation 15)}$$

In this equation '*U*' is the potential energy between two example atoms '*i*' and '*j*' and r_{ij} relates to the interatomic distance between those two atoms. *A* and *ρ* are the parameters that relate to the repulsion element of the atomic interaction within this equation, whereas *C* is the parameter that relates to the attraction element of the atomic interaction within this equation.

The potential parameter values for the Buckingham potential used in this study were obtained from Sayle et al.[62, 63] and Lewis et al.[64] The Buckingham potential has been used for the amorphization and recrystallization stages of these studies similar to the manner in which they were implemented in this study. Although other potentials were available, these potentials parameters had been used in previous studies and fitted to bulk structural and elastic properties of ceria and were first to show reactive effects for {111} and {110} surface planes.

Atom i	Atom j	A (eV)	P (Å)	C (eV.Å)
Ce	O	1986.83	0.351	20.40
O	O	22764.30	0.149	27.89

Table 1. Table showing the values for the Buckingham potential parameters obtained from Sayle et al.[62]. Sayle[63] provided the values for the cerium – oxygen interaction whereas the value for the oxygen – oxygen interaction was obtained from Lewis and Catlow[64].

Morse Potential

The Morse potential involves the inclusion of atom distance, equilibrium bond distance and dissociation energy to calculate the potential energy of atom interactions. This potential is suited for investigation of vibration properties of molecules due to its inclusion of the effects of bond breaking making it a better approximation for vibration structure and hence its use in the vibrational stage of this study.

$$U_{(r_{ij})} = E_0 \left[\left\{ 1 - exp(-k(r_{ij} - r_0) \right\}^2 - 1 \right] \quad \textit{(Equation 16)}$$

In this equation 'U' is the potential energy between two example atoms 'i' and 'j', E_0 is the well depth otherwise known as the dissociation energy, r_{ij} is the distance between the two example atoms, and r_0 is the equilibrium bond distance.

A version of the Morse potential was used within this study, this potential was produced by Pedone et al.[65] The potential includes a short-range Morse function and an added repulsion term C_{ij}/r^{12}.

$$U_{(r_{ij})} = D_{ij} \left[\left\{ 1 - e^{-a_{ij}(r_{ij} - r_0)} \right\}^2 - 1 \right] + \frac{C_{ij}}{r^{12}} \quad \textit{(Equation 17)}$$

In this equation '*U*' is the lattice energy, '*z*' is the ion charge on the example atoms and similar to the original Morse potential r_{ij} and r_0 represent the distance between two example atoms and the equilibrium bond distance respectively. For this study, the potential parameter values for the Morse function were obtained from Sayle et al.[66]

Atom i	Atom j	D_{ij} (eV)	a_{ij} (Å^{-2})	R_0 (Å)	C_{ij} (eV Å^{-2})
Ce	O	0.098	2.930	1.848	1.0
O	O	0.041	3.189	1.886	22.0

Table 2. Table showing the values for the modified Morse potential parameters obtained from Sayle et al.[66], they provided parameter values for both the cerium – oxygen and oxygen – oxygen interactions.

Coulomb's Law

The Coulombic potential relates to the electrostatic portion of the atomic interaction between two particles that are charged:

$$F = k_e \frac{q_1 q_2}{r^2} \quad \textit{(Equation 18)}$$

This can be modified to relate to the potential energy between two example ions 'i' and 'j':

$$U_{(r_{ij})} = \frac{q_i q_j}{4\pi\varepsilon_0 r_{ij}} \quad \textit{(Equation 19)}$$

Within this equation '$U_{r_{ij}}$' relates to the interaction between example ions 'i' and 'j', 'q_i' and 'q_j' are the charges on those ions, 'ε_0' represents the permittivity constant and 'r_{ij}' is the distance between the ions. The charge properties of the particles used within this study are reported below, they are split into the charges for the Buckingham potential and modified Morse potential:

Buckingham Potential		
Atom	**Mass (amu)**	**Charge (e)**
Ce	140.12	+4.0
O	15.99	-2.0
Morse Potential		
Atom	**Mass (amu)**	**Charge (e)**
Ce	140.12	+2.4
O	15.99	-1.2

Table 3. Table showing the values for atom mass and atom charge included in the Coulombic potential, these values are separated by their related potential Buckingham and Morse. When empirical interatomic potentials are developed, the potential parameters are optimised for a particular selection of charges. “Formal” charges such as those selected for the Buckingham potential and “partial” charges such as those selected for the Morse potential are two common choices.

Total Energy Calculation

The calculation of the total interaction energy of an atom pairing can be obtained through the combination of the Coulomb function with the designated potential of the simulation. In this study the calculation of the total interaction energy for the atom pairings within these simulations required the combination of a Coulomb function, the equation is written as:

$$U_{(r_{ij})} = \frac{q_i q_j}{4\pi\varepsilon_0 r_{ij}} + Aexp\left(-\frac{r_{ij}}{\rho}\right) - \left(\frac{C}{r_{ij}}\right) \qquad \textit{(Equation 20)}$$

This equation allows for the calculation of the total energy of the interaction of one atom pairing, this can be simply modified to calculate the total energy of the entire system:

$$U_{(r_{ij})} = \sum_{ij} \frac{q_i q_j}{4\pi\varepsilon_0 r_{ij}} + \sum_{ij} Aexp\left(-\frac{r_{ij}}{\rho}\right) - \left(\frac{C}{r_{ij}}\right) \qquad \textit{(Equation 21)}$$

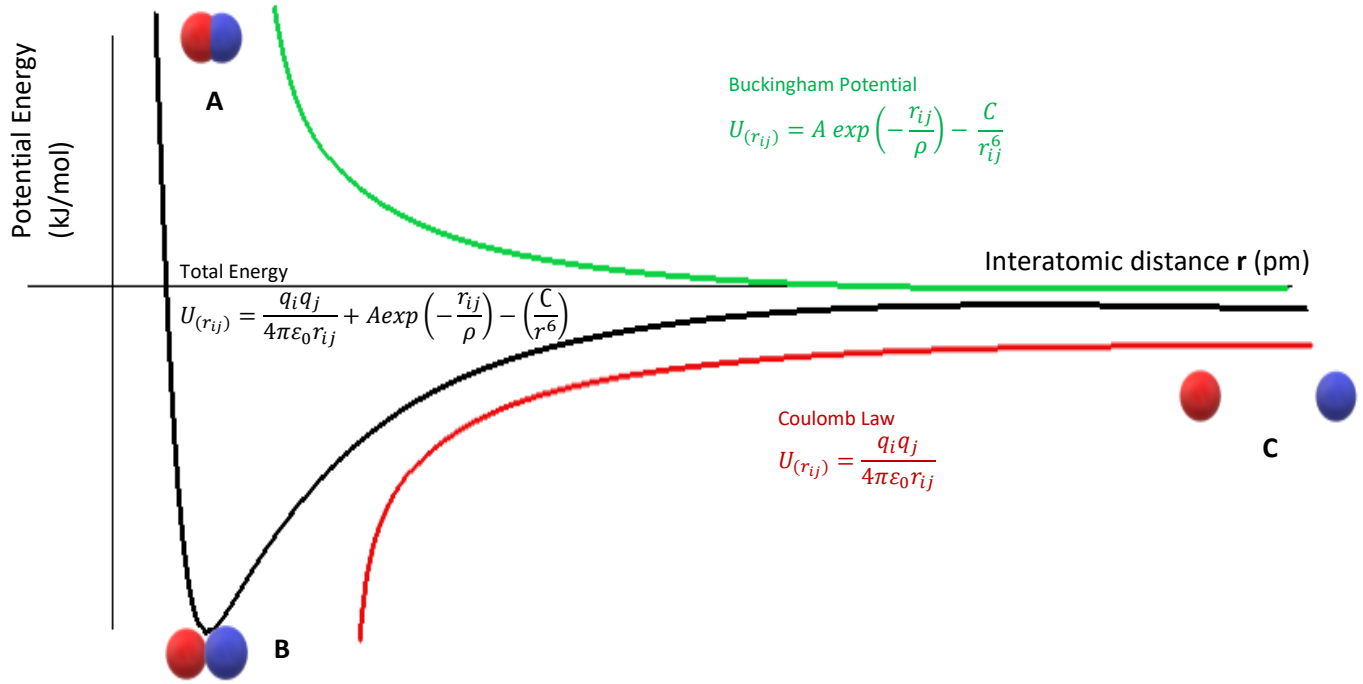

A – Too close **B** – Equilibrium distance **C** – Too far

Fig 6. This figure shows the variation in potential energy against the increase and decrease of the interatomic distance. The Buckingham potential is represented by the green line whereas the Coulomb's function is represented by the red line, and the incorporation of the two into the total interaction is represented by the black line. The figure displays the potential energy development and interatomic distance at the point where bond formation occurs. Between the points labelled A and B the attractive forces are in effect becoming dominant at point A where the atoms are too close for bond formation, whereas between point B and C the repulsion forces are in effect becoming dominant at point C where the atoms are too far apart for bond formation. As the figure shows both potentials show the potential energy approaching zero as the interatomic distance increases, reaching zero when **r** reaches infinity.

When calculating the total interaction energy of a system, it is easier to define the particle charges using Coulomb's Law. It is more difficult to accurately define the constraints and parameters for the potentials, such as those used with the Buckingham potential. As these values are based on various methods such as spectroscopic analysis, they can vary from study to study.

3.3 DL POLY

DL POLY[67] is a molecular dynamics package that provides a base code for modification for a variety of different simulated interactions and environments. In this study the DL POLY code was used for the simulation of the amorphization, crystallisation, relaxation, and equilibration stages during the preparation of the nanoparticle models. The same code with minor alterations was in used in the vibration simulations after an initial velocity change was implemented within the code.

Periodic Boundary Conditions

For this study, a set of periodic boundary conditions were implemented for simulating the interactions of the nanoparticle models. The use of periodic boundary conditions is common practice for computational calculations as it allows the modelling of smaller unit cells to interact in the same manner as the larger bulk materials providing information of the properties of the full bulk structure from the smaller unit reducing the amount of data for simulation reducing the amount of computation power required. When using periodic boundary conditions, the interactions of the simulations are examined within a central unit cell known as the supercell which is then surrounded by infinitely repeated periodic unit cells that are identical to the initial supercell.

During the calculation stages of the simulation it is the atoms located within the supercell that are included in the calculation. The atoms located within the immediate surrounding periodic unit cells may be considered in the form of their interactions with the supercell atoms, granted the repeated cell is located within the 'Cut Off' distance included within the DL POLY code. The atoms within the repeated cells located beyond the cut off distance are not considered in the calculations of the supercell atoms. This is the case for nanoparticles which are effectively zero dimensional objects. In contrast, in extended objects such as a nanowire or nanosheet, atoms have the potential to move to the boundary wall of the supercell 'box', when these atoms pass through the boundary wall an atom enters from the opposite side of the supercell originating from the neighbouring periodic cell replicating the atom movements of the central cell.

3.4 Simulations

All the nanoparticles used within this study went through three stages of preparation prior to vibration. Amorphization, recrystallization and cooling; this was to transform an initial produced structure to a structure with more realistic surface planes and crystallography. A spherical nanoparticle, with a selected radius, was built from parent cerium oxide material. Ce^{4+} or O^{2-} atoms were removed from the surface to neutralise the charge across the nanoparticle. The nanoparticle was then amorphized at 4500 K for 50,000

steps, crystallized at 1500 K for 5 million timesteps and finally cooled at 100 K for 10,000 timesteps, each timestep was equivalent to 0.005 picoseconds. This process was repeated for all the nanoparticles used within this study, with nanocubes being built to selected length, width, and height values and nanocylinders being built to selected length and diameter values.

Simulations within this study were run using 16 processors with the runtime varying between an hour to 48 hours. The time that a simulation took to run was dependent on three main factors: the size and atom count of the nanoparticle, the number of steps in the simulation and finally the processing power available for calculation. Beginning with nanoparticle size, each simulation involved calculating the interactions of each atom against every other atom in the system. Structures with a larger atom count took a larger run time as there were more atoms involved in these atom interaction calculations. Secondly, each stage required a different amount of simulation time for the atoms to achieve a stable arrangement, therefore each stage required a different amount of timesteps to complete. For example, the amorphization of the nanoparticles was quicker requiring only around 50 thousand timesteps whereas recrystallization required more run time at around 5 million timesteps. This increased number of steps meant that recrystallization stages took longer to simulate. A supercomputer was used for all the calculations involved in simulating the various stages of nanoparticle preparation and vibration. The processing power controlled how much data could be processed at one time, therefore the greater the processing power, the more data that could be processed and therefore the quicker the simulation could be performed.

Nanoparticle Preparation

All nanoparticles used in this study were created using the nanoparticle builder tool in Material Studio 2016[68] from a base cerium oxide model. This tool allowed the shape of the nanoparticle to be selected. Once the shape was selected, the desired dimensions for the nanoparticle were inserted into the building tool. There was the capacity to select the desired surface planes for polyhedral and nanocylinder structures, however this was not implemented as the structures were then subjected to a melt and recrystallization stage to produce more realistic surface planes. The units used in this study were Angstrom (Å) for the length, width and height for the nanocube models, radius and length for nanocylinder models and radius for the nanosphere models during the initial generation of the nanoparticle models, however these have been converted into Nanometres (nm) to better relate to the findings found within the literature. The time was reported in picoseconds (ps), which led to the unit of measurement of velocity to be reported as Angstrom per picosecond (Å/ps) and finally the pressure studied during vibration was measured in Pascals (Pa). The next step was to neutralise the charge on the nanoparticle, this was done manually through the removal of excess atoms. The table below lists the shape and size specifications of the nanoparticles used in this study and the atom count of cerium in those nanoparticles.

Nanoparticle Shape	Nanoparticle Dimensions	Cerium Atom Count
Nanocube (Length x Width x Height)	3 nm	665
	4 nm	1687
	5 nm	2916
Nanosphere (Diameter)	4 nm	820
	6 nm	2899
	8 nm	6708

Nanocylinder (Diameter x Length)	4 nm x 2 nm	653
	4 nm x 3 nm	954
	4 nm x 4 nm	1290
	4 nm x 5 nm	1604
	4 nm x 6 nm	1905
	4 nm x 7 nm	2257
	6 nm x 2nm	1458
	6 nm x 3 nm	2131
	6 nm x 4 nm	2916
	6 nm x 5 nm	3589
	6 nm x 6 nm	4262
	7 nm x 2 nm	1979
	7 nm x 3 nm	2892
	7 nm x 4 nm	3955
	7 nm x 5 nm	4868
	7 nm x 6 nm	5781
	7 nm x 7 nm	6721
	8 nm x 2 nm	2576
	10 nm x 2 nm	4047

Table 4. A summary table of all nanoparticles observed in this study. Separated into groups based on nanoparticle shape and further ordered by increasing nanoparticle dimensions. Included is the cerium atom count of each nanoparticle.

After production of the nanoparticle and neutralisation of the charge using Material Studio[68], the nanoparticle files were transferred to a supercomputer for the running of computational simulations. The simulation of all steps in the process of preparing the nanoparticle for vibration was conducted through the use of molecular dynamics. Each nanoparticle simulation was conducted within a self-contained simulation cell. The dimensions of the simulation cells were given values of 120 Angstrom in the x, y, and z directions. This ensured that there was enough space to prevent any of the nanostructures from interacting with the edge of the simulation cell and next periodic cell. All nanoparticles were put through a process of amorphization followed by the recrystallisation of the nanoparticles and finally cooled to set the newly produced recrystallised structure. The NVT ensemble within the DL POLY code that controls the volume and temperature for particles in a system was included to maintain the temperature at a constant for the system. The NVT ensemble was applied unchanged for all nanoparticle preparation stages to ensure the coded value for temperature at each stage remains constant.

Amorphization

Each of the nanoparticles went through an initial simulation of an amorphization stage; they were simulated within conditions of 4500 K for 50,000 timesteps. The temperature conditions within the simulation caused the shifting of atoms from their lattice positions due to the breaking down of the bonds which produced an amorphous structure which could then be recrystallized.

Crystallization

After initial amorphization of each nanoparticle, a recrystallization stage was simulated. The simulated temperature was dropped to 1500 K for recrystallization to begin and each simulation was run for approximately 5 million timesteps. The simulations were observed using VMD[69] to monitor the repositioning of the atoms to produce the final surface planes of each structure.

Alongside the standard recrystallization simulation, an additional simulation was run where the time value for each timestep was adjusted from 0.005 ps to 0.000005 ps. This decreased time value meant that the data for the recrystallization was gathered in smaller increments leading to much better visualisation of atom rearrangement and surface plane production. As this simulation was designed solely for the purpose of examining the rearrangements of the atoms during recrystallization and their formation of the surface planes in greater detail rather than the production of full recrystallized models for vibration, the number of timesteps were reduced leading to a reduction in time to 5 ps.

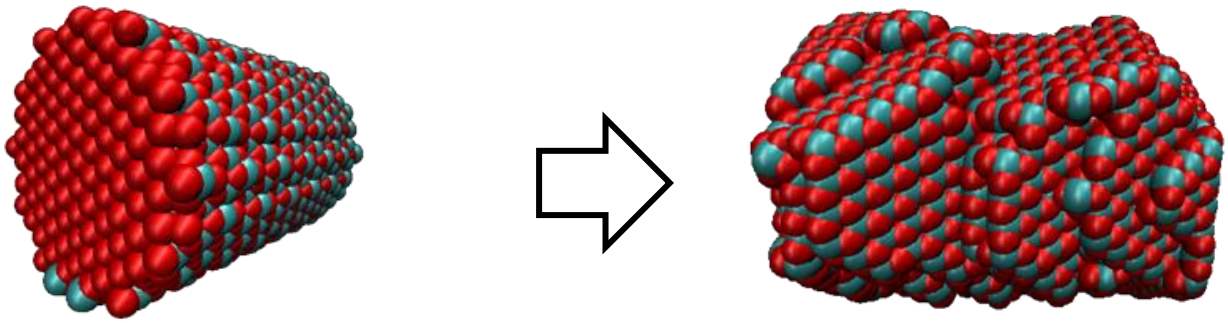

Fig 7. Example of surface plane and crystallography change in nanoparticles after amorphization and recrystallization. The figure shows the change in crystal planes of the 4 nm x 6 nm from the initial build of {100} and {110} cylindrical structure to a hexagonal structure consisting of {100} and {111} planes.

Crystallization begins with the formation of seeds through the clustering of atoms. Nucleation of these seeds causes an expansion of the structure. When two expanding seeds meet, they lead to the production of grain boundaries that can be observed within these nanostructures. Defects observed within the recrystallized nanoparticles were naturally produced as this study is not investigating defect affects there were no designed defects incorporated within the structures. Both the nanocubes and nanospheres within this study produced polyhedral structures after the recrystallization stage with predominantly {111} surface planes exposed with minor exposed {110} surface planes. The (111) plane is the most thermodynamically stable planes therefore this plane is preferentially produced plane during crystallization. The 4 nm x 4 nm nanorod additionally produced a polyhedral structure consisting of predominantly exposed {111} planes with the incorporation of minor {110} surface planes.

The nanorods excluding the 4 nm x 4 nm nanorod produced hexagonal structures after the recrystallization stage. The exposed surface planes observed were a relatively equal distribution of {111} and {100} planes. As previously stated, the (111) plane is the most stable plane thermodynamically whereas the (100) plane is the least thermodynamically stable, however, the latter is the most reactive. The recrystallized structures were then cooled at 100 K for 10,000 timesteps and an additional equilibration stage was incorporated into the nanoparticle production. The equilibration stage was used to incorporate the Morse potential, this was achieved through changing the Buckingham potential for the modified Morse potential and running an additional simulation for 10,000 timesteps at 100 K. Due to the interest in vibrational properties, the final stages of the simulation used the Morse potential. The form of the Morse potential is more realistic for modelling movements of atoms around their equilibrium positions.

Vibration

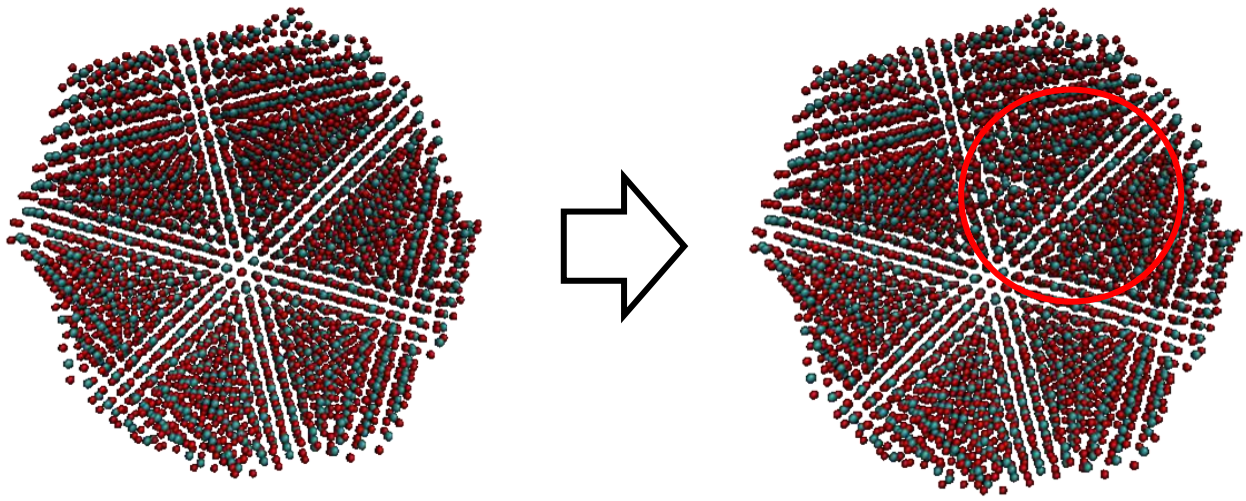

Fig 8. Example of the propagation of vibration through the nanoparticle, displaying the displacement of atoms from their lattice positions due to bond contraction and extension.

After the preparation of the (model) nanoparticles, simulation of the nanoparticle vibrations was performed. To achieve this, energy was introduced into the system by increasing the velocity of a single cerium atom to (typically 250 Å/ps). This induced velocity was kept the same across all vibration simulations to remove the induced velocity as a variable. The introduction of the increased initial velocity caused a collision cascade between atoms that was repeated throughout the nanoparticle causing the spread of energy across the system as vibrational waves. The velocity was increased for one random atom and direction, there was little variation dependent on which atom was modified provided that the atom did not break away from the main structure as this would lead to a secondary shock interaction within the structure distorting the vibration pattern. When the velocity of one atom is altered it shifts from the lattice site which causes it to push the next one out, continuing as a wave from the initial source of energy input until the whole nanoparticle expands which then contracts creating the breathing mode. With two atoms modified this would create two waves which would spread throughout the nanoparticle until they inevitably interacted with each other with two atoms shifting out of their lattice sites towards each other as opposed to outwards creating a distortion in the wave.

In the literature review it is discussed that some structures possess more than a single vibration pattern. Large et al.[54] discussed that nanorods possess both breathing mode and extensional vibration. These patterns are identified to be low frequencies similar to the breathing mode which means that the introduced energy is not required to be considerable and therefore the introduced velocity is not required to be considerable.

Alongside modifying the velocity of a cerium atom, the amount of time represented by each timestep was changed from 0.005 ps to 0.00005 ps. The ensemble was switched from NVT to NVE, using an Ewald precision of 10^{-6}. The vibration within the nanoparticle was measured via the pressure of the system at each recorded timestep; the pressure of the system was recorded as it represents the movement of the atoms with the expansion of the atoms causing an decrease in pressure, which then increases as the atoms contract.

Pressure is measured from the net amount of compression experienced by atoms with respect to interatomic potentials. Each fluctuation of the pressure from high to low was equivalent to one wave of a vibration mode, pressure calculated as a function of time was then recorded to give pressure oscillations with characteristic frequencies. As breathing modes involved the expansion of atoms in all directions simultaneously, these cause the largest fluctuations in the pressure within the supercell. Whereas radial and axial vibration patterns only exhibited expansion across one direction, therefore their effect on the supercell pressure is reduced compared to that of the breathing mode. It was through the implementation of FT analysis that the fluctuations created by the radial and axial vibration patterns become observable as they are overlaid by pressure fluctuations from the breathing modes.

Frequency Calculation

An initial resonant frequency of the breathing mode vibrations was calculated from the time-pressure graphs from the average value of a single wave. However, the nanoparticles within this study are not perfectly spherically symmetric; therefore, several breathing modes co-exist to produce the composite pattern. As such, Fourier Transform (FT) analysis was employed using the Viper[70] code, this allowed for the identification of the various individual frequencies within the initial time-pressure data.

The size of the peak within the FT graph was representative of the quantity of that frequency present within the time-pressure data, the larger the peak; the more prevalent that frequency was. All the frequencies calculated within this study are recorded in Terahertz (THz).

Fourier Transform Analysis

Fourier Transform analysis is a mathematical technique for deconstructing a composite pattern of vibration. It can be implemented to isolate the various component frequencies within these patterns. In this study, FT analysis was conducted to identify the various frequencies present within the pressure-time graphs. Each of these frequencies were representative of the various vibration modes present within the overall vibration pattern.

One of the most common forms of FT analysis is known as (Continuous) Fourier transform, it is implemented in creating one continuous function of the frequency to produce a frequency distribution. In this study, the size of each peak on the FT analysis graphs were equivalent to the percentage presence of that vibration mode.

3.5 Visualisers

Molecular graphical analysis was performed using Material Studio[68] for the initial production of the nanoparticles, and VMD[69] for the visualization of simulations.

4. Results

4.1 Simulation Data

Nanocube 5nm (2916 Ce) - 250Å/ps

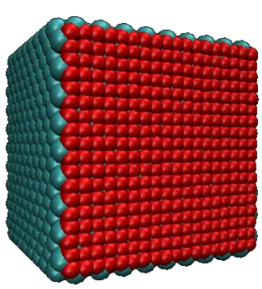

(Initial structure)

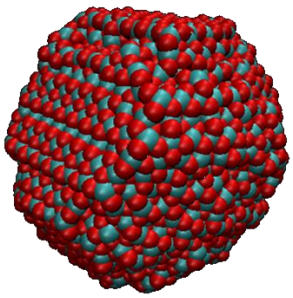

(Final cooled structure)

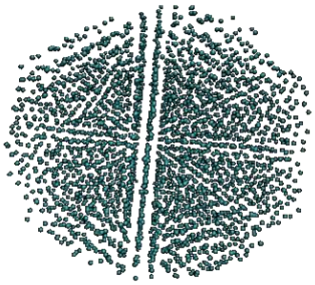

(Final crystalline structure)

Fig 9. Example of the structure development of the 2916 Ce nanocube through the stages of nanoparticle production beginning with the initial structure, post-recrystallization and the final cooled structure. The shape of the nanoparticle develops from cubic to polyhedral with a change in surface planes from {001} to a mixture. These images were obtained through the VMD visualiser, for the initial structure and final cooled structure a 7.0 sphere scale was used, whereas for the final crystalline structure the sphere scale was reduced to 2.0.

The initial structure of the 2916 Ce nanocube displayed {001} surface planes, after amorphization the recrystallization the atoms rearranged into a more stable structure with increased stability of the surface planes such as the (110) plane leading to a change in shape from the cube to a polyhedral structure.

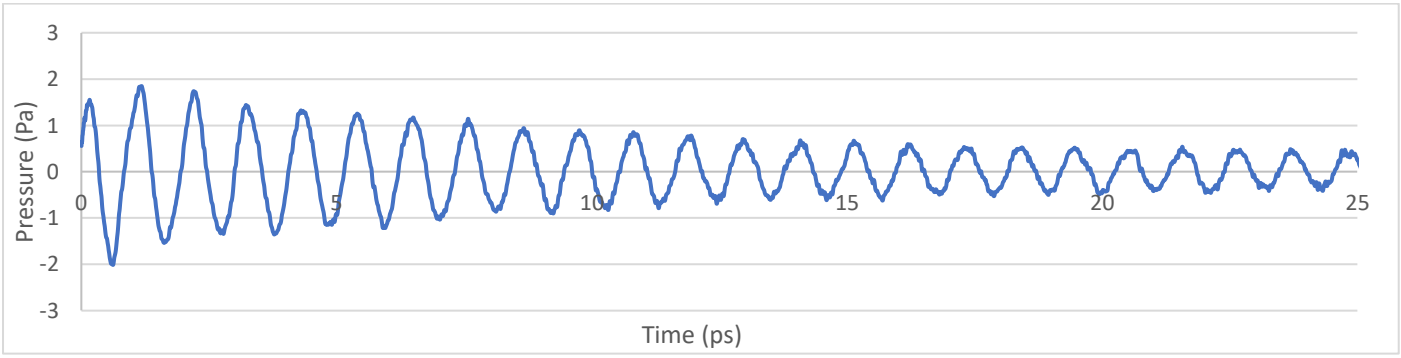

Fig 10. The time-pressure graph for the 2916 Ce nanocube at a vibration initiation velocity of 250 Å/ps. The frequency from this graph was calculated as 0.938 THz.

As previously stated, the velocity was increased for a random atom and direction, and there was little variation dependant on the choice of atom. It is observed in Fig 10 that there is an initial shock created by this amended atom interacting with surrounding atoms. At this point the breathing motion is producing a pressure fluctuation with an amplitude of ±2 pa. This pressure fluctuation is reduced throughout time meaning that the intensity of the breathing motion reduces, however at 17 ps the amplitude of the pressure fluctuation stabilises into a regular pattern of ±0.5 pa suggesting that the breathing motion is occurring at a continuous intensity. Within the graph the areas of high pressure relate to the contraction section of the breathing motion, whereas the areas of low pressure relate to the expansion section of the breathing motion. The expansion of the nanoparticle leads to an increase in the surface area for catalytic activity to occur, therefore the time intervals of low pressure are representative of time intervals where there is potential for high catalytic activity to occur. The amplitude of the reduction in pressure is related to the level of expansion of the structure during the breathing motion, therefore with a higher amplitude of pressure reduction, the level of expansion of the nanoparticle is greater with a larger surface increase allowing for higher catalytic activity.

Fourier Transform Analysis - Nanocube 5nm

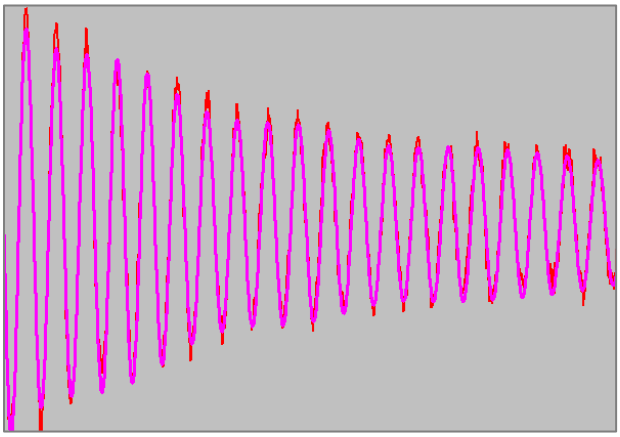

Fig 11. Image taken from Viper displaying the dominant frequency pattern from FT analysis (pink) overlaid upon the time-pressure graph (red).

Frequency (Fourier Transform)	
0.928 THz	Dominant Peak
Frequency (Initial Measurement)	
0.938 THz	

Table 5. Table displaying the frequencies of the vibration through both methods of frequency calculation, initial measurement, and FT analysis.

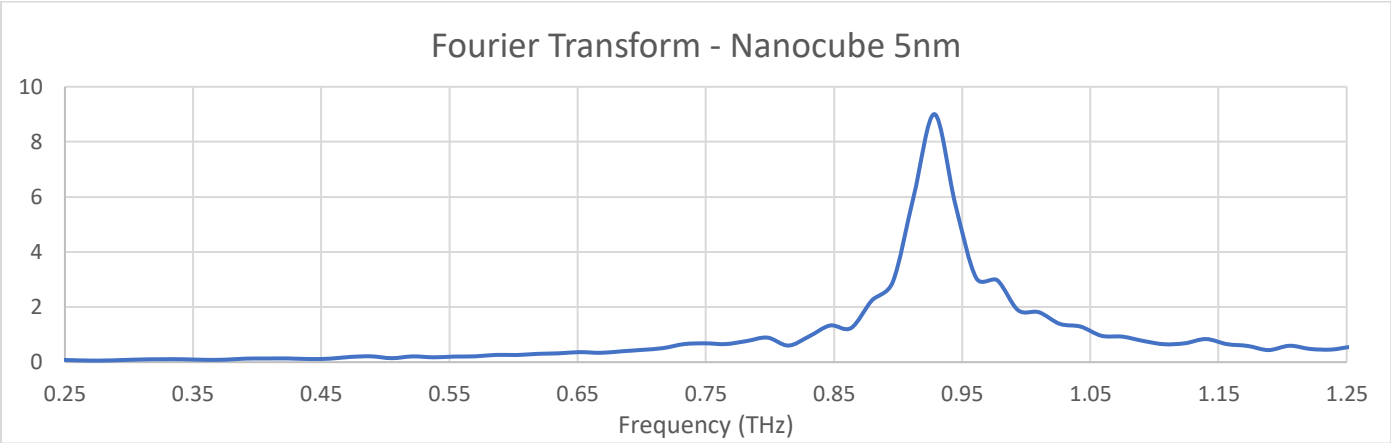

Fig 12. The FT analysis graph for the 2916 Ce nanocube at a vibration initiation velocity of 250Å/ps. A single peak is located at the frequency of 0.928 THz.

It is observed in Fig 12 that FT analysis performed on the 2916 Ce nanocube produced a single peak at the frequency of 0.928 THz. This frequency value was similar to the frequency value calculated during the initial measurement. This is confirmed within Fig 11 where the wave pattern from the peak frequency is overlaid upon the time-pressure graph and display a similar wave pattern. During FT analysis each wave pattern present within the main time-pressure graph produce an individual vibration frequency represented as a peak on the FT analysis graph. Therefore, each peak on an FT analysis graph can potentially be attributed to a vibration motion. The single peak on the FT analysis graph for the 2916 Ce nanocube is representative of the breathing motion.

Nanoparticle Shape	Cerium Atom Count	Initial Measurement Frequency (THz)	FT Analysis Measurement Frequency (THz)
Nanocube	665 1687 2916	1.408 1.039 0.938	1.451 1.060 0.928
Nanosphere	820 2899 6708	1.290 0.932 0.828	1.335 0.928 0.689
Nanocylinder	653	1.538	0.814 (Diameter) 1.578 (Length)
	954	1.262	0.716 (Diameter) 1.255 (Length)
	1290	1.140	1.140 (Diameter + Length)
	1458	1.481	0.586 (Diameter) 1.399 (Length)
	1604	1.129	1.092 (Diameter) 0.502 (Length)
	1905	1.092	1.092 (Diameter) 0.422 (Length)
	1979	1.418	0.536 (Diameter) 1.466 (Length)
	2131	1.114	0.570 (Diameter) 1.091 (Length)
	2257	1.055	1.06 (Diameter) 0.39 (Length)
	2576	1.338	0.470 (Diameter) 1.550 (Length)
	2892	1.064	0.506 (Diameter) 1.091 (Length)
	2916	0.869	0.521 (Diameter) 0.881 (Length)
	3589	0.798	0.796 (Diameter + Length)
	3955	0.787	0.619 (Diameter) 0.993 (Length)
	4047	1.090	0.377 (Diameter) 1.470 (Length)
	4262	0.746	0.744 (Diameter + Length)
	4868	0.735	0.732 (Diameter + Length)
	5781	0.677	0.671 (Diameter + Length)
	6721	0.67	0.667 (Diameter + Length)

Table 6. A summary table of the frequencies calculated in this study from the time-pressure graphs. The 'initial measurement frequency' column relates to the first frequency calculated for each nanoparticle from the average wavelength of the first five waves of the time-pressure graph. The 'FT analysis measurement frequency' column relates to the frequencies produced by FT analysis conducted on the time-pressure graphs and recorded measurements for both diameter and length vibrations. The data has been split into nanoparticle shape groups which are then recorded in order of increasing cerium atom count. The trend for nanocubes and nanospheres shows that as the cerium atom count and therefore overall atom account increases, the vibration frequency decreases. For nanocylinders the trend is similar, however, the radius to length ratio creates heightened frequencies for select nanocylinders.

4.2 Observations

Both the nanospheres and nanocubes after the initial amorphization stage produced a polyhedral structure during the crystallisation stage. This preference to produce a polyhedral structure could potentially be attributed to the more stable nature of the {111} planes of polyhedrals when compared to the less stable {100} planes of nanocubes. This is confirmed through the visualisation of the crystalline structure of the nanospheres and nanocubes as well as through the examination of the time-pressure graphs of these two types of structures and the frequencies of their vibrations that produced a common trendline when plotted.

Many of the time-pressure graphs produced for the vibration of nanoparticles possessed sharp peaks in contrast to the smooth peaks that would be expected. There were common features observed across many of the time-pressure graphs one of these being an initial jump/shock in amplitude caused by the introduction of the increased velocity of the incident atom being transferred through the system. This initial shock in the amplitude then begins to gradually decrease as the number of timesteps that have passed increases. This reduction in pressure fluctuations is potentially caused by the transfer of kinetic energy back into potential energy due to the resistance of the bonded atoms. As the number of timesteps increased the amplitude of the waves decreased to a point where the peaks are less distinguishable potentially due to the presence of more than one vibration pattern created by the incident atom.

These common patterns were not the case for all nanoparticles studied, some structures such as the 4 nm nanosphere and the 4 nm x 2 nm nanocylinder which do not possess a clear gradual decline in the amplitude of the wave in the time-pressure graphs after the initial shock instead these graphs display double peaks alongside fluctuating wave amplitudes. Additionally, some of the larger structures such as the 6 nm x 6 nm nanocylinder and the 7 nm x 5 nm nanocylinder shows little to no initial shock which leads to no pattern of gradual decrease in wave amplitude.

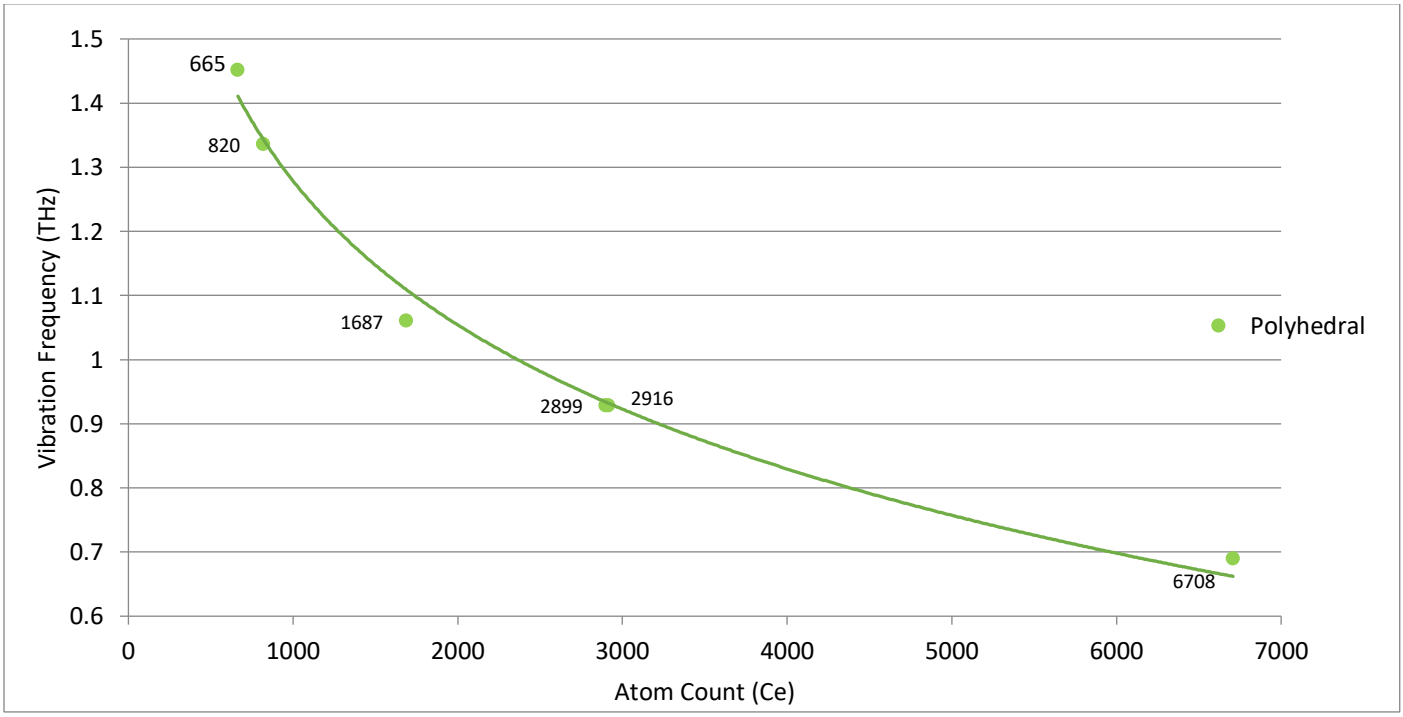

Fig 13. Graph presenting vibration frequency plotted against cerium atom count for both nanocube and nanosphere structures. Due to both nanoparticle shapes producing polyhedral shapes this is presented as a single polyhedral data series. The frequencies used in this graph were obtained from the FT analysis measurements. The points are labelled in size order starting with the smallest at 665 Ce to the largest at 6708 Ce with the frequencies producing a range from 1.451 THz to 0.689 THz. The difference between frequencies are much larger for the smaller atom count models, a change of 0.391 THz between the 665 Ce model and 1687 Ce model, compared to a smaller difference in frequencies for larger atom count models, a change of 0.239 THz between the 2899 Ce model and the 6708 Ce model.

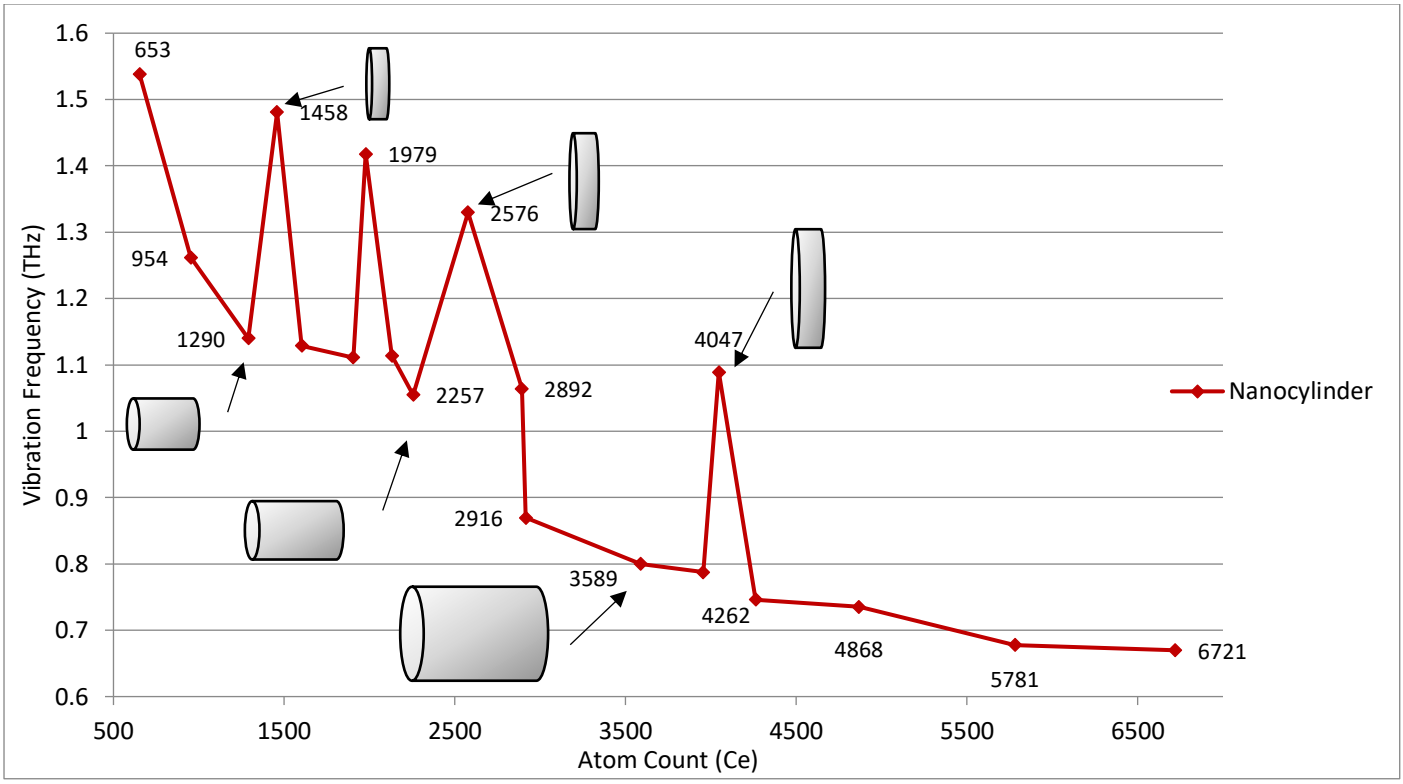

Fig 14. Graph presenting vibration frequency plotted against cerium atom count for nanocylinders. The frequencies used in this graph were obtained from the initial measurements. The points are labelled in size order starting with the smallest at 653 Ce to the largest at 6721 Ce with the frequencies producing a range from 1.538 THz to 0.67 THz. Similar to polyhedrals the overall trend shows that as size increases, the frequency decreases with the rate of frequency decrease being larger for small nanocylinders and smaller for large nanocylinders. Some nanocylinders break the pattern of frequency decrease with increase in size, for example, the 6 nm x 2 nm (1458 Ce) and the 7 nm x 2 nm (1979 Ce) nanocylinders where the frequency is higher than smaller nanocylinders.

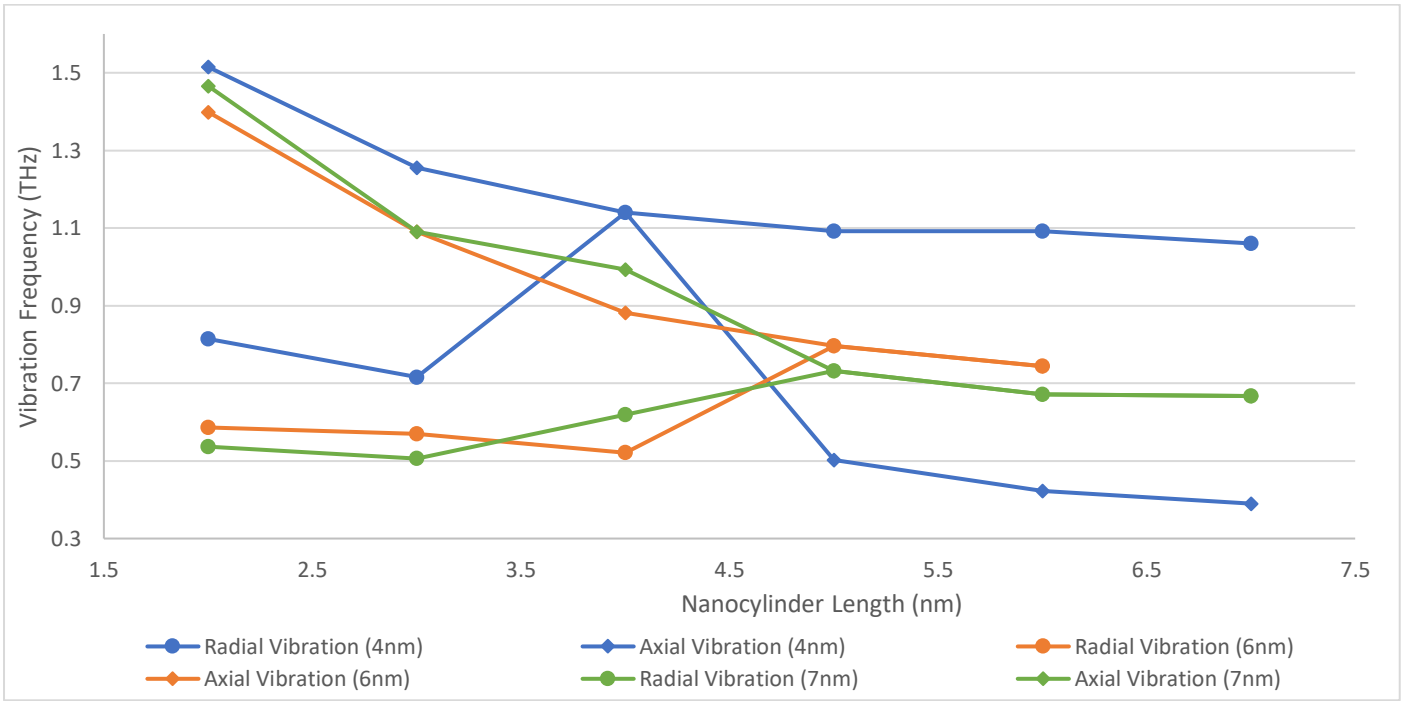

Fig 15. Graph presenting the vibration frequencies of the vibration modes of nanorods against the nanorod length. For the 4 nm diameter nanorods it shows that the vibration frequency of the extensional mode is faster than the vibration frequency of the radial vibration mode whilst the length is shorter than the diameter, the extensional mode then switches to being slower as length surpasses diameter. For the 6 nm and 7 nm diameter nanorods there is a gradual decrease in the vibration frequency of the extensional mode and an increase in the radial vibration mode as length is increased until they share a single vibration frequency for both.

5. Discussion

5.1 Literature Comparison

Size v Frequency

Our simulations predict that the vibrational frequency of cerium oxide nanoparticles increases with decreasing size. This trend is initially observed in the data for the vibrations of the nanocubes and nanospheres which are recorded as a single polyhedral data series in Fig 13. This data series covers nanocubes of 3 nm^3 to 5 nm^3 with a frequency range of 1.451 THz to 0.928 THz and nanospheres with a diameter range of 4 nm to 8 nm that possess a frequency range of 1.335 THz to 0.689 THz.

Wheaton et al.[59] investigated the acoustic vibrations of different sized nanoparticles, studying polystyrene nanoparticles and Titania (TiO_2) using Extraordinary Acoustic Raman (EAR) spectroscopy that combined previous Raman and ultrafast techniques with the results shown below:

Composition	Size	Frequency
Polystyrene	20 nm	0.044 THz
	40 nm	0.022 THz
Titania	20.5 nm	0.158 THz – 0.166 THz

Through the continuation of the trend observed in the data series of the polyhedral models used in this study, a frequency of 0.275 THz would be expected for a model with a 20 nm diameter which is much higher than the frequency value for the polystyrene model, this could potentially be due to the material used. Polystyrene bonds are van der Waals bonds which are much weaker than the ionic bonding that takes place within cerium oxide nanoparticles. The Titania nanoparticle studied by Wheaton possessed a frequency which is much closer to the expected value for a similar sized cerium oxide nanoparticle possibly as they are both metal oxide structures that exhibit ionic bonding. Although there are differences between this study and the study conducted by Wheaton in terms of the size range and the material used, there are similarities in the overall trend that can be established. The authors tested increasing sizes and reported that as the size increased, the frequency of vibration decreased which follows the trend concluded in this study.

This trend of frequency decrease with size increase is further supported by a study conducted by Sauceda et al.[6] who investigated the vibration pattern of different metal nanoparticles of various morphologies. They studied gold, silver, and platinum nanoparticles in three different structure shapes; icosahedron, Mark's decahedral and FCC truncated octahedra recorded below:

Composition	Size	Frequency
Gold	0.5 nm	3.33 THz
	3 nm	1.05 THz
	4 nm	0.74 THz
Silver	0.5 nm	3.33 THz
	3 nm	1.33 THz
	4 nm	1.25 THz

The frequencies of both the gold and platinum nanoparticles are in a similar frequency range to the frequencies in this study and other literature. When comparing the frequencies of 3 nm nanoparticles the frequencies are found to be similar to those observed within this study. They also found that the frequencies decreased as the diameter increased, however, the data shows a more linear trend in the frequency decrease than is observed in this study and Wheaton et al. It is important to note that the

vibrations reported in Sauceda are not the breathing modes and are instead quasi-breathing modes meaning that they are the vibration mode with the smallest deviation from the breathing mode.

Many studies examining the vibration and breathing modes of spherical nanoparticles report similar trends to those concluded in this study[71-73]. However, there are some studies that show deviations from the conclusions of this study.

Goharshadi et al.[74] studied the breathing modes of spherical nanoparticles within cerium oxide powders using a variety of methods such as dynamic light scattering spectrometer, UV-vis and the data analysed using FT-Raman analysis. They studied four samples of nanoparticles taking the average diameter within each:

Nanoparticle diameter	Frequency
5 nm	0.139 THz
8 nm	0.138 THz

Although the overall trend of the data shows a decrease in frequency as the diameter increases, the change in frequencies is much smaller than those observed in this study. A possible cause of this could be due to the frequencies in the study being taken as averages, this allows a larger range in size difference between the smallest nanoparticle and the largest nanoparticle within samples leading to greater variation in co-existing frequencies.

Hodak et al.[75] also found a data pattern that varied from the one this study when investigating the acoustic breathing modes of bimetallic core-shell nanoparticles. They investigated the breathing mode of gold and lead nanoparticles shown below:

Nanoparticle diameter	Frequency
48 nm	0.062 THz
68 nm	0.049 THz

They found overall that the frequency decreased as the radius of the nanoparticle increased however they reported that for larger nanoparticles the change in frequency was larger than for smaller nanoparticles this was a contradiction of this study that found as the size of the nanoparticle increased the change in frequency decreased getting smaller for the larger nanoparticles.

The trend of frequency decrease with an increase in the nanoparticle cerium atom count was also observed within the nanorod data in Fig 14. The data series covers nanorods with an atom count of 653 (4 nm x 2 nm) to 6721 (7 nm x 6 nm) with a frequency of 1.538 THz to 0.67 THz. However, for the nanorod data it was observed that there was a frequency increase for nanorods that possessed a length shorter than the nanorod radius when compared to nanorods with a smaller atom count but a length longer than the radius.

Cardinal et al.[76] investigated the acoustic vibrations of bimetallic Au-Pd core-shell nanorods, they studied gold nanoroads coated in palladium increasing the thickness of the palladium in 1 nm intervals. The initial gold nanorods were 33.7 nm by 9.7 nm with palladium deposited with a thickness range of 0 nm to 5 nm. The palladium was deposited in three methods, around the circumference of the nanorod, on the tips, and finally equally across the entire nanorod surface. They also gathered data on pure gold and pure palladium nanorods of equal sizes, the size range of the nanorods investigated consists of larger nanorods than those investigated within this study. They simulated two different vibration modes, the extension and the breathing modes of the nanorods, the extensional mode had a frequency range of 0.05 THz to 0.02 THz, and the breathing mode had a frequency range of 0.5 THz to 0.125 THz.

The frequency ranges reported by Cardinal et al.[73] are shown below:

Nanorod composition	Size	Frequency
Gold	33.7 nm x 9.7 nm	0.25 THz
Gold - Palladium	33.7 nm x 9.7 nm	0.25 THz
Palladium	33.7 nm x 9.7 nm	0.333 THz

Additionally, the data produced by Cardinal et al[73] showed patterns in the vibrations similar to those found within this study. It showed that for all the simulated nanorods; pure gold, pure palladium and the palladium coated gold nanorod there was an observed pattern that as the size of the nanorod was increased around the circumference and in a uniform manner, the frequency of its simulated breathing mode was found to decrease. This supports the trend observed in this study that found as the size of the nanorod increased, the frequency of the vibration decreased. However, for the nanorods whose size was increased at the tips lengthwise, this pattern was not observed and instead it was reported little change in the overall breathing mode frequency of these nanorods. This is different from the trend observed in the results of this study, which found that there was still a decrease in frequency for the nanorod vibration as the length was increased, though this decrease was reduced for the larger nanorods in this study suggesting that a decrease in vibration frequency with length increase as a feature of smaller nanorods.

The trend of frequency decrease with an increase in nanorod length is further supported by the work of Hu et al[77] who investigated the effect of nanorod length increase on the vibrational response of silver nanorods through ultrafast laser induced heating.

Nanorod size	Frequency
20.7 nm x 46 nm	0.025 THz
22.8 nm x 108 nm	0.0083 THz

They observed that the frequency of the vibrational response decreased as the length of the nanorod was increased similarly to the trend observed in this study, however, they reported a more linear trend in the frequency decrease compared to the curved trend observed in this study.

Peak Split

The use of FT analysis on the vibrations of the nanoparticles in this study allowed for the isolation of the various vibrational modes present within them. In this study two different types of nanoparticles were investigated: symmetrical and asymmetrical.

Symmetrical nanoparticles such as the nanospheres and nanocubes possessed identical distances that the vibration travels across shown in Fig 16a. Fig 16b shows this singular distance means that there is only a single vibration pattern leading to only one frequency being identifiable during FT analysis causing a single peak in the FT analysis graphs. This singular frequency and peak on the FT analysis graphs are also observed for nanorods whose diameter and length were of an identical size and thus identical vibration distance.

a)

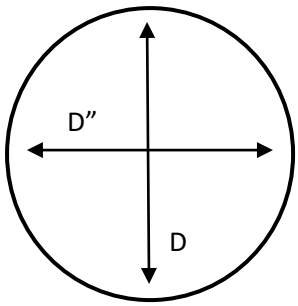

b)

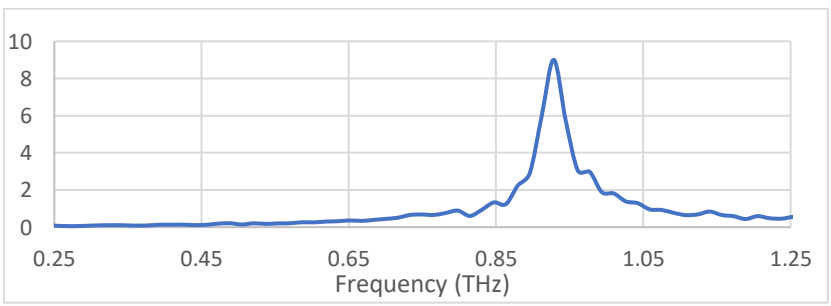

Fig 16. a) Diagram showing an example of the vibration patterns of a symmetrical nanoparticle with value D and D” being equivalent. b) Example of the FT analysis graph of a symmetrical nanoparticle, the single peak produced by the vibration pattern of the equivalent height (D) and the width (D”).

Whereas asymmetrical nanoparticles such as nanorods have different distances for the vibration to travel across for each dimension, diameter, and length, this means that there is more than one vibration pattern present. The presence of these multiple vibration patterns leads to multiple peaks in the FT analysis graphs as each vibration pattern has its own frequency. The frequencies of these peaks and the distance between them has the potential as a method to identify the differences between the dimensions of unknown asymmetrical nanoparticles.

This characteristic of multiple peaks during FT analysis of asymmetrical nanoparticles such as nanorods was supported by Hu et al.[77] during their analysis of the vibrational response of silver nanorods. The FT analysis graphs showed three vibration pattern peaks, two of these peaks were attributed to the extensional vibration mode and the breathing mode. This is similar to the results observed in this study that showed multiple peaks in the FT analysis graphs for the vibration of nanorods. One of these peaks can be attributed to extensional vibration due to a decrease in frequency as length increased and another attributed to the breathing mode vibration.

Additionally, Hu et al.[77] calculated an aspect ratio of length/width for four FT analysis graphs which showed that as the aspect ratio decreased, the difference between the breathing mode and the extensional mode decreased. However, though some of the FT analysis graphs produced in this study showed the same pattern of a decrease in difference in the frequencies between the extensional vibration mode and the

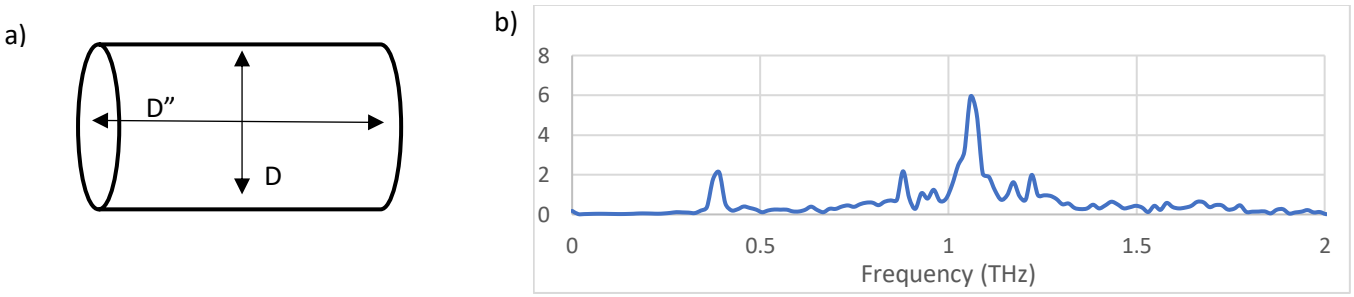

Fig 17. a) Diagram showing an example of the vibration patterns of an asymmetrical nanoparticle with the values of D and D” being of different values leading to multiple vibration patterns, these patterns merge for the breathing mode. b) Example of the FT analysis graph of an asymmetrical nanoparticle, the multiple peaks correlate to different vibration modes produced by the different distances that the vibration must travel across including the breathing mode, the equal expansion of the nanoparticle in all directions.

breathing mode as the aspect ratio decreased, several of the graphs did not conform to this trend. This could potentially be due to the nanorods examined by Hu et al all possessing a length larger than their diameter, whereas in this study the majority of the nanorods possessed a diameter larger than the length. For the nanorods with a 4 nm diameter this aspect ratio also switches from the diameter being larger than the length to the length becoming larger than the diameter.

The presence of these various vibrational modes is further supported by the work of Cardinal et al in their study of bimetallic Au/Pd core-shell nanorods. They investigated the breathing and the extensional vibration modes of nanorods confirming the separate frequencies in asymmetrical nanoparticles. Their data also shows that for nanorods where the length is larger than the diameter of the nanorod, the breathing mode frequency is faster than that of the extensional mode, with the former’s frequency range being 0.5 THz to 0.125 THz and the latter’s being 0.05 THz to 0.02 THz. It supports the results observed in this study for the 4 nm x 5 nm to 4 nm x 7 nm nanorods, the frequency of the breathing mode becomes faster than that of the extensional mode once the length is larger than the diameter as shown in Fig. 15.

Microstructure and Defects

Throughout this study there were several nanoparticles that produced data points that did not perfectly adhere to the trends drawn from this research. One example of this is the FT analysis of the 8 nm x 2 nm and the 10 nm x 2 nm nanorods, the dominant frequencies identified in the FT analysis of these two

nanorods put the frequency much slower than would be expected. The expected vibration frequency for the 8 nm x 2 nm nanorod was 1.338 THz, however the dominant frequency was found to be 0.47 THz, this was the same for the 10 nm x 2 nm which was expected to exhibit a vibration frequency of 1.09 THz however the dominant frequency was found to be 0.377 THz.

Upon examination of the frequency graphs for the 8 nm x 2 nm and 10 nm x 2 nm nanorods there can be identified a point where the frequency wave pattern changes from the pattern produced by the initial shock of the incident atom. Further investigation of the vibration simulations linked a potential cause for the change in vibration patterns can be attributed to a similar defect of asymmetrical faces that can be found on both nanorods. The presence of this defect creates a distortion in the vibration causing the wavelength to increase. This distortion of the vibration waves created by defects within the nanorods led to a change in the vibration frequency due to the increase of the wavelength, as the wavelength increases it leads to a lowering of the vibration frequency.

A study was conducted by Muskens et al.[78] into the longitudinal surface plasmon resonance vibrations across gold nanorods. They studied gold nanorods of an equal size, 30 nm x 15 nm, but with different structure shapes and surface planes. Initially stating with an elliptical shape, the caps were flattened in stages towards a cylindrical shape, they observed that as the caps were flattened the wavelength of the surface vibrations was increased from 616 nm to 645 nm thus leading to a decrease in frequency. This provides further evidence of the impact that the structure and surface planes exhibit on the vibrations of nanorods.

5.2 Why Study Vibration?

Ceria Identification

The size, shape and composition of a nanoparticle can have an impact on the properties of that nanoparticle, hence the importance of being able to measure and identify these factors within experimentally produced unknowns. In this study, the frequency of the vibration modes of cerium oxide nanoparticles are identified to be related to the size and shape of the nanoparticle being analysed.

The observed pattern of frequency decrease as size is increased highlights the potential use of vibration mode analysis as a method of estimating the size of unknown cerium oxide nanoparticles. Standard measurement of the time-pressure graphs, taking an average of the waves produced, primarily works for near-symmetrical nanoparticles such as the polyhedral structures produced by the nanocubes and nanospheres within this study, as these structures produced a singular breathing mode pattern with a single vibration frequency being observed.

It is through the incorporation of FT analysis of the time-pressure graphs that allows for the identification of the symmetry of an unknown nanoparticle alongside its potential for the identification of more complex unknown nanoparticles such as the nanorods. Firstly the number of peaks that were produced within the FT analysis data graphs allowed the confirmation of nanoparticle symmetry, it was observed that symmetrical nanoparticles due to their singular vibration mode and therefore vibration frequency produced a singular peak or tight cluster for the breathing mode, whereas unsymmetrical structures were observed to produce multiple peaks or peak clusters due to the presence of two or more vibration modes and therefore vibration frequencies.

Secondly as these unsymmetrical structures possessed different values for the diameter and length, they produced more than one vibration mode such as a breathing mode but also an extensional vibration mode and therefore more than one vibration frequency was observed. The dominant frequency in these structures was reliant on more than just the size of the nanoparticle but also the diameter to length ratio of the nanorod. Patterns in the FT analysis data showed the beginnings of an identification technique, the

distance between the vibration peaks for the breathing mode and the extensional mode after FT analysis has the potential to be used to estimate the ratio between the diameter and the length of an unknown nanorod. The location of the individual vibration mode peaks on the FT analysis graphs and their relating frequencies could also allow for the estimation of the individual dimensions of the nanorod that is being analysed.

The vibration of the nanoparticles within this study were observed to be similar to quasi-breathing modes in that the expansion of the nanoparticles was wavelike across the whole structure. As individual surface planes caused the nanoparticle to be asymmetric this in turned caused differing sections of the nanoparticle to expand at a varied rate making these vibrations IR active. The variations created by these individual surface planes within these quasi-breathing mode vibrations could potentially be used to not only identify the size and shape of unknown nanoparticles but the surface planes, corners and surface chemistry similar to the 'finger-print' region of an IR spectrum.

IR and the Electromagnetic Spectrum

An area of common use for cerium oxide nanoparticles is in nanomedicine as a source of oxygen during cell repair. The activation of vibration modes to aid catalytic activity would therefore have to take place within the human body. To activate the vibration modes of the nanoparticle, the human body would need to be subjected to a radiation source with enough energy to promote excitation within the nanoparticle.

All the vibration modes observed within this study were located at low frequencies between 0.3 and 1.6 THz, this puts them in the far-IR region of the electromagnetic spectrum. The energy required to excite the nanoparticle and trigger the vibration modes is lower, therefore the frequency and energy of the activating radiation source is lower, reducing the potential harm caused to the human body during activation of the nanoparticle.

Comparing the vibration frequencies of the nanorods it was observed that nanorods of similar sized atom counts possessed differing vibration frequencies dependant on their dimensions. Nanorods with a larger diameter and smaller length had a vibration frequency that was faster than those with a smaller width and larger length. These nanorods with a higher vibration frequency could require more energy to initiate a breathing mode, making them less energetically efficient in some instances.

Catalytic Activity

The shape of a nanoparticle can have an impact on the catalytic activity of that nanoparticle primarily due to the surface planes predominantly produced by that shape. For polyhedral structures the surface planes that are predominantly produced are {111} planes that are more thermodynamically stable but therefore are less reactive when compared to the {001} and {011} planes that are predominantly produced within the nanorod structures which are less thermodynamically stable and therefore more reactive.

As previously stated, Zhou et al[34] investigated the catalytic activity of cerium oxide nanoparticles and nanorods. They observed the predominant surface plane for nanoparticles to be {111} surfaces whereas the predominant surface plane for nanorods to be {001} surfaces. They observed for the conversion of CO that nanorods had a higher rate of activity and suggested a reason for this to be due to the surface planes present.

However, the vibration of the breathing mode causes a shifting of the atoms from the lattice sites producing instability within the nanoparticle and its surface causing an increase in energy. This instability would cause the production of catalytically active sites on the surface of the nanoparticle potentially improving the reactivity of surfaces such as the {111} surfaces observed on octahedral nanoparticles. This increase in reactivity is similar to that observed through temperature increase, energy in the form of heat causes vibration in the atoms shifting them within their lattice sites, making it easier to extract oxygen from the nanoparticle. The vibration created through irradiation has a similar effect of causing atom

shifting within their lattice sites, however it can be performed at low temperatures improving cost effectiveness. As the breathing mode is an expansion of the nanoparticle in all directions, this increase in catalytically active sites would be observed throughout the entire structure rather than a single surface.

The disadvantage of using vibration in this manner is that the expansion of the breathing mode and shifting of the atoms from their lattice positions although is a repeated incident is only momentary. The shift in atoms occurs at the peak of each oscillation for a few picoseconds before returning to their original position of reduced energy and reactivity limiting the use of this method, however with increased frequency this advantageous state of atom displacement would occur more regularly.

Catalytic activity of nanoparticles can be related to the surface to volume ratio of that nanoparticle, a larger surface area provides more opportunity for catalytically active sites across that surface, additionally the smaller volume allows for the easier movement of atoms to and from the surface during oxidation and redox processes. Comparing the nanorods in this study, despite similar atom counts nanorods with a wider diameter and shorter length had a larger surface to volume ratio compared to nanorods with a thinner width but longer length. This shows potential for improved catalytic capacity for nanorods with a wider diameter and shorter length over thinner and longer nanorods for improved efficiency in their uses.

5.3 Calculating Frequency

The two methods of identifying the frequency used in this study presented their own advantages and drawbacks but both allowed the calculation and presentation of the frequency data in a standard form of Hz and THz.

For the initial measurement of frequency, the method of frequency calculation was identical for all the nanoparticles examined within this study, however the data range selection process was different for each one. Beginning at the initial peak observed in the time-pressure graphs, an average wavelength of the first five waves was used to calculate the initial measurement frequency, however, the time of this initial peak was different for each nanoparticle leading to measurement beginning between a range of 0 – 2 ps. The initial measurement method allowed the introduction of human error into the calculation of the frequencies, steps such as measurement of the time when the fifth wave ended was conducted by human eye, however the impact of this process is reduced through the use of average wavelength and a secondary measurement method using FT analysis.

For the FT analysis, the method of frequency calculation and data range selection was kept the same for all the nanoparticle examined in this study. All the time-pressure data contained in the graph was used in the analysis of each individual nanoparticle regardless of initial peak time, this meant that all the waves were analysed and presented in the final data graph regardless of wavelength and the various vibration patterns separated.

When comparing initial measurement of frequency to the various vibration patterns identified using FT analysis, the presence of defects and different surfaces within the nanoparticles and their impact on the wavelength and vibration frequencies of these nanoparticles are crucial, this impact is most clearly observed within the nanocylinders examined in this study. When using Fourier analysis on the vibration graphs of nanoparticles, all the various wavelengths are included into the calculations even those created by defects, surface planes or grain boundaries within the structure, dependent on when this microstructure distorts the vibration pattern may lead to the distorted frequency being the dominant peak. Alternatively, using manual measurement techniques means that any distorted wavelengths can be easily excluded from calculations of the vibration frequencies. This issue can be minimized in computational methods however this is more difficult and involves the limitation of the data range used in the Fourier analysis. Excluding distorted wavelengths that are created by microstructure requires removing the entire section of data rather than just eliminating the distorted vibration pattern.

6. Conclusion

Molecular dynamics was used to investigate the vibrational frequency patterns of cerium oxide nanoparticles of various sizes and shapes. Two methods of frequency measurement were employed in this study, an initial measurement taken from an average wavelength of the first five waves of the time-pressure graphs and a second FT analysis method. All the vibration frequencies calculated for this study were located within the low THz range meaning that they are situated within the far-infrared range of electromagnetic spectrum. The breathing mode vibration of the nanoparticles in this study was observed to cause shifting of the atoms from their lattice sites, similar to the effects of temperature, this could produce an increase in the catalytic activity of the nanoparticle surface improving efficiency in oxidation and reduction processes.

Two major trends are identifiable in the results of this study, the first being that as nanoparticle size increases the vibration frequency decreases. This trend was found across all nanoparticle shapes. However, nanocylinders, possessing lengths smaller than the radius, displayed higher vibrational frequencies than nanocylinders with a lower atom count but possessing lengths larger than the radius. For the polyhedral nanoparticles, the change in frequency was larger for the smaller atom count nanoparticles and smaller for the nanoparticles with a larger atom count. The second trend present is that nanoparticles with symmetric dimensions produced single peak graphs after FT analysis whereas nanoparticles with nonsymmetric dimensions displayed split peaks at different frequencies after FT analysis. This pattern of peak splitting within asymmetrical nanoparticles can be used to characterise the aspect ratios and dimensions of unknown nanoparticles.

Some issues encountered within this study were examining the differences between nanospheres and nanocubes was not entirely possible as they both produced polyhedral structures during the crystallisation stage. However, the trend of these polyhedral nanoparticles showed that as atom count increased, the frequency of vibration decreased. Frequency value for the 8 nm x 2 nm and 10 nm x 2 nm nanocylinders produced through Fourier analysis was considerably different from the frequency value produced from the initial measurement. Finally, the presence of extra data peaks within some of the FT data graphs which can potentially be attributed to the microstructure and defects within the nanoparticle analysed.

7. Further Work

The conducting of experimental research into the vibrations of cerium oxide nanoparticles using a technique such as ultrafast or Raman spectroscopy would aid in supporting the results and trends identified in this study beyond the theoretical simulation. The synthesis of polyhedral and nanorod structures of similar sizes to those investigated in this study could provide confirmation of the surface planes produced and the patterns that are observed.

In this study, the main trend of interest was that when the length of a nanorod was much smaller than the diameter, the speed of the vibration frequency largely spiked. An interesting avenue of further work would be to increase the sample range of the nanorods examined and establish if the trend continues into increasing nanorod sizes, through expansion into larger nanorod sizes and combinations of diameter to length aspect ratios for further confirmation of the trends identified in this study along with the observation of shifts in this pattern. Further investigation into the effects of surface planes on variations within quasi-breathing modes observed within this study would be beneficial in establishing whether they can be applied as a method of identifying surface morphology and chemistry within unknown nanoparticles through infrared excitation and analysis of Fourier Transform data.

Another area of interest for expansion of this research would be to experiment with the doping of nanoparticles with atoms of differing elements. The potential changes created within the vibration of the nanoparticles by the introduction of varied bond lengths could shed light on further methods of tailoring the vibration frequency to desired wavelengths and frequencies that are more efficient. This would have a further effect of altering the oxidation state of the cerium atoms introducing Ce^{3+} oxidation into the structure opposed to the standard Ce^{4+} that is observed within the nanoparticles of this study. This change in oxidation state could also be achieved through the introduction of vacancies into the structure which could potentially impact on the vibration frequency of the nanoparticle by limiting the pathways of energy spread. Considering cerium oxides properties in relation to nanomedicine as an oxidising source for cell repair the potential of measuring changes in vibration frequency caused by the introduction of vacancies, would open possibilities of this vibration analysis method as one to measure activity of the nanoparticle within the body.

8. References

1. Twigg, M.V. (2011) Catalytic control of emissions from cars. *Catalysis Today*. 163 (1), 33 – 41
2. Xu, P-T., Maidment, B.W., Antonic, V., Jackson, I.L., Das, S., Zodda, A., Zhang, X., Seal, S., & Vujaskovic, Z. (2016) Cerium Oxide Nanoparticles: A Potential Medical Countermeasure to Mitigate Radiation – Induced Lung Injury in CBA/J mice. *Radiation Research*. 185 (5), 516 – 526.
3. Tarnuzzer, R.W., Colon, J., Patil, S., & Seal, S. (2005) Vacancy Engineered Ceria Nanostructures for Protection from Radiation – Induced Cellular Damage. *Nano Letters*. 5 (12), 2573 – 2577.
4. Ghavanloo, E., Fazelzadeh, S. A., & Rafii-Tabar, H. (2015) Analysis of radial breathing-mode of nanostructures with various morphologies: a critical review. *International Materials Reviews*. 60 (6), 312 – 329.
5. Stuart, B.H. (2004). *Infrared Spectroscopy: Fundamentals and Applications*. John Wiley & Sons, Ltd.
6. Sauceda, H. E., Mongin, D., Maioli, P., Crut, A., Pellanin, M., Del Fatti, N., Vallée, F., & Garzón, I. L. (2012) Vibrational Properties of Metal Nanoparticles: Atomistic Simulation and Comparison with Time-Resolved Investigation. *J. Phys. Chem. C*. 116 (47). 25147 – 25156
7. Xu, R., Wang, D., Zhang, J., & Li, Y. (2006) Shape-dependent catalytic activity of silver nanoparticles for the oxidation of styrene. *Chemistry, an Asian Journal.* 1 (6) 888 – 893
8. Haruta, M. (1997) Size- and support-dependency in the catalysis of gold. *Catalysis Today*. 36 (1) 153 – 166
9. Valden, M., Lai, X., & Goodman, D. W. (1998) Onset of catalytic activity of gold clusters on Titania with the appearance of non-metallic properties. *Science*. 281 (5383) 1647 – 1650
10. Jarmillo, T. F., Baeck, S. H., Roldan Cuenya, B., & McFarland, E.W. (2003) Catalytic Activity of Supported Au Nanoparticles Deposited from Block Copolymer Micelles. *Journal of the American Chemical Society*. 125 (24) 7148 – 7149
11. Reske, R., Mistry, H., Behafarid, F., Roldan Cuenya, B., & Strasser, P. (2014) Particle Size Effects in the Catalytic Electroreduction of CO_2 on Cu Nanoparticles. *Journal of the American Chemical Society*. 136 (19) 6978 – 6986
12. Narayanan, R., & El-Sayed, M. A. (2004) Shape-Dependent Catalytic Activity of Platinum Nanoparticles in Colloidal Solution. *Nano Letters*. 4 (7) 1343 – 1348
13. Tian, N., Zhou, Z-Y., Sun, S-G., Ding, Y., & Wang, Z. L. (2007) Synthesis of Tetrahedral Platinum Nanocrystals with High-Index Facets and High Electro-Oxidation Activity. *Science*. 316 (5825) 732 – 735
14. Lance Kelly, K., Coronado, E., Zhao, L. L., & Schatz, G. C. (2003) The Optical Properties of Metal Nanoparticles: The Influence of Size, Shape, and Dielectric Environment. *The Journal of Physical Chemistry B*. 107 (3) 668 – 677
15. Choi, H. C., Jung, Y. M., & Kim, S. B. (2005) Size effects in the Raman spectra of TiO_2 nanoparticles. *Vibrational Spectroscopy*. 37 (1) 33 – 38
16. Malani, A. S., Chaudhari, A. D., & Sambhe, R. U. (2016) A Review on Applications of Nanotechnology in Automotive Industry. *Journal of Mechanical and Machatronics Engineering*. 10 (1). 36 – 40
17. Asmatulu, R., Nguyen, P. & Asmatulu, E. (2013) Nanotechnology Safety in the Automotive Industry. *Nanotechnology Safety*. 57 – 72
18. Kašpar, J., Fornasiero, P., & Graziani, M. (1999) Use of CeO_2 – based oxides in the three – way catalysis. *Catalysis Today*. 50 (2). 285 – 298
19. Kašpar, J., Fornasiero, P., & Hickey, N. (2003) Automotive catalytic converters: current status and some perspectives. *Catalysis Today*. 77. 419 – 449
20. Rajeshkumar, S., & Naik, P. (2018) Synthesis and biomedical applications of Cerium oxide nanoparticles – A Review. *Biotechnology Reports*. 17. 1 – 5
21. Wiseman, H., & Halliwell, B. (1996) Damage to DNA by reactive oxygen and nitrogen species: role in inflammatory disease and progression to cancer. *Biochem J.* 313. 17 – 29
22. Liou, GY., & Storz, P. (2010) Reactive oxygen species in cancer. *Free Radic Res.* 44. 479 – 496
23. Trachootham, D., Alexandre, J., & Huang, P. (2009) Targeting cancer cells by ROS-mediated mechanisms: a radical therapeutic approach?. *Nature Reviews Drug Discovery*. 8. 579 – 591
24. Xue, Y., Luan, Q., Yang, D., Yao, X., & Zhou, K. (2011) Direct Evidence for Hydroxyl Radical Scavenging Activity of Cerium Oxide Nanoparticles. *J Phys Chem C*. 115 (11). 4433 – 4438
25. Kim, SJ., & Chung, B. H. (2016) Antioxidant activity of levan coated cerium oxide nanoparticles. *Carbohydrate Polymers*. 150. 400 – 407
26. Dunnick, K. M., Pillai, R., Pisane, K. L., Stefaniak, A. B., & Sabolsky, E. M. (2015) The Effect of Cerium Oxide Nanoparticle Valence State on Reactive Oxygen Species and Toxicity. *Biological Trace Element Research*. 166 (1). 96 – 107
27. Janos, P., Ederer, J., Pilarova, V., Henych, J., Tolasz, J., Milde, D., & Opletal, T. (2016) Chemical mechanical glass polishing with cerium oxide: Effect of selected physico-chemical characteristics on polishing efficiency. *WEAR*. 362 – 363. 114 – 120

28. Na, T., Jingyue, L., & Wenjie, S. (2013) Tuning the shape of ceria nanomaterials for catalytic applications. *Chinese Journal of Catalysis*. 34. 838 – 850
29. Gupta, A., Waghmare, U. V., & Hegde, M. S. (2010) Correlation of Oxygen Storage Capacity and Structural Distortion in Transition-Metal-, Noble-Metal-, and Rare-Earth-Ion-Substituted CeO_2 from First Principle Calculation. *Chem. Mater.* 22. 5184 – 5198
30. Conesa, J. C. (1995) Computer modelling of surfaces and defects on cerium dioxide. *Surface Science*. 339. 337 – 352
31. Wang, X., Jiang, Z., Zheng, B., Xie, Z., & Zheng, L. (2012) Synthesis and shape-dependent catalytic properties of CeO_2 nanocubes and truncated octahedral. *CrystEngComm*. 14. 7579 – 7582
32. Mullins, D. (2015) The surface chemistry of cerium oxide. *Surface Science Reports*. 70. 42 – 85
33. Tasker, P. W. (1979) The stability of ionic crystal surfaces. *J. Phys. C: Solid State Phys.* 12 (22). 4977.
34. Zhou, K., Wang, X., Sun, X., Peng, Q., & Li, Y. (2005) Enhanced catalytic activity of ceria nanorods from well-defined reactive crystal planes. *Journal of Catalysis*. 299 (1). 206 – 212
35. Liu, X., Zhou, K., Wang, L., Wang, B., & Li, Y. (2009) Oxygen Vacancy Clusters Promoting Reducibility and Activity of Ceria Nanorods. *J.Am.Chem.Soc*. 131 (9). 3140 – 3141
36. Sear, R. P. (2014) Quantitative studies of crystal nucleation at constant supersaturation: experimental data and models. *CrystEngComm*. 16. 6506
37. Sear, R. P., (2014) The non-classical nucleation of crystals: Microscopic mechanisms and applications to molecular crystals, ice and calcium carbonate. *International Materials Reviews*. 57. 328 – 356
38. Sear, R. P. (2007) Nucleation: theory and applications to protein solutions and colloidal suspensions. *Journal of Physics: Condensed Matter*. 19. 033101
39. Thanh, N. T. K., Maclean, N., & Mahiddine, S. (2014) Mechanisms of Nucleation and Growth of Nanoparticles in Solution. *Chem. Rev.* 114. 7610 – 7630
40. Chayen, N. E., Saridakis, E., & Sear, R. P. (2006) Experiment and theory for heterogeneous nucleation of protein crystals in a porous medium. *Proc. Natl. Acad. Sci.* 103 (3). 587 – 601
41. Lifshitz, I. M., & Slyozov, V. V. (1961) The kinetics of precipitation from supersaturated solid solutions. *Journal of Physics and Chemistry of Solids*. 19 (1-2). 35 – 50.
42. Yarranton, H. W., & Masliyah, J. H. (1997) Numerical Simulation of Ostwald Ripening in Emulsions. *Journal of Colloid and Interface Science*. 196 (2). 157 – 169.
43. La Mer, V. K., & Dinegar, R. H. (1950) Theory, Production and Mechanism of Formation of Monodispersed Hydrosols. *J. Am. Chem. Soc*. 72 (11). 4847 – 4854.
44. La Mer, V. K. (1952) Nucleation in Phase Transitions. *Ind. Eng. Chem.* 44 (6). 1270 – 1277.
45. Patakfalvi, R., Papp, S., & Dékány, I. (2007) The kinetics of homogeneous nucleation of silver nanoparticles stabilized by polymers. *Journal of Nanoparticle Research*. 9 (3). 353 – 364.
46. Husein, M. M, Rodil, E., & Vera, J. H. (2007) Preparation of AgBr Nanoparticles in Microemulsions Via Reaction of $AgNO_3$ with CTAB Counterion. *Journal of Nanoparticle Research*. 9 (5). 787 – 796.
47. Zheng, H., Smith, R. K., Jun, Y., Kisielowski, C., Dahmen, U., & Alivisatos, A. P. (2009) Observation of Single Colloidal Platinum Nanocrystal Growth Trajectories. *Science*. 324. 1309 – 1312.
48. Niederberger, M., & Cölfen, H. (2006) Orientated attachment and mesocrystals: Non-classical crystallization mechanisms based on nanoparticle assembly. *Phys. Chem. Chem. Phys.* 8. 3271 – 3287.
49. Christy, D., Melikechi, N., Jothi, N., Baby Suganthi, A. R., & Sagayaraj, P. (2010) Synthesis of TiO_2 nanorods by oriented attachment using EDTA modifier: a novel approach towards 1D nanostructure development. *J Nanopart Res*.
50. Ovid'ko, I. A., Pande, C. S., & Masumura, R. A. (2006) 8 Grain Boundaries in Nanomaterials.
51. Moldovan, D., & Wolf, D. (2007) Mesoscale modelling of grain growth and microstructure in polycrystalline materials. *Multiscale Materials Modelling*. 84 – 120.
52. Aljawfi, R. N., Rahman, F., Batoo, K. M. (2014) Effect of grain size and grain boundary defects on electrical and magnetic properties of Cr doped ZnO nanoparticle. *Journal of Molecular Structure*. 1065 – 1066. 199 – 204.
53. Hartland, G. V., Hu, M., Wilson, O., Mulvaney, P., & Sader, J. E. (2002) Coherent excitation of vibrational modes. J. Phys. Chem. B 106. 743–747.
54. Large, N., Saviot, L., Margueritat, J., Gonzalo, J., Afonso, C. N., Arbouet, A., Langot, P., Mlayah, A., & Aizpura, J. (2009) Acousto-plasmonic Hot Spots in Metallic Nano-objects. *Nano Letters*. 9 (11). 3732 – 3738
55. Kogure, Y., Doyama, N., & Nozaki, T. (2007) Molecular dynamics simulation of lattice vibrations and elastic properties in nanoparticles. *J.Phys.:Conf.Ser*. 92. 012055

56. Jishi, R. A., Venkataraman, L., Dresselhaus, M. S., & Dresselhaus, G. (1993) Phonon modes in carbon nanotubules. *Chem. Phys. Let*. 209. 77 – 82
57. Rafii – Taber, H., Ghavanloo, E., & Fazelzadeh, A. S. (2016) Nonlocal continuum-based modelling of mechanical characteristics of nanoscopic structures. *Physics Reports*. 638. 1 – 97
58. Voisin, C., Del Fatti, N., Christofilos, D., & Vallée, F. (2001) Ultrafast Electron Dynamics and Optical Nonlinearities in Metal Nanoparticles. *J. Phys. Chem. B*. 105. 2264 – 2280
59. Wheaton, S., Gelfand, R. M., & Gordon, R. (2015) Probing the Raman-active acoustic vibrations of nanoparticles with extraordinary spectral resolution. *Nature Photonics*. 9. 68 – 72
60. Nosé, S. (1984) A molecular dynamics method for simulations in the canonical ensemble. *Molecular Physics*. 52 (2). 255 – 268
61. Grest, G. S, & Kremer, K. (1986) Molecular dynamics simulation for polymers in the presence of a heat bath. *Physical Review A*. 33 (5). 3628 – 3631
62. Sayle, T. X. T., Parker, S. C., & Catlow, C. R. A. (1994) The role of oxygen vacancies on ceria surfaces in the oxidation of carbon monoxide. *Surface Science*. 316 (3). 329 – 336
63. Sayle, T. X. T. PhD Thesis, University of Bath, 1993
64. Lewis, G. V., & Catlow, C. R. A. (1985) Potential models for ionic oxides. *J. Phys. C: Solid State Phys*. 18. 1149 – 1161
65. Pedone, A., Malavasi, G., Menziani, M. C., Cormack, A. N., & Segre, U. (2006) A New Self-Consistent Empirical Interatomic Potential Model for Oxides, Silicates, and Silica-Based Glasses. *J. Phys. Chem. B*. 110. 11780 – 11795
66. Sayle, T. X. T., Molinari, M., Das, S., Bhatta, U. M., Möbus, M., Parker, S. C., Seal, S., & Sayle, D. C. (2003) Environment-mediated structure, surface redox activity and reactivity of ceria nanoparticles. *Nanoscale*. 5. 6063
67. Smith, W., Forester, T. R., DL_POLY_2.0, (1996) A general-purpose parallel molecular dynamics simulation package, *J. Molec. Graphics*. 14 (3). 136 – 141
68. Dassault Systèmes BIOVIA, Material Studio, Version 7.6, San Diego: Dassault Systèmes, 2016.
69. Humphrey, W., Dalke, A. and Schulten, K. "VMD - Visual Molecular Dynamics". *J. Molec. Graphics*. 14. 33 – 38
70. Klementiev, K. V. VIPER for Windows, freeware
71. Wang, J., Gao, Y., Ng, M-Y., & Chang, Y-C. (2015) Radial vibration of ultra-small nanoparticles with surface effects. *Journal of Physics and Chemistry of Solids*. 85. 287 – 292
72. Voisin, C., Del Fatti, N., Christofilos, D., & Vallée, F. (2001) Ultrafast Electron Dynamics and Optical Nonlinearities in Metal Nanoparticles. *J. Phys. Chem. B*. 105. 2264 – 2280
73. Mankad, V., Mishra, K. K., Gupta, S. K., Ravindan, T. R., & Jha, P. K. (2012) Low frequency Raman scattering from confined acoustic phonons in freestanding silver nanoparticles. *Vibrational Spectroscopy*. 61. 183 – 187
74. Goharshadi, E. K., Samiee, S., & Nancarrow, P. (2011) Fabrication of cerium oxide nanoparticles: Characterization and optical properties. *Journal of Colloid and Interface Science*. 356. 473 – 480
75. Hodak, J. H., Henglein, A., & Hartland, G. V. (2000) Coherent Excitation of Acoustic Breathing Modes in Bimetallic Core-Shell Nanoparticles. *J. Phys. Chem. B.* 104. 5053 – 5055
76. Cardinal, M. F., Mongin, D., Crut, A., Maioli, P., Rodríguez-González, B., Pérez-Juste, J., Liz-Marzán, L. M., Del Fatti, N., & Vallée, F. (2012) Acoustic Vibrations in Bimetallic Au@Pd Core-Shell Nanorods. *J. Phys. Chem. Lett*. 3 (5). 613 – 619
77. Hu, M., Wang, X., Hartland, G. V., Mulvaney, P., Juste, J. P., & Sader, J. E. (2003) Vibrational Response of Nanorods to Ultrafast Laser Induced Heating: Theoretical and Experimental Analysis. *J. Am. Chem. Soc.* 125 (48). 14925 – 14933
78. Muskens, O. L., Bachelier, G., Del Fatti, N., Vallée, F., Brioude, A., Jiang, X., & Pileni, N-P. (2008) Quantative Absorption Spectroscopy of a Single Gold Nanorod. *J. Phys. Chem. C.* 112. 8917 – 8921

9. Appendix

9.1 Visualisers

Material Studio 2016

Material Studio 2016 is a computer modelling and simulation program, it allows the user to create, edit and visualise various molecular structures as well as run analyses to establish a molecule's properties. For this study, the program was used solely to produce the studied nanostructures. It allowed various nanostructures to be produced from a base CeO_2 molecule through imputing specified values into a build nanoparticle tool, the tool then built the nanostructure to bond length calculations for each atom to atom interaction. These nanostructures were then edited manually through the removal of atoms to create charge neutral nanostructures.

Visual Molecular Dynamics (VMD)

Visual Molecular Dynamics (VMD) is a program that allows the 3D visualisation of molecules, nanostructures and other structures, the advantage of this 3D method being the ability to move and rotate the viewpoint to expose otherwise hidden surfaces. VMD contains a variety of tools for editing the visualisation of an examined structure; an example of this is the ability to change atom colouring dependent on different factors such as element, charge or mass. It also has versatility when it comes to atom presentation allowing different styles to be chosen, an example of such is CPK where the atoms are displayed as spheres and further options to change the size of these spheres is available. This range of visualisation options allows the image presented to be tailored to the structure being examined.

For this study VMD was used throughout the runtime of simulations to ensure that they were successful or to identify areas that may have caused issue in cases of crashed simulations. The visualisation preferences selected for simulations prior to the vibration stage were CPK style atom presentations with size 7.0 sphere scale, these preferences were selected as they best displayed the movement of atoms along surfaces during the recrystallisation stage and the final lattice planes present.

Viper

Viper is a program designed for the analysis of XRAFS spectra using various methods, one of these being the use of Fourier-analysis. It allows the splitting and identification of the vibration data into the various frequencies created by vibration modes present, the downside of this program however is that it does not produce the data within a publishable graph itself, it produces a data file however that can be converted within Microsoft Excel. For this study it was used to conduct FT analysis on all nanostructures that were examined to identify the frequencies of the vibration modes present within the vibration graphs.

9.2 Calculating Frequency

The first step was measuring the number of picoseconds it takes for five waves, this was then divided by five to get the average picoseconds for one wave:

$$\frac{Number\ of\ picoseconds\ in\ 5\ waves}{5} = Average\ number\ of\ picoseconds\ in\ 1\ wave$$

The division of one second by the number of picoseconds in one wave provides the frequency in Hertz which is then converted to Terahertz:

$$Frequency\ (Hz) = \frac{1\ second}{Number\ of\ picoseconds\ in\ 1\ wave}$$

$$\frac{Frquency\ (Hz)}{Number\ of\ Hz\ in\ 1THz} = Frequency\ (THz)$$

9.3 Simulation Data

Nanocube 3nm (665 Ce) - 250 Å/ps

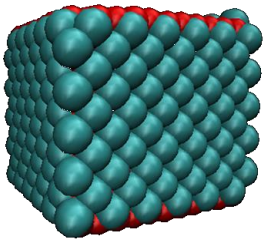

(Initial structure)

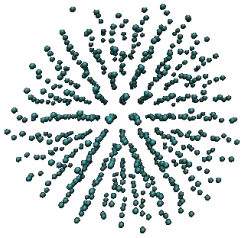

(Crystalline structure)

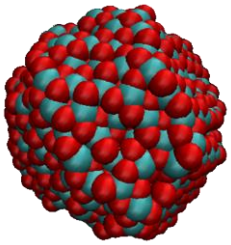

(Final cooled structure)

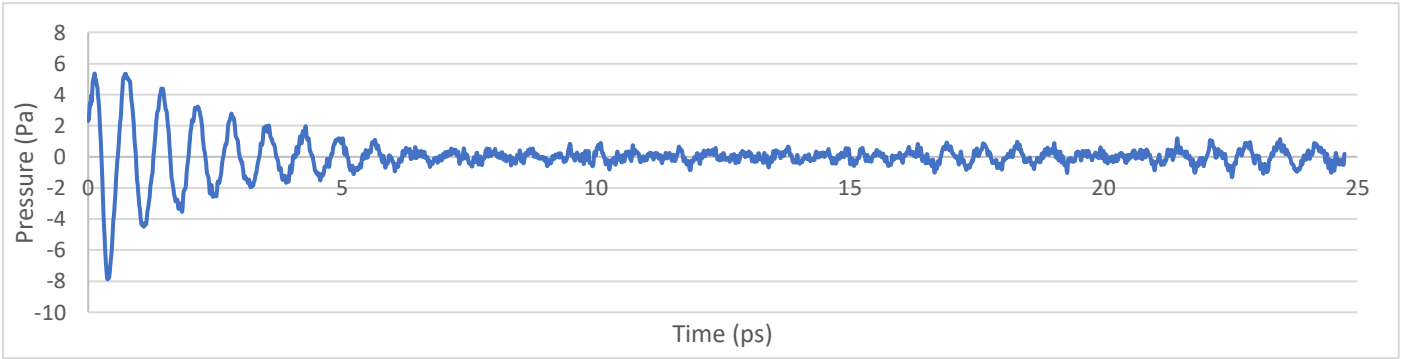

$$\frac{3.55ps}{5\ waves} = 0.71ps$$

$$\frac{1\ second}{0.71x10^{12}} = 1.408^{-12}\ Hz$$

1 second = 10^{-12} ps

$$\frac{1.408^{-12}Hz}{1x10^{-12}} = 1.408\ THz\ (Far\ Infrared\ range)$$

1 THz = $1x10^{-12}$Hz

Fourier Transform Analysis – Nanocube 3nm

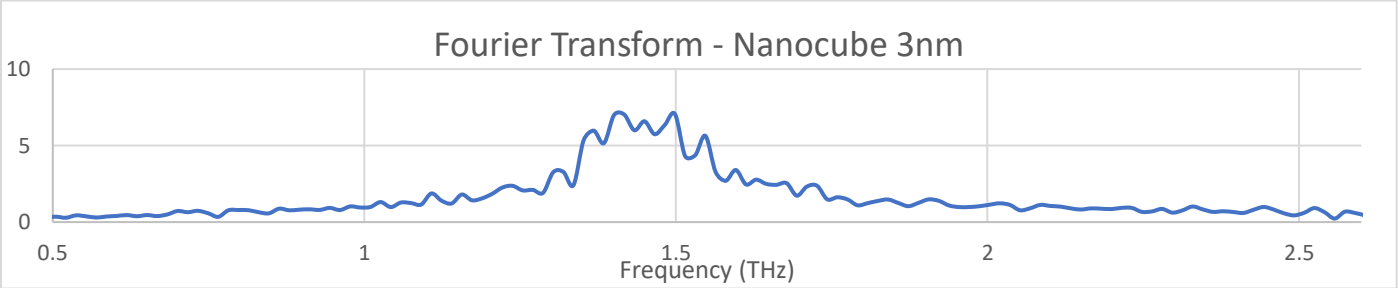

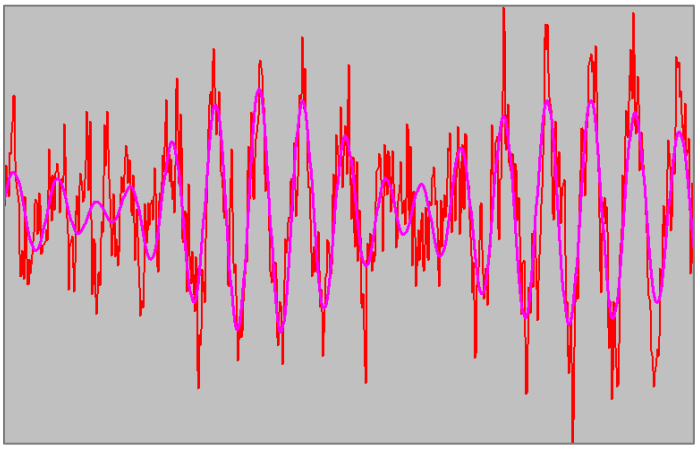

Frequency (Fourier Transform)	
1.451 THz	Dominant Peak (Broad)
Frequency (Manual Measure)	
1.408 THz	

Nanocube 4nm (1687 Ce) - 250 Å/ps

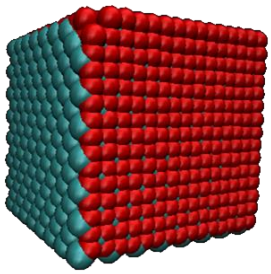

(Initial structure)

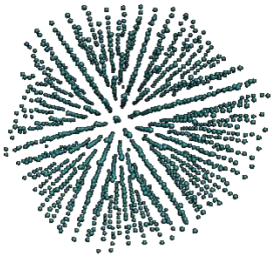

(Crystalline structure)

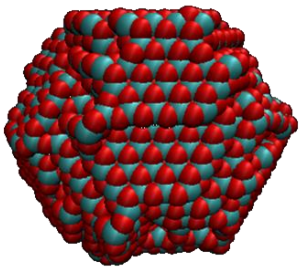

(Final cooled structure)

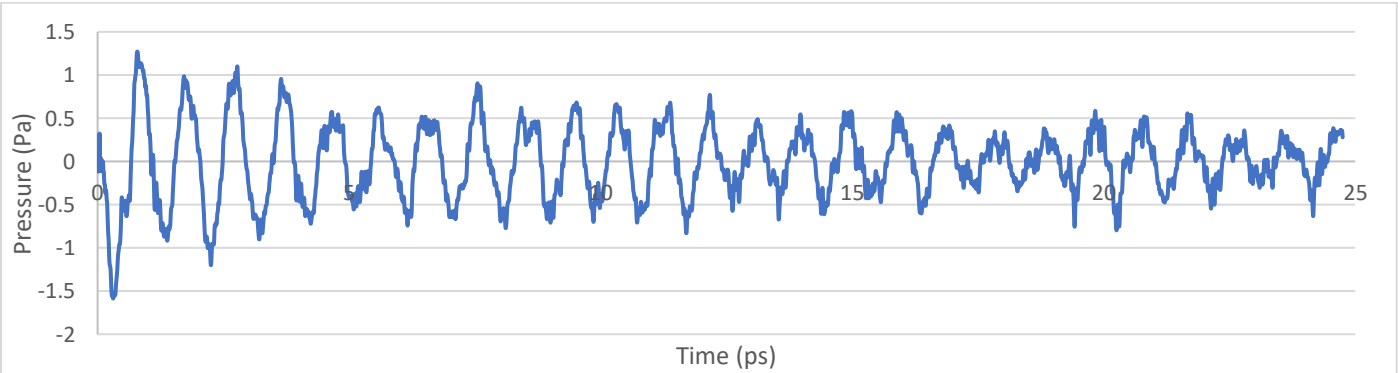

$$\frac{4.812\ ps}{5\ waves} = 0.962\ ps$$

$$\frac{1\ second}{0.962x10^{12}} = 1.039^{-12}Hz$$

1 second = 10^{-12} ps

$$\frac{1.039^{-12}Hz}{1x10^{-12}} = 1.039\ THz\ (Far\ Infrared\ range)$$

1 THz = $1x10^{-12}$Hz

Fourier Transform Analysis - Nanocube 4nm

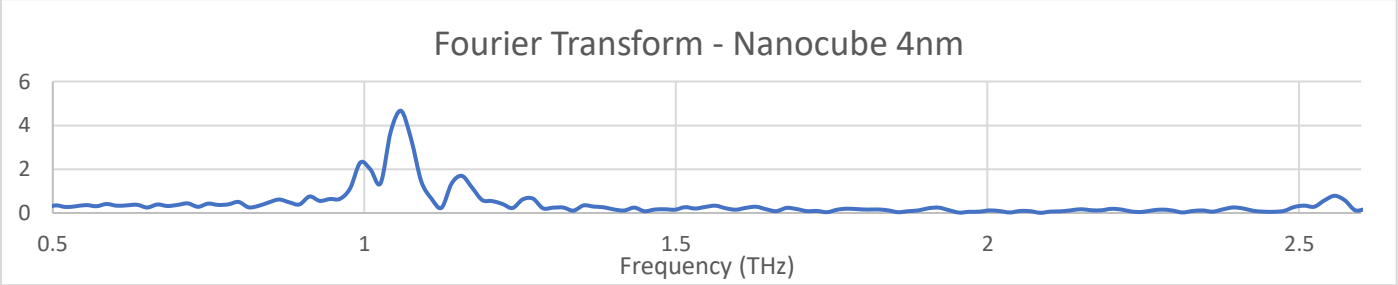

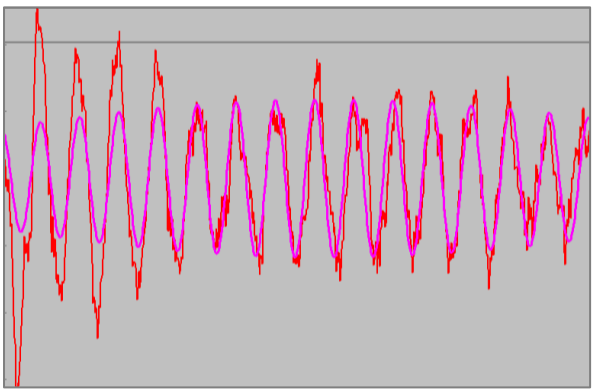

Frequencies (Fourier Transform)	
1.060 THz	Dominant peak
1.156 THz	Minor peak
2.555 THz	Minor peak
Frequency (Manual Measure)	
1.039 THz	

Nanosphere 2nm (820 Ce) - 250 Å/ps

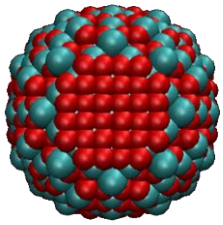

(Initial structure)

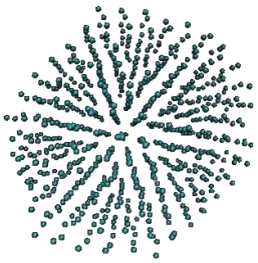

(Crystalline structure)

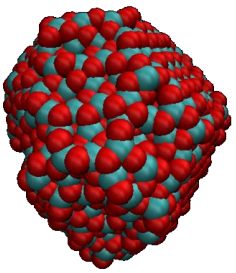

(Final cooled structure)

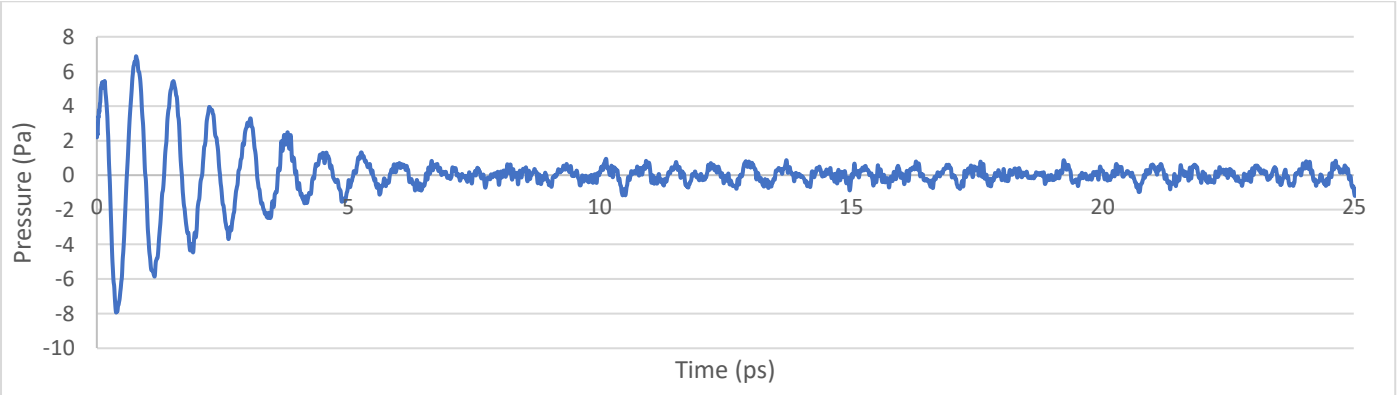

$$\frac{3.875\ ps}{5\ waves} = 0.775\ ps$$

$$\frac{1\ second}{0.775x10^{12}} = 1.290^{-12}Hz$$

1 second = 10^{-12} ps

$$\frac{1.290^{-12}Hz}{1x10^{-12}} = 1.290\ THz\ (Far\ Infrared\ range)$$

1 THz = $1x10^{-12}$Hz

Fourier Transform Analysis – Nanosphere 2nm

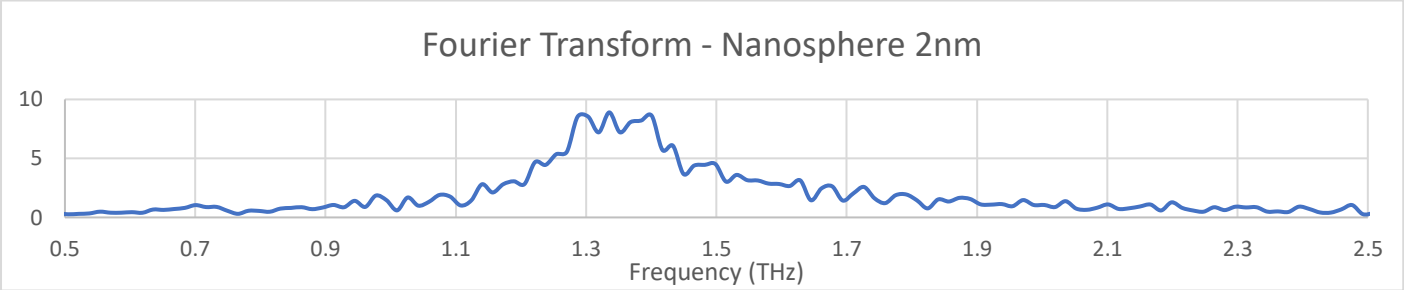

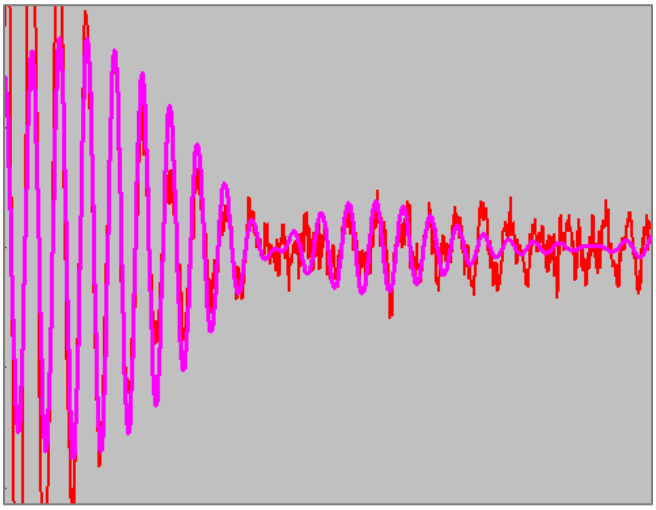

Frequency (Fourier Transform)	
0.701 THz	
1.335 THz	Dominant peak (Broad)
Frequency (Manual Measure)	
1.290 THz	

Nanosphere 3nm (2899 Ce) - 250 Å/ps

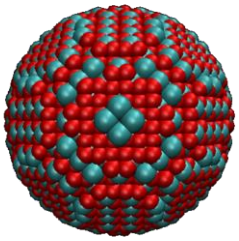

(Initial structure)

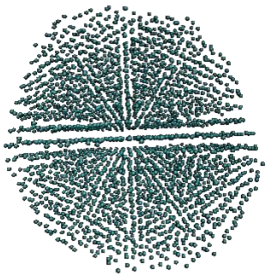

(Crystalline structure)

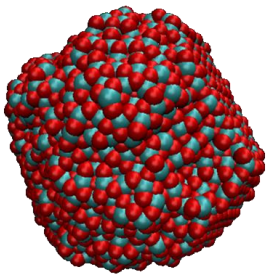

(Final cooled structure)

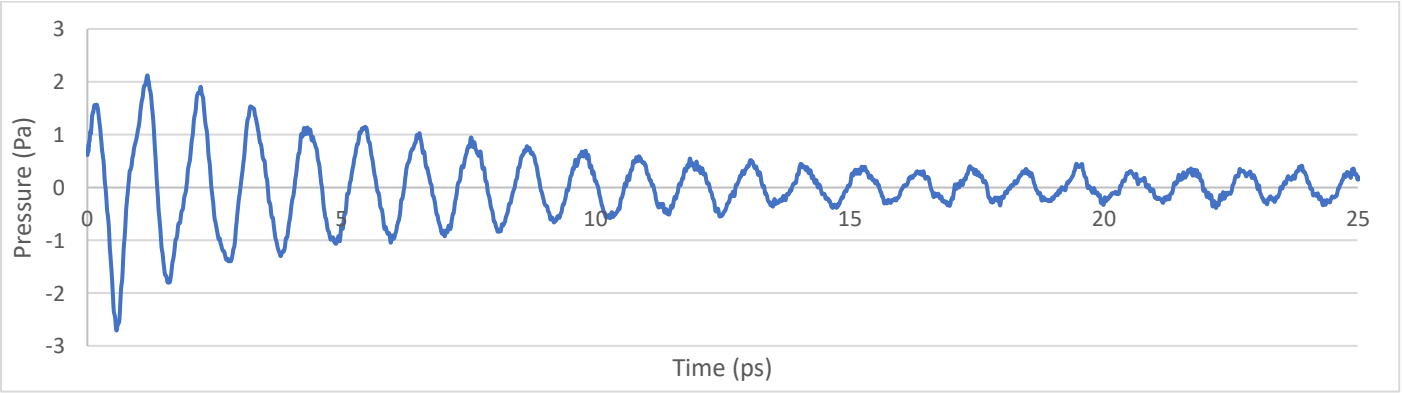

$$\frac{5.362\ ps}{5\ waves} = 1.072\ steps$$

$$\frac{1\ second}{1.072x10^{12}} = 9.328^{-13}Hz$$

1 second = 10^{-12} ps

$$\frac{9.328^{-13}Hz}{1x10^{-12}} = 0.932\ THz\ (Far\ Infrared\ range)$$

1 THz = $1x10^{-12}$Hz

Fourier Transform Analysis – Nanosphere 3nm

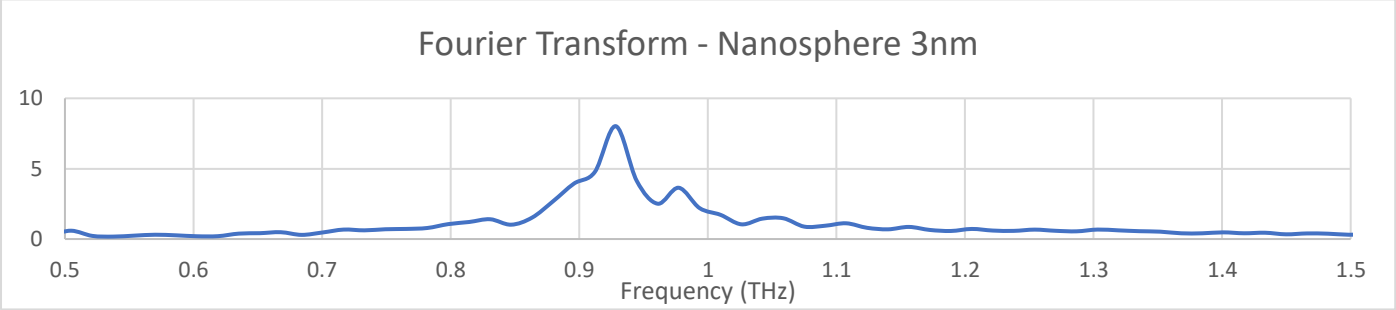

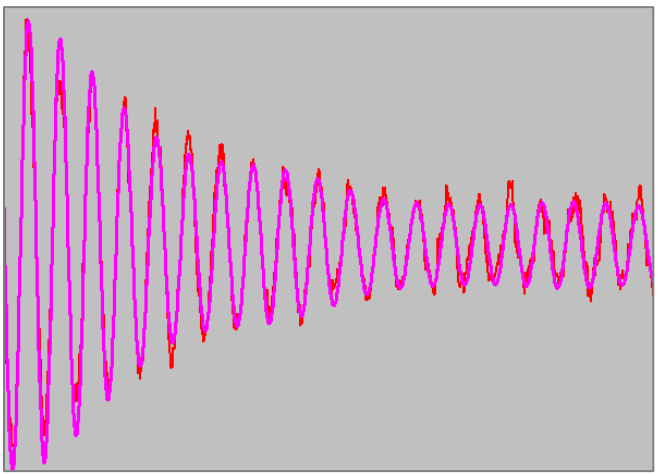

Frequency (Fourier Transform)	
0.928 THz	Dominant peak
Frequency (Manual Measure)	
0.932 THz	

Nanosphere 4nm (6708 Ce) - 250 Å/ps

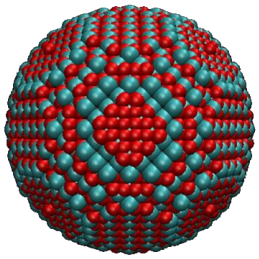

(Initial structure)

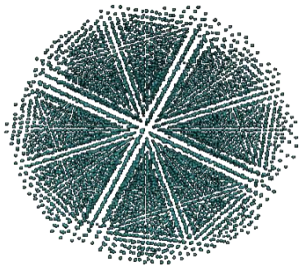

(Crystalline structure)

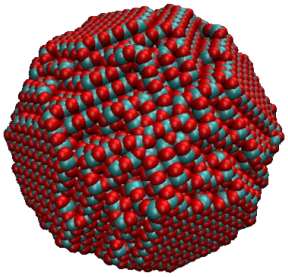

(Final cooled structure

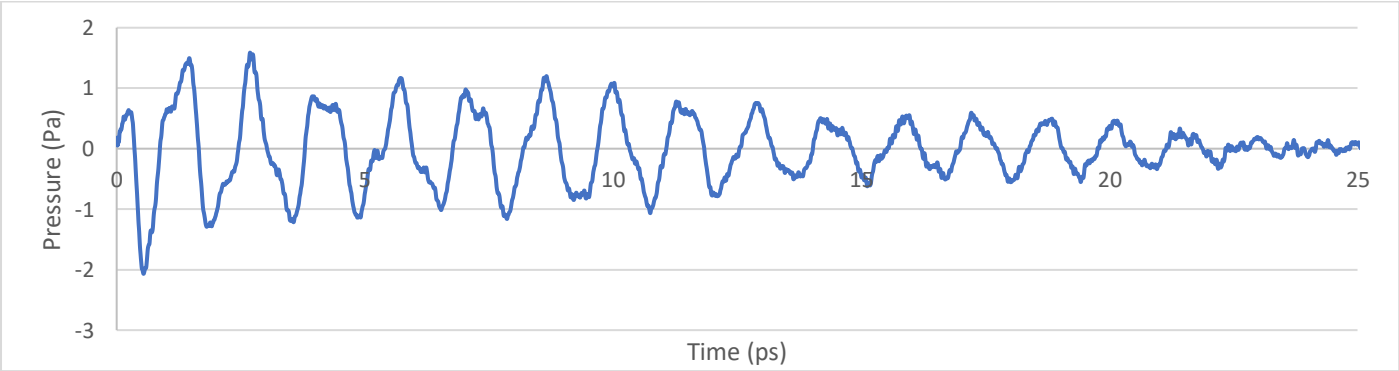

$$\frac{6.037\ ps}{5\ waves} = 1.207\ ps$$

$$\frac{1\ second}{1.207x10^{12}} = 8.285^{-13} Hz$$

$$\frac{8.285^{-13} Hz}{1x10^{-12}} = 0.828\ THz\ (Far\ Infrared\ range)$$

1 second = 10^{-12} ps

1 THz = $1x10^{-12}$Hz

Fourier Transform Analysis - Nanosphere 4nm

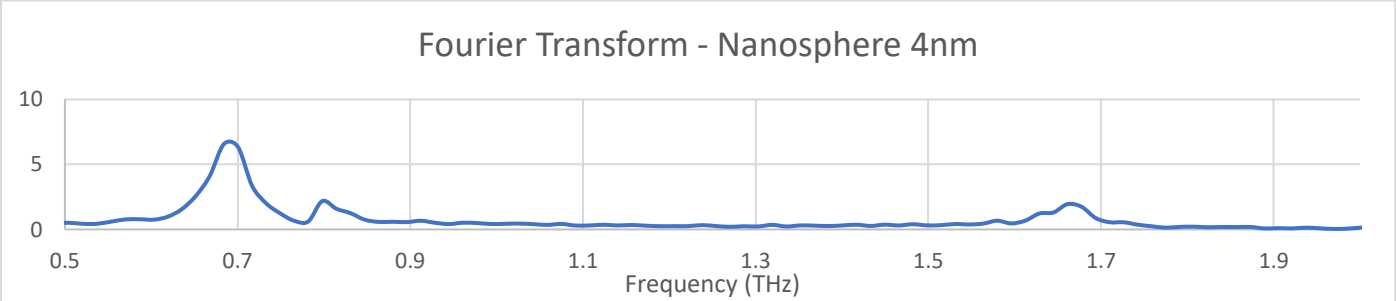

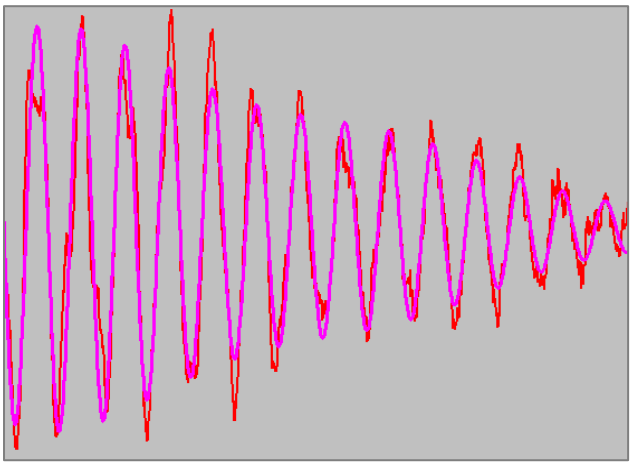

Frequency (Fourier Transform)	
0.689 THz	Dominant peak
0.797 THz	
1.666 THz	
Frequency (Manual Measure)	
0.828 THz	

Nanocylinder 4nm x 2nm (653 Ce) - 250 Å/ps

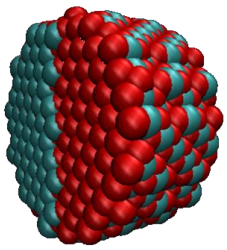

(Initial structure)

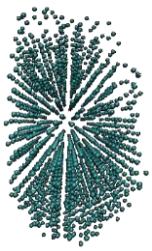

(Crystalline structure)

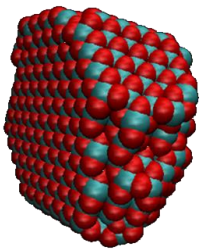

(Final cooled structure)

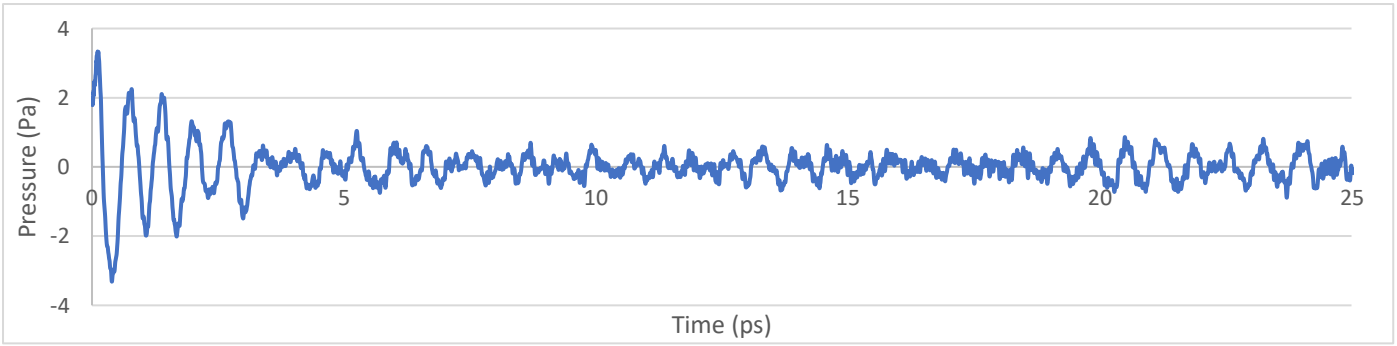

$$\frac{3.25\ ps}{5\ waves} = 0.65\ ps$$

$$\frac{1\ second}{0.65x10^{12}} = 1.538x10^{-12}Hz$$

1 second = 10^{-12} ps

$$\frac{1.538x10^{-12}Hz}{1x10^{-12}} = 1.538\ THz\ (Far\ Infrared\ range)$$

1 THz = $1x10^{-12}$Hz

Fourier Transform Analysis – Nanocylinder 4nm x 2nm

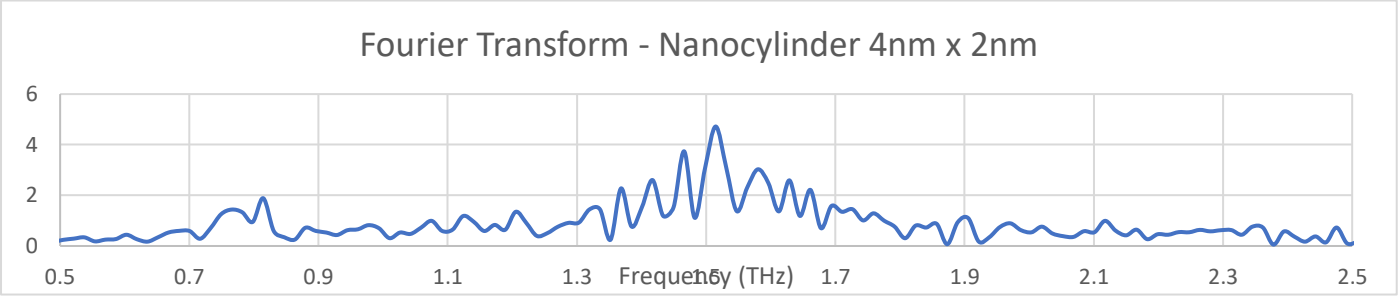

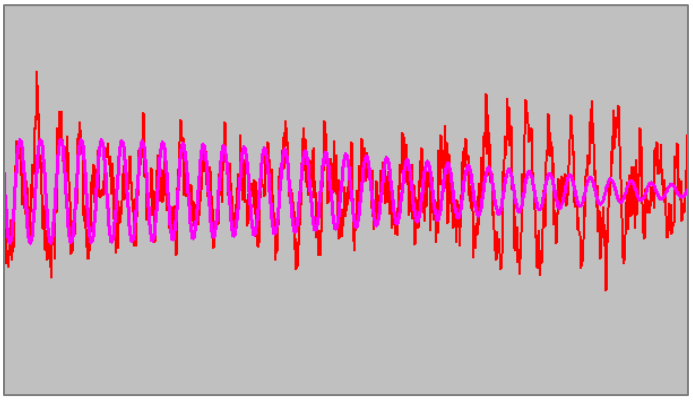

Frequency (Fourier Transform)	
0.814 THz	
1.353 – 1.467 THz	Peak cluster
1.515 THz	Dominant peak
1.578 – 1.662 THz	Peak cluster
Frequency (Manual Measure)	
1.538 THz	

Nanocylinder 4nm x 3nm (954 Ce) - 250 Å/ps

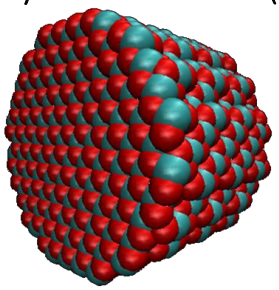

(Initial structure)

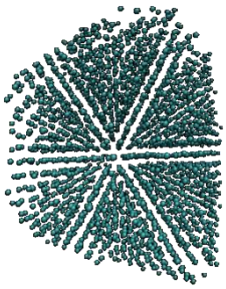

(Crystalline structure)

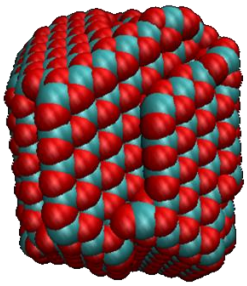

(Final cooled structure)

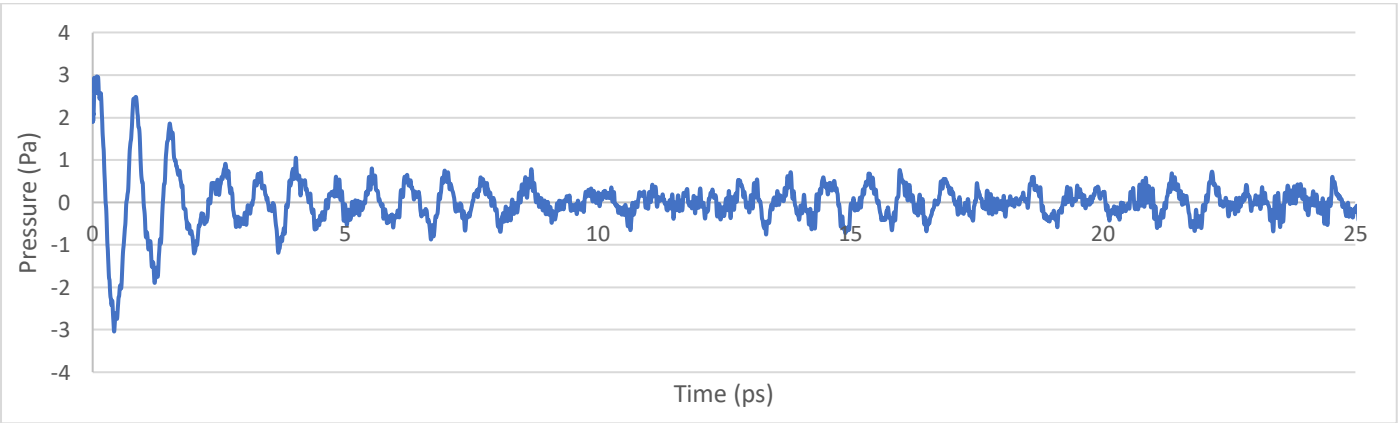

$$\frac{3.962\ ps}{5\ waves} = 0.792\ ps$$

$$\frac{1\ second}{0.792x10^{12}} = 1.262x10^{-12}Hz$$

1 second = 10^{-12} ps

$$\frac{1.262x10^{-12}Hz}{1x10^{-12}} = 1.262\ THz\ (Far\ Infrared\ range)$$

1 THz = $1x10^{-12}$Hz

Fourier Transform Analysis – Nanocylinder 4nm x 3nm

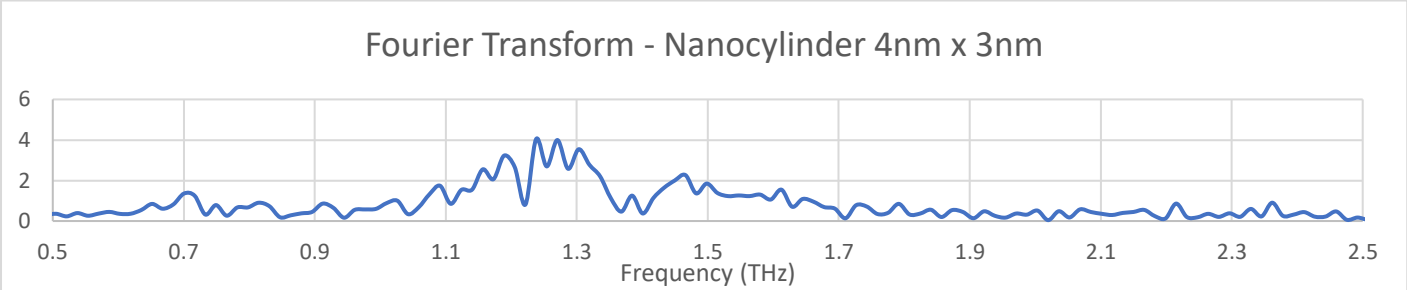

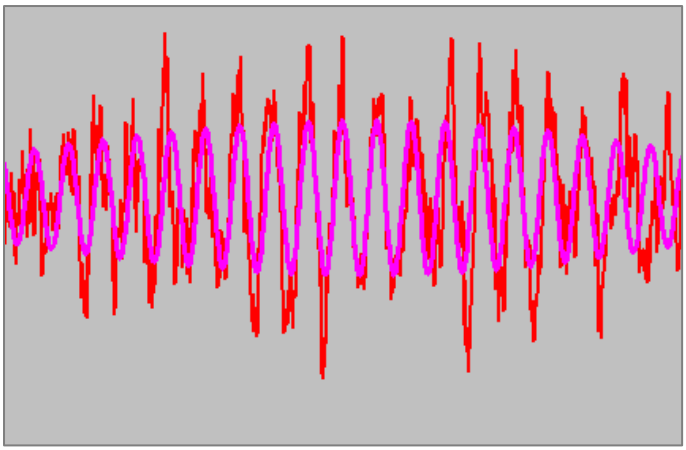

Frequency (Fourier Transform)	
0.716 THz	
1.088 – 1.188 THz	Peak cluster
1.255 THz	Dominant peak
1.467 THz	
Frequency (Manual Measure)	
1.262 THz	

Nanocylinder 4nm x 4nm (1290 Ce) - 250 Å/ps

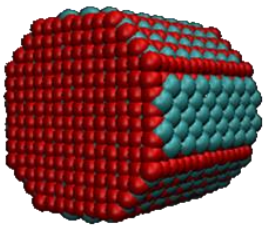

(Initial structure)

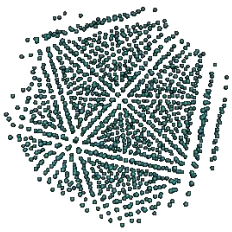

(Crystalline structure)

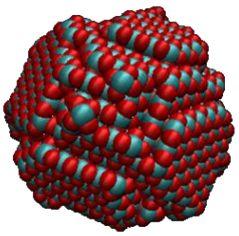

(Final cooled structure)

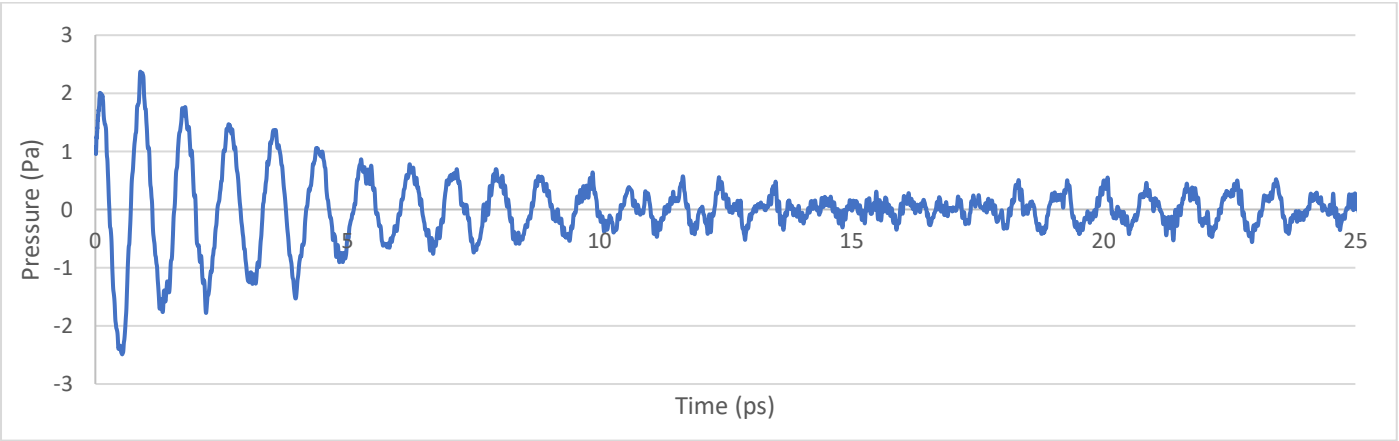

$$\frac{4.387\ ps}{5\ waves} = 0.877\ steps$$

$$\frac{1\ second}{0.877x10^{12}} = 1.140x10^{-12}Hz$$

1 second = 10^{-12} ps

$$\frac{1.140x10^{-12}Hz}{1x10^{-12}} = 1.140\ THz\ (Far\ Infrared\ range)$$

1 THz = $1x10^{-12}$Hz

Fourier Transform Analysis – Nanocylinder 4nm x 4nm

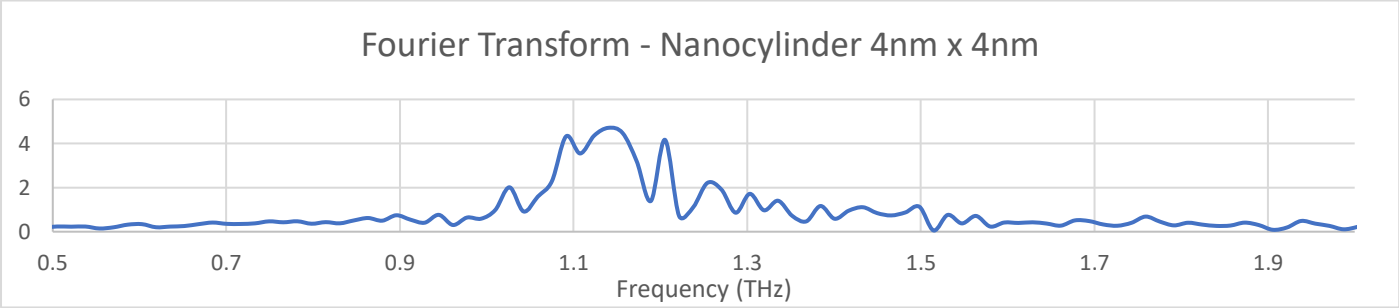

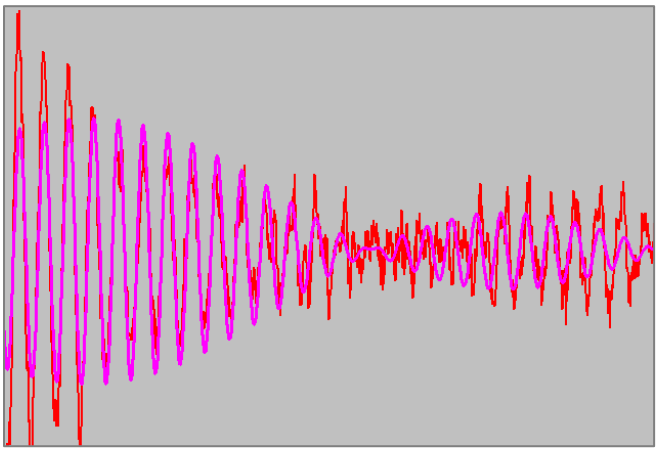

Frequency (Fourier Transform)	
1.140 THz	Dominant peak
1.204 THz	
Frequency (Manual Measure)	
1.140 THz	

Nanocylinder 4nm x 5nm (1604 Ce) - 250 Å/ps

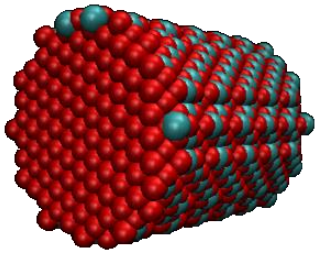

(Initial structure)

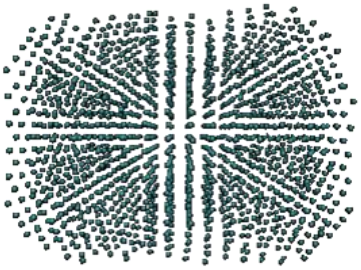

(Crystalline structure)

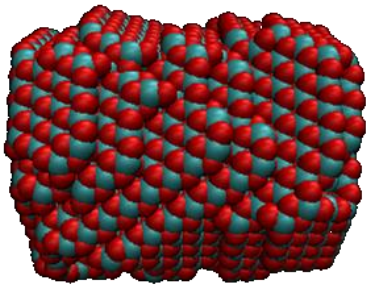

(Final cooled structure)

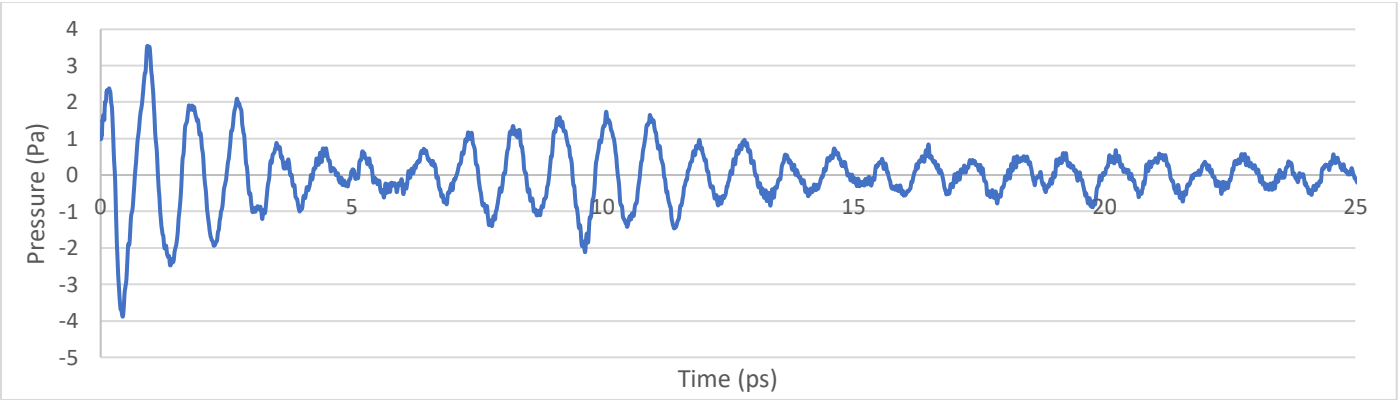

$$\frac{4.425\ ps}{5\ waves} = 0.885\ ps$$

$$\frac{1\ second}{0.885x10^{12}} = 1.129x10^{-13}Hz$$

1 second = 10^{-12} ps

$$\frac{1.129x10^{-13}Hz}{1x10^{-12}} = 1.129\ THz\ (Far\ Infrared\ range)$$

1 THz = $1x10^{-12}$Hz

Fourier Transform Analysis – Nanocylinder 4nm x 5nm

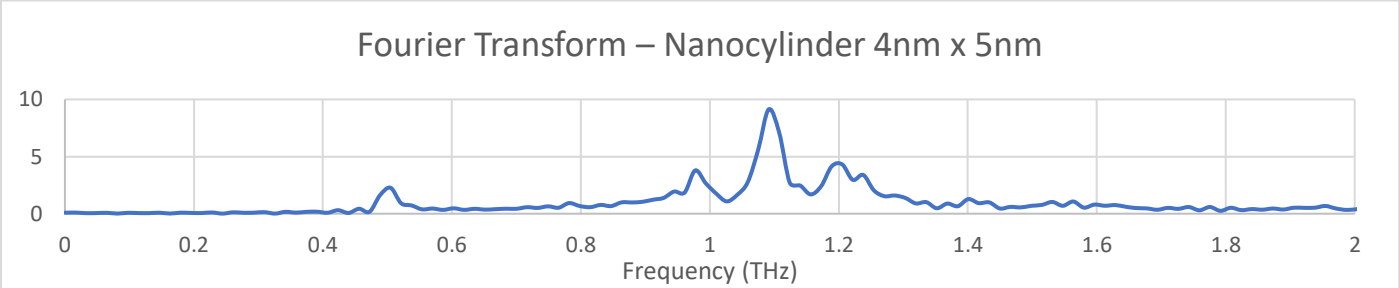

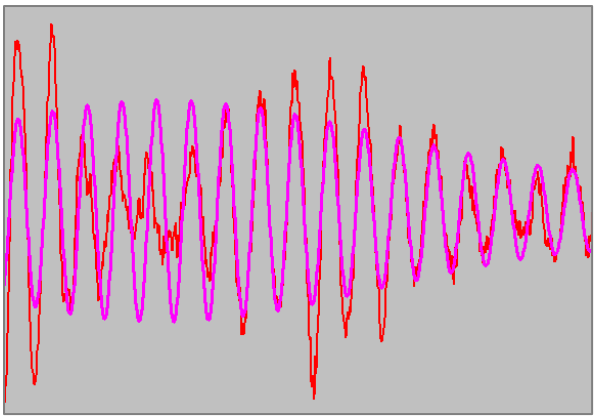

Frequency (Fourier Transform)	
0.502 THz	
0.976 THz	
1.092 THz	Dominant peak
1.204 THz	
Frequency (Manual Measure)	
1.129 THz	

Nanocylinder 4nm x 6nm (1905 Ce) - 250 Å/ps

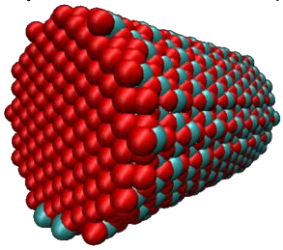

(Initial structure)

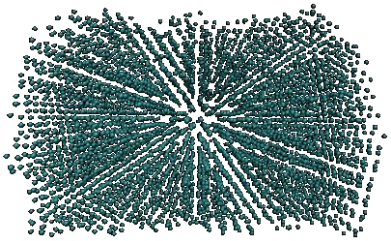

(Crystalline structure)

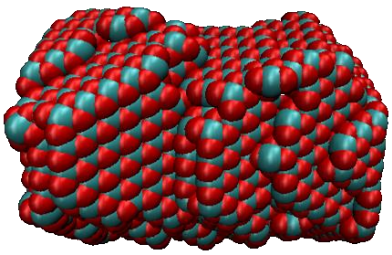

(Final cooled structure)

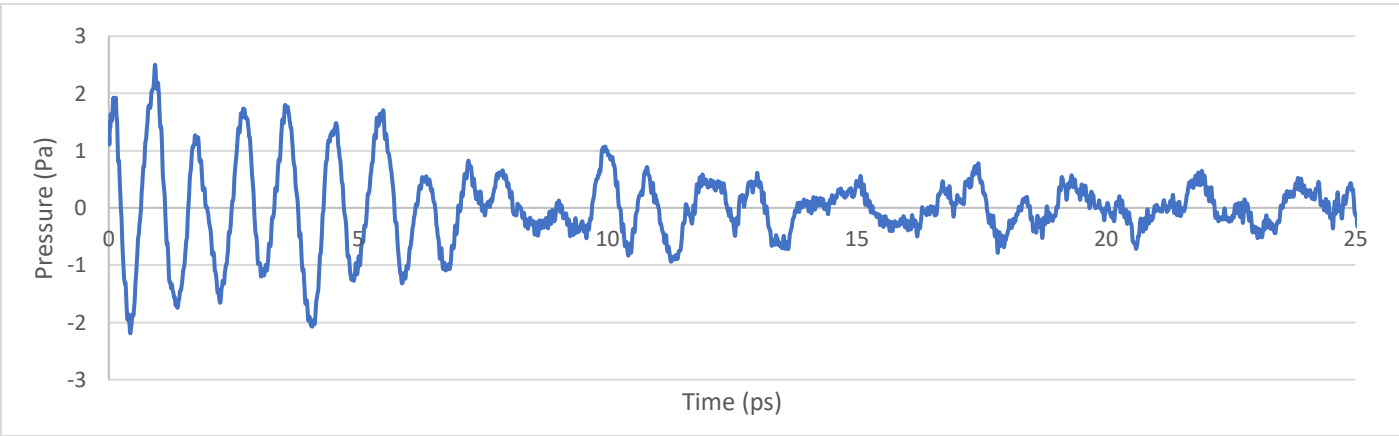

$$\frac{4.575\ ps}{5\ waves} = 0.915\ ps$$

$$\frac{1\ second}{0.915x10^{12}} = 1.092x10^{-12}Hz$$

1 second = 10^{-12} ps

$$\frac{1.092x10^{-12}Hz}{1x10^{-12}} = 1.092\ THz\ (Far\ Infrared\ range)$$

1 THz = $1x10^{-12}$Hz

Fourier Transform Analysis – Nanocylinder 4nm x 6nm

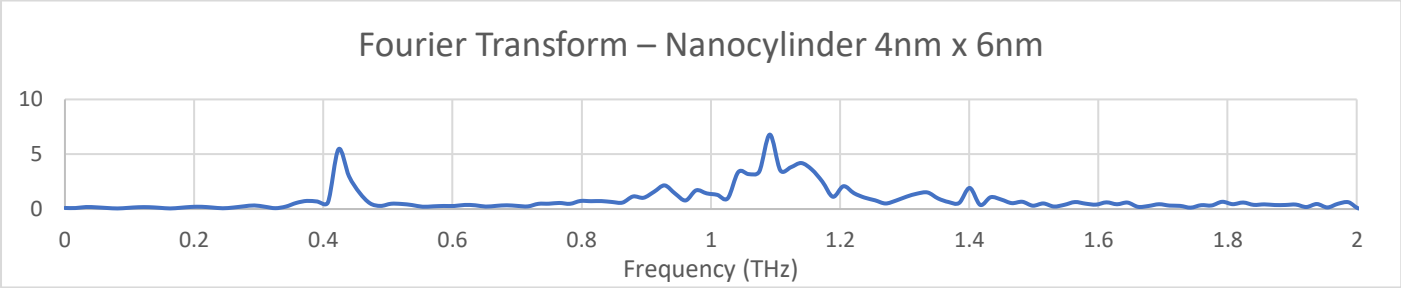

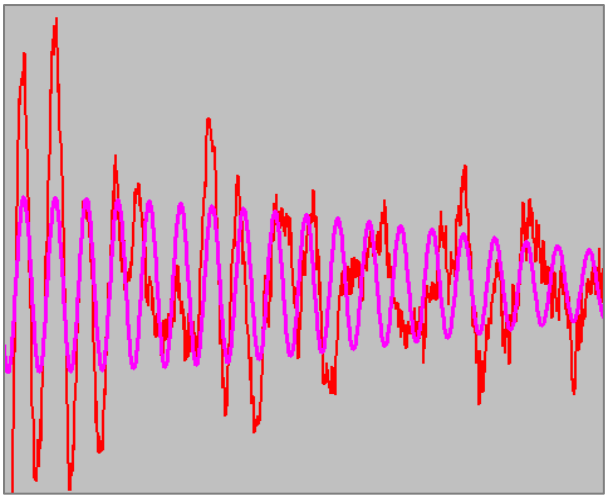

Frequency (Fourier Transform)	
0.422 THz	
1.092 THz	Dominant peak
1.4 THz	
Frequency (Manual Measure)	
1.092 THz	

Nanocylinder 4nm x 7nm (2257 Ce) - 250 Å/ps

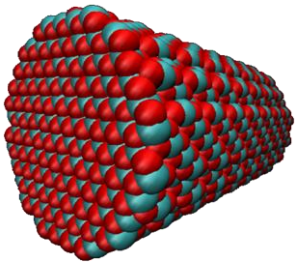

(Initial structure)

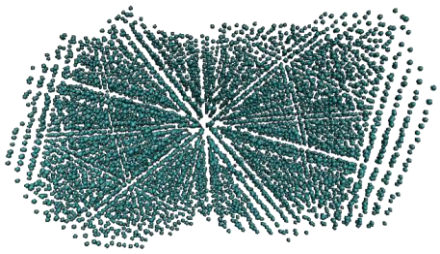

(Crystalline structure)

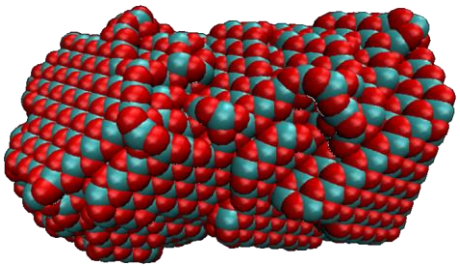

(Final cooled structure)

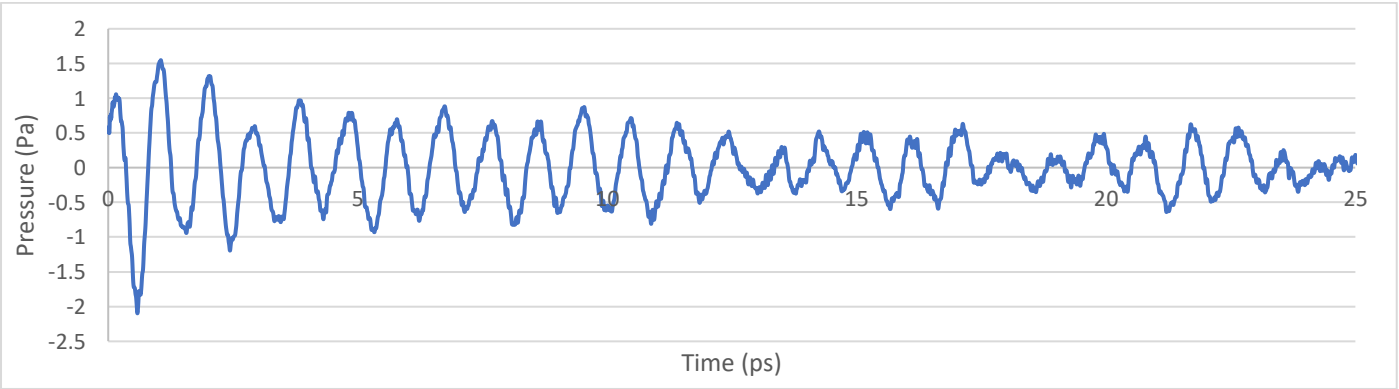

$$\frac{4.737\ ps}{5\ waves} = 0.947\ ps$$

$$\frac{1\ second}{0.947x10^{12}} = 1.055x10^{-12}Hz$$

1 second = 10^{-12} ps

$$\frac{1.055x10^{-12}Hz}{1x10^{-12}} = 1.055\ THz\ (Far\ Infrared\ range)$$

1 THz = $1x10^{-12}$Hz

Fourier Transform Analysis – Nanocylinder 4nm x 7nm

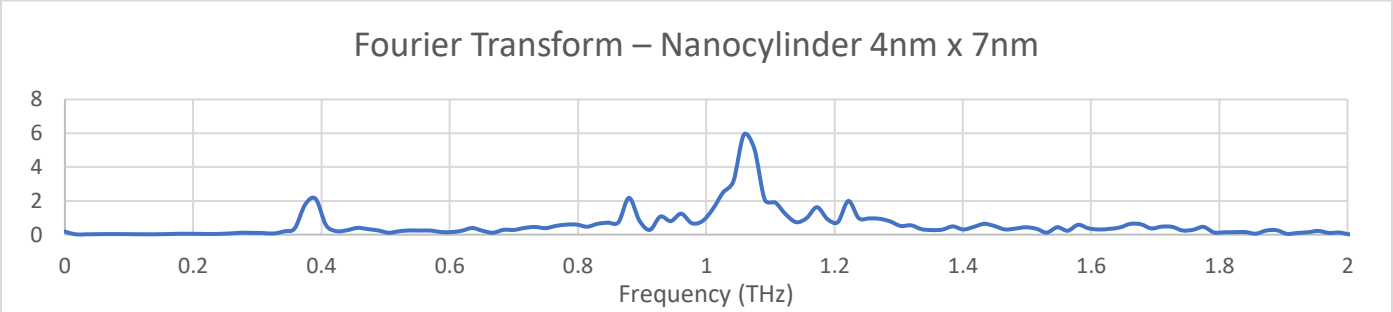

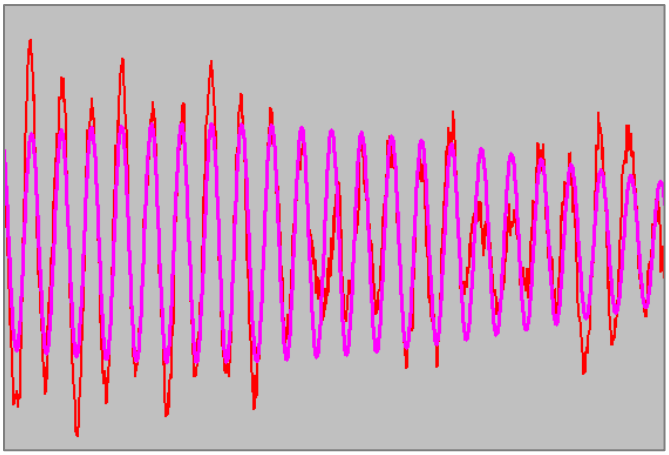

Frequency (Fourier Transform)	
0.39 THz	
0.881 THz	
1.06 THz	Dominant peak
1.22 THz	
Frequency (Manual Measure)	
1.055 THz	

Nanocylinder 6nm x 2nm (1458 Ce) - 250 Å/ps

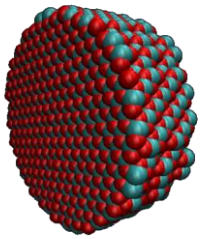

(Initial structure)

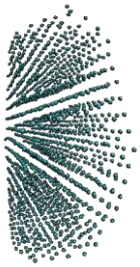

(Crystalline structure)

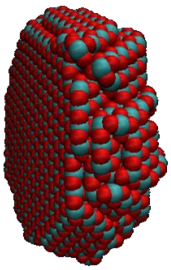

(Final cooled structure)

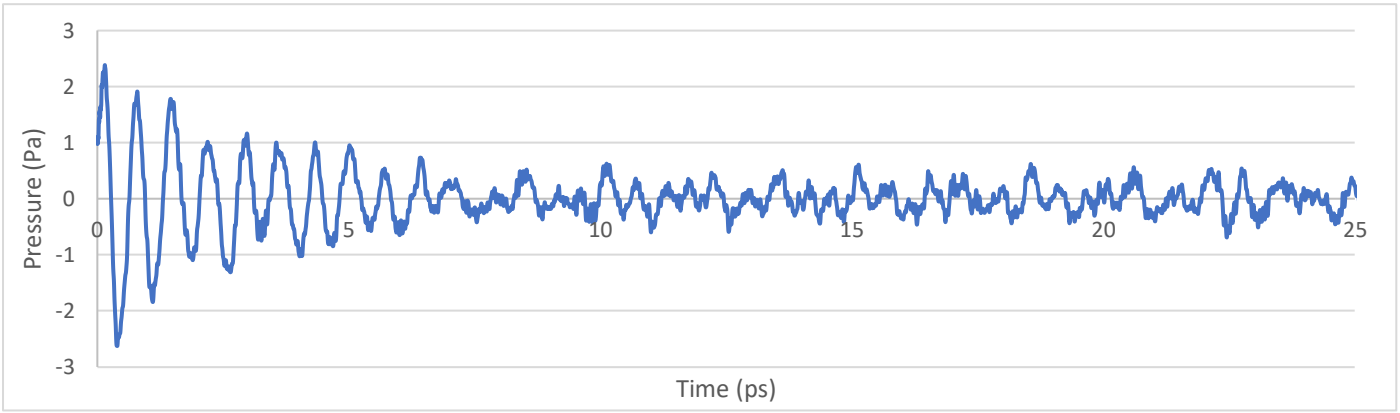

$$\frac{3.375\ ps}{5\ waves} = 0.675\ ps$$

$$\frac{1\ second}{0.675x10^{12}} = 1.481^{-12}Hz$$

1 second = 10^{-12} ps

$$\frac{1.481^{-12}Hz}{1x10^{-12}} = 1.481\ THz\ (Far\ Infrared\ range)$$

1 THz = $1x10^{-12}$Hz

Fourier Transform Analysis – Nanocylinder 6nm x 2nm

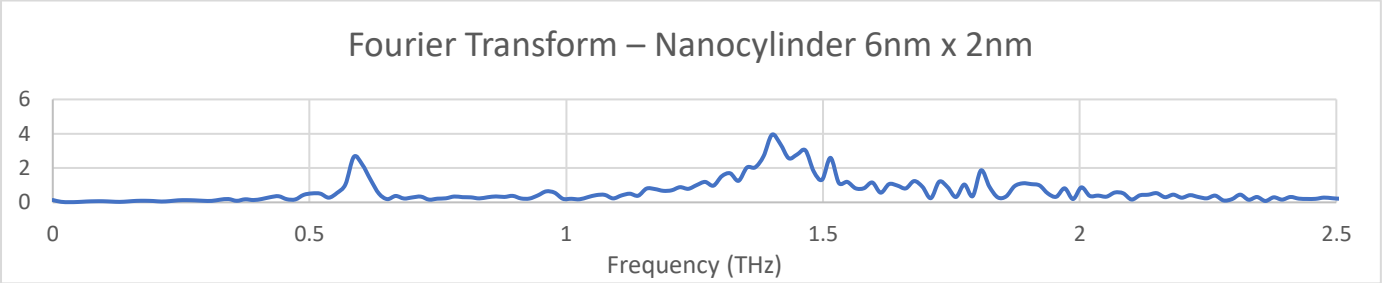

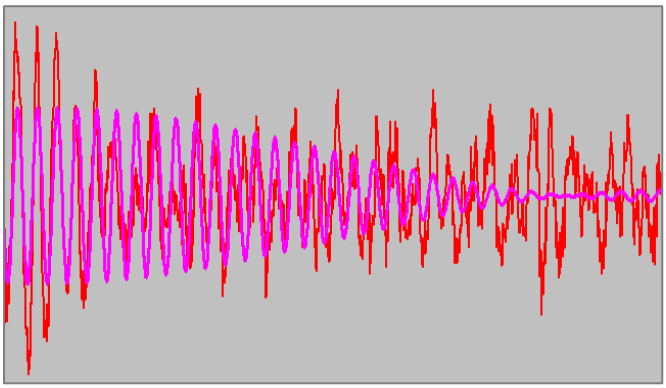

Frequency (Fourier Transform)	
0.586 THz	
1.399 THz	Dominant peak
1.806 THz	
Frequency (Manual Measure)	
1.481 THz	

Nanocylinder 6nm x 3nm (2131 Ce) - 250 Å/ps

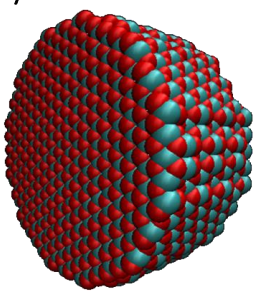

(Initial structure)

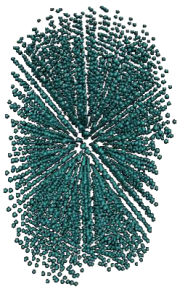

(Crystalline structure)

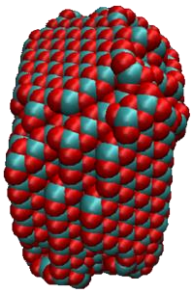

(Final cooled structure)

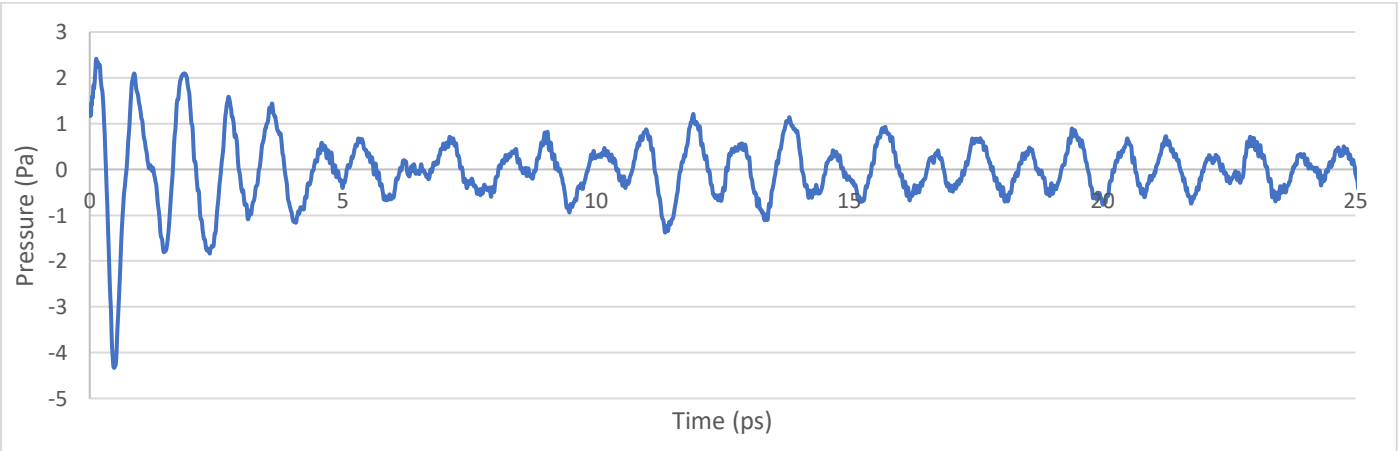

$$\frac{4.487\ ps}{5\ waves} = 0.897\ ps$$

$$\frac{1\ second}{0.897x10^{12}} = 1.114x10^{-12}Hz$$

1 second = 10^{-12} ps

$$\frac{1.114x10^{-12}Hz}{1x10^{-12}} = 1.114\ THz\ (Far\ Infrared\ range)$$

1 THz = $1x10^{-12}$Hz

Fourier Transform Analysis – Nanocylinder 6nm x 3nm

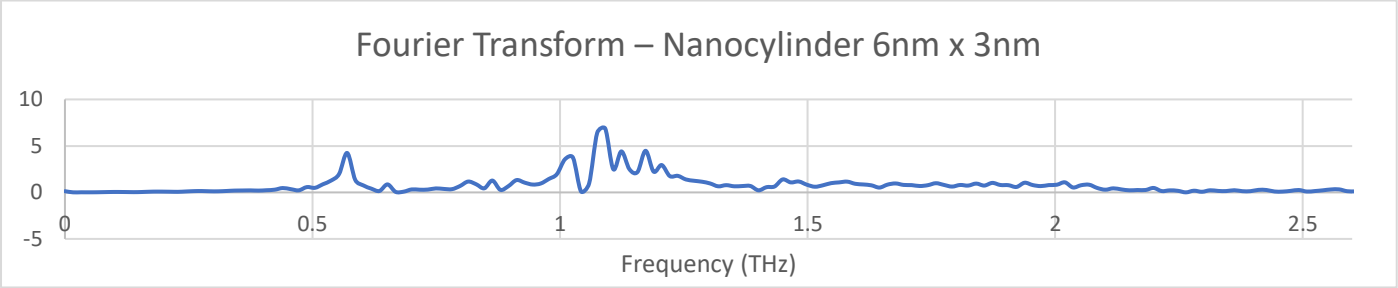

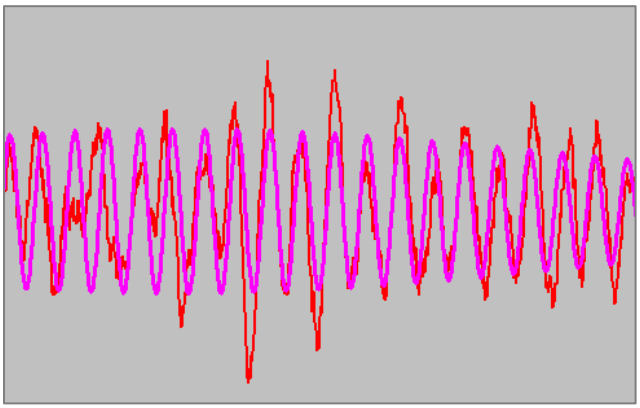

Frequency (Fourier Transform)	
0.570 THz	
1.020 THz	
1.091 THz	Dominant peak
1.172 THz	
Frequency (Manual Measure)	
1.114 THz	

Nanocylinder 6nm x 4nm (2916 Ce) - 250 Å/ps

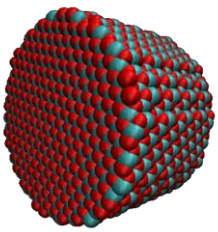

(Initial structure)

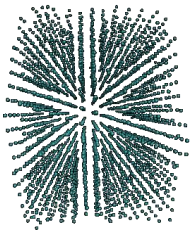

(Crystalline structure)

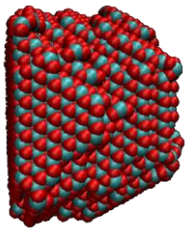

(Final cooled structure)

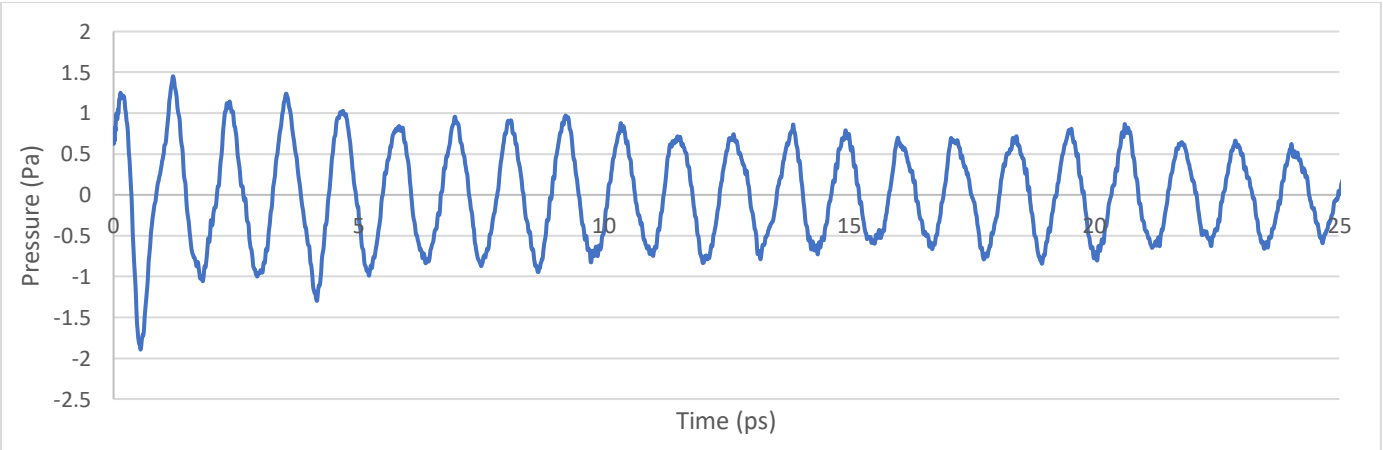

$$\frac{5.8\ ps}{5\ waves} = 1.16\ ps$$

$$\frac{1\ second}{1.16x10^{12}} = 8.696^{-13} Hz$$

1 second = 10^{-12} ps

$$\frac{8.696^{-13} Hz}{1x10^{-12}} = 0.869\ THz\ (Far\ Infrared\ range)$$

1 THz = $1x10^{-12}$Hz

Fourier Transform Analysis – Nanocylinder 6nm x 4nm

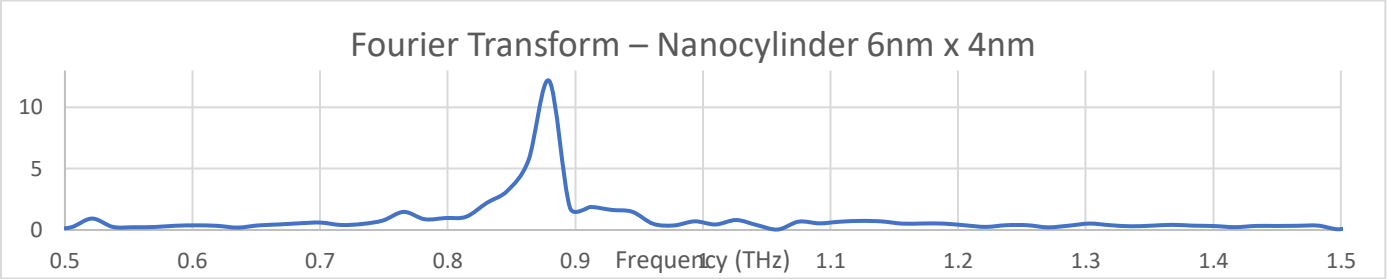

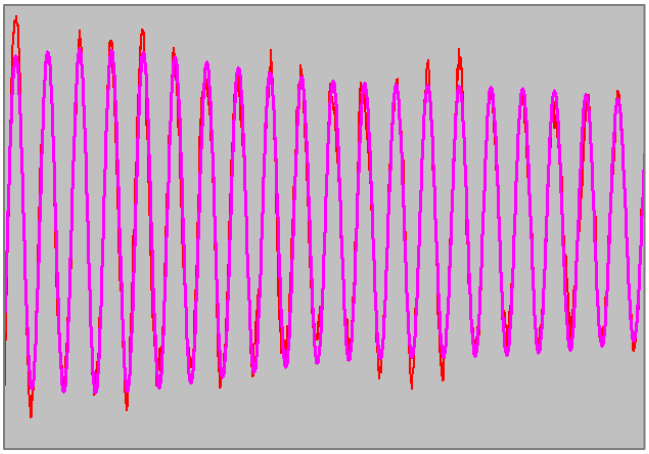

Frequency (Fourier Transform)	
0.521 THz	Minor peak
0.881 THz	Dominant peak
Frequency (Manual Measure)	
0.869 THz	

Nanocylinder 6nm x 5nm (3589 Ce) - 250 Å/ps

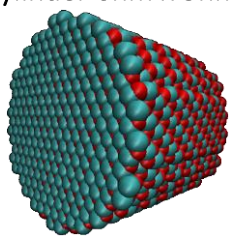

(Initial structure)

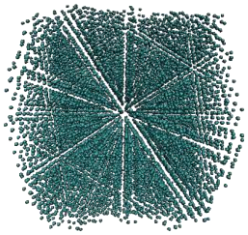

(Crystalline structure)

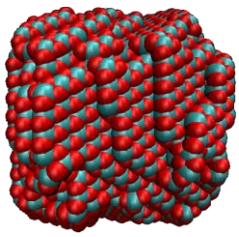

(Final cooled structure)

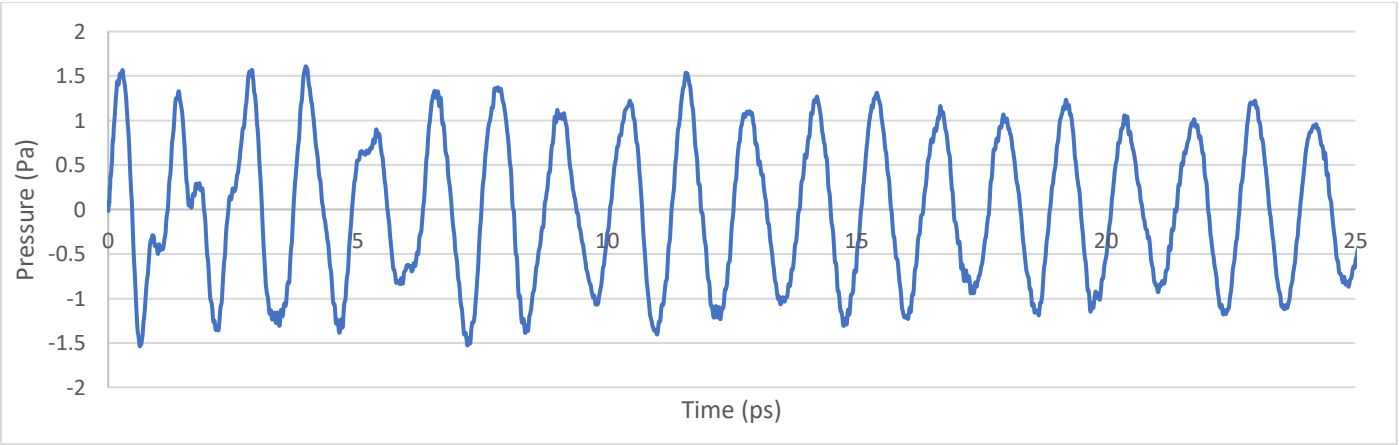

$$\frac{6.262\ ps}{5\ waves} = 1.252\ ps$$

$$\frac{1\ second}{1.252x10^{12}} = 7.987x10^{-13}Hz$$

1 second = 10^{-12} ps

$$\frac{7.987x10^{-13}Hz}{1x10^{-12}} = 0.798\ THz\ (Far\ Infrared\ range)$$

1 THz = $1x10^{-12}$Hz

Fourier Transform Analysis – Nanocylinder 6nm x 5nm

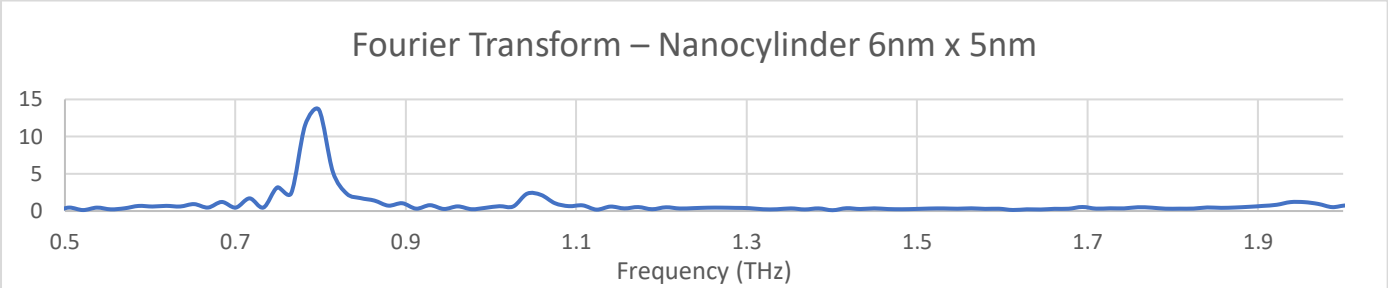

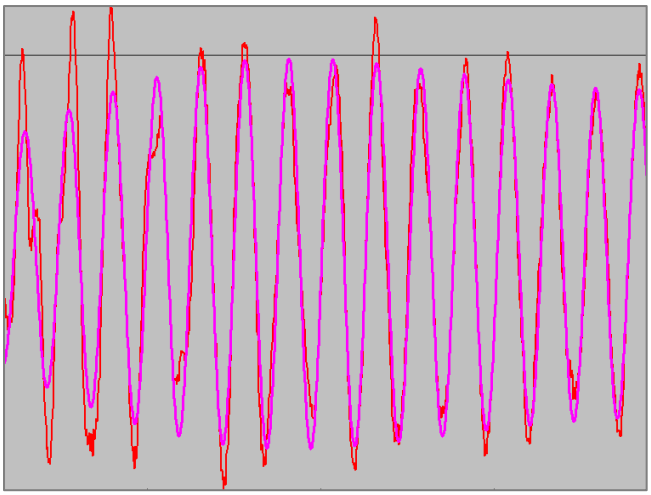

Frequency (Fourier Transform)	
0.796 THz	Dominant peak
1.046 THz	
1.951 THz	Broad
Frequency (Manual Measure)	
0.798 THz	

Nanocylinder 6nm **x 6nm** (4262 Ce**)** - 250 Å/ps

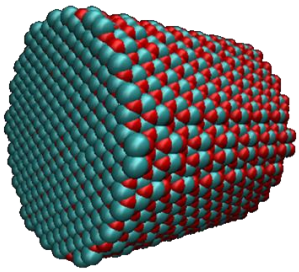

(Initial structure)

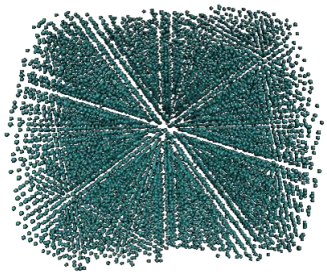

(Crystalline structure)

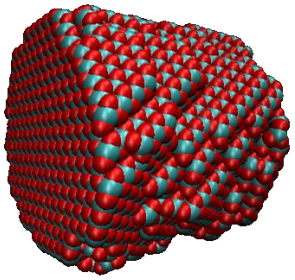

(Final cooled structure)

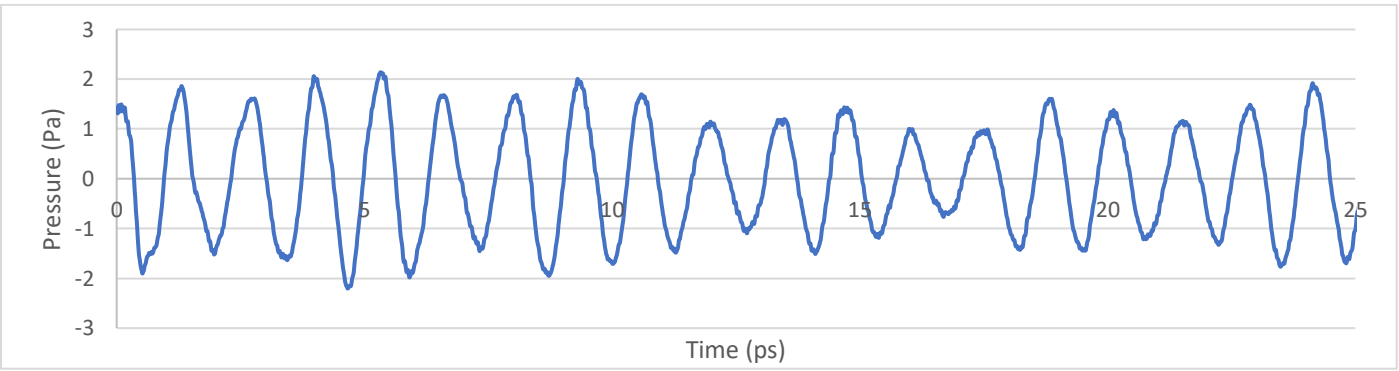

$$\frac{6.7\ ps}{5\ waves} = 1.34\ ps$$

$$\frac{1\ second}{1.34x10^{12}} = 7.463^{-13} Hz$$

1 second = 10^{-12} ps

$$\frac{7.463^{-13} Hz}{1x10^{-12}} = 0.746\ THz\ (Far\ Infrared\ range)$$

1 THz = $1x10^{-12}$Hz

Fourier Transform Analysis – Nanocylinder 6nm x 6nm

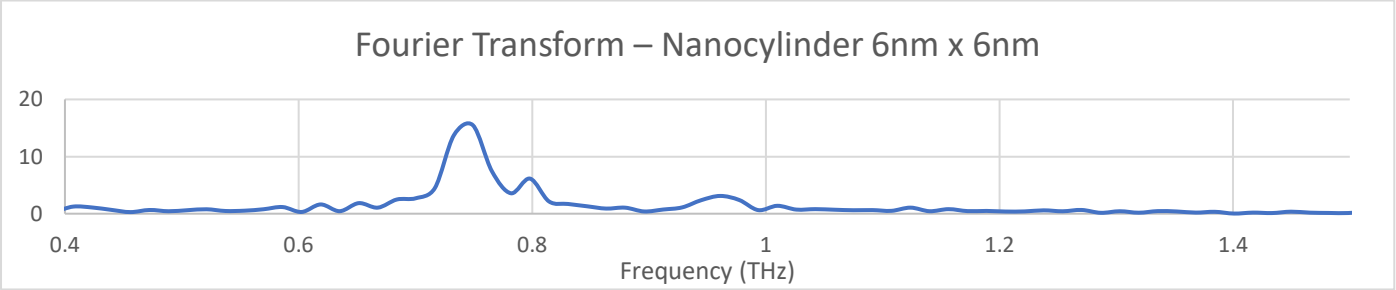

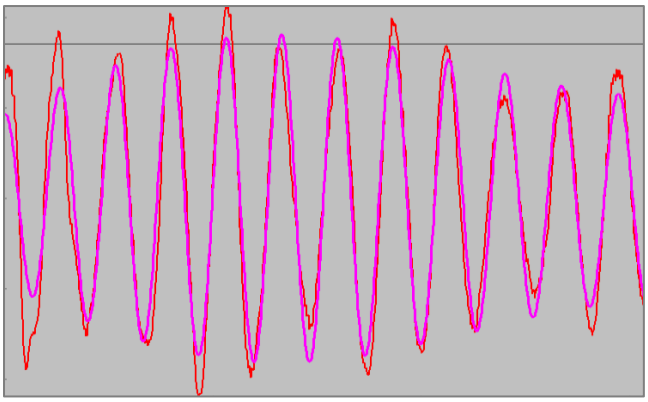

Frequency (Fourier Transform)	
0.744 THz	Dominant peak
0.961 THz	
Frequency (Manual Measure)	
0.746 THz	

Nanocylinder 7nm x 2nm (1979 Ce) - 250 Å/ps

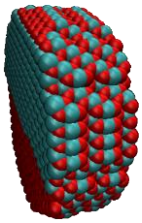

(Initial structure)

(Crystalline structure)

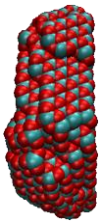

(Final cooled structure)

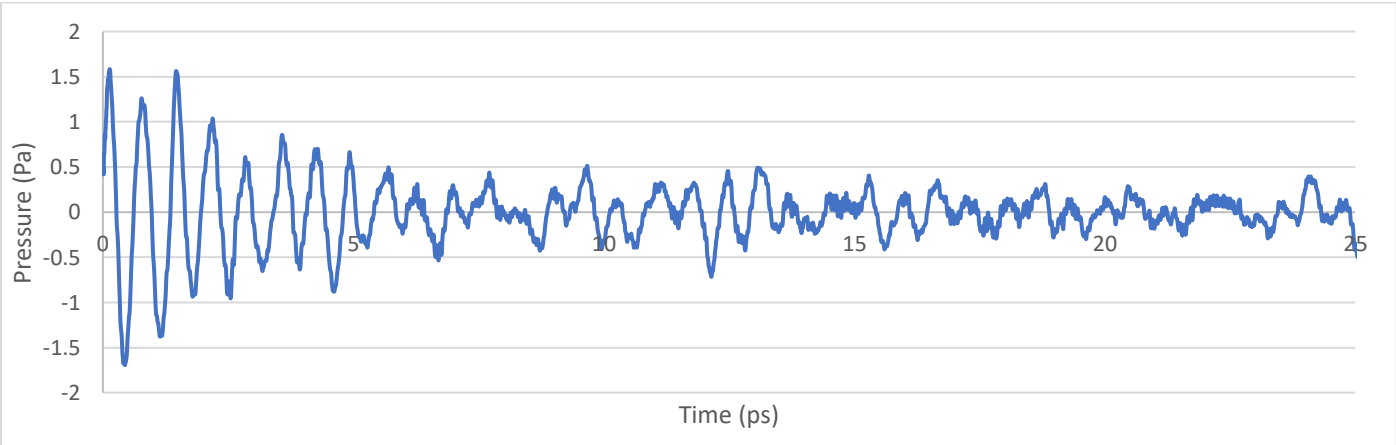

$$\frac{3.525\ ps}{5\ waves} = 0.705\ ps$$

$$\frac{1\ second}{0.705x10^{12}} = 1.418x10^{-12}Hz$$

1 second = 10^{-12} ps

$$\frac{1.418x10^{-12}Hz}{1x10^{-12}} = 1.418\ THz\ (Far\ Infrared\ range)$$

1 THz = $1x10^{-12}$Hz

Fourier Transform Analysis – Nanocylinder 7nm x 2nm

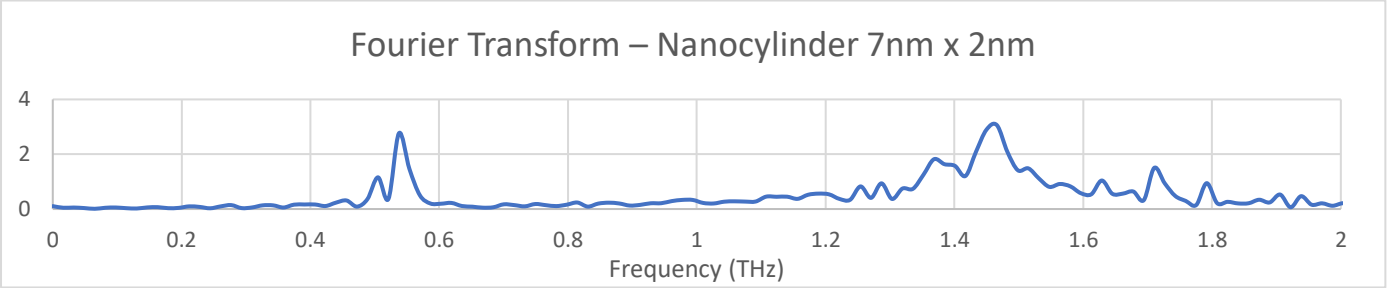

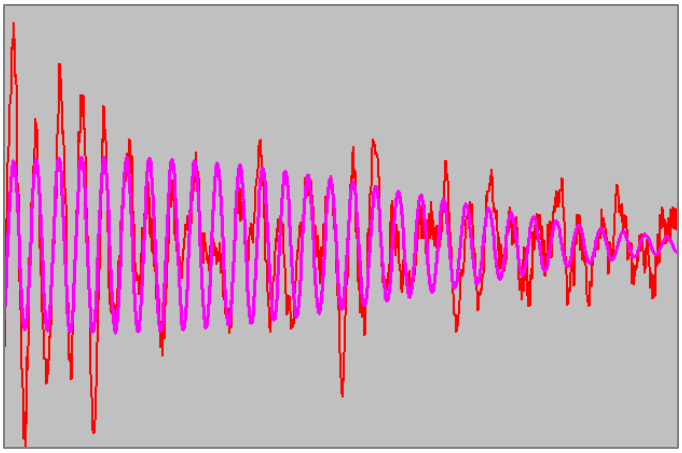

Frequency (Fourier Transform)	
0.536 THz	
1.466 THz	Dominant peak
1.709 THz	
Frequency (Manual Measure)	
1.418 THz	

Nanocylinder 7nm x 3nm (2892 Ce) - 250 Å/ps

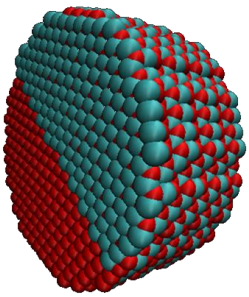

(Initial structure)

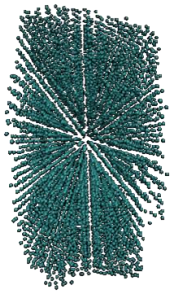

(Crystalline structure)

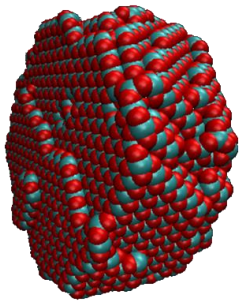

(Final cooled structure)

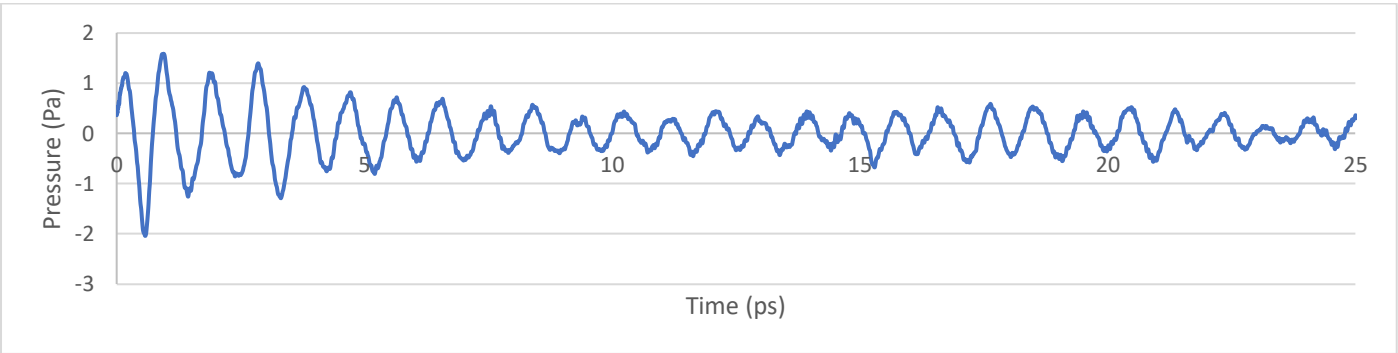

$$\frac{4.7\ ps}{5\ waves} = 0.94\ ps$$

$$\frac{1\ second}{0.94x10^{12}} = 1.064^{-12} Hz$$

1 second = 10^{-12} ps

$$\frac{1.064^{-12} Hz}{1x10^{-12}} = 1.064\ THz\ (Far\ Infrared\ range)$$

1 THz = $1x10^{-12}$Hz

Fourier Transform Analysis – Nanocylinder 7nm x 3nm

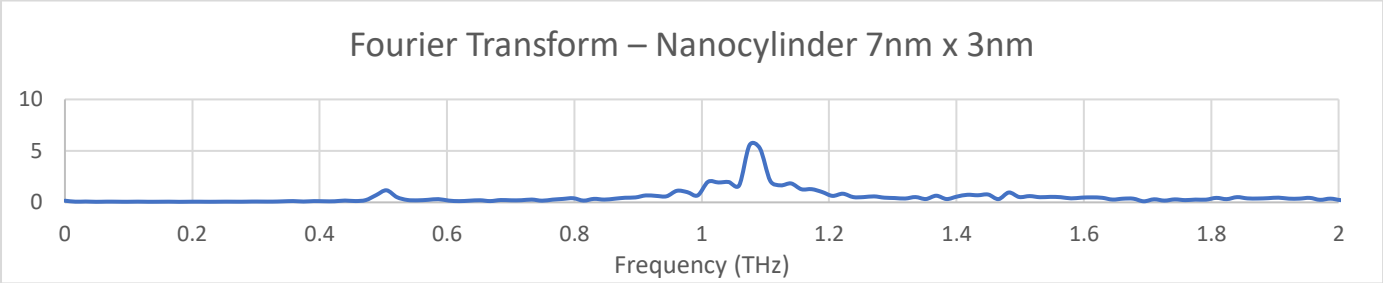

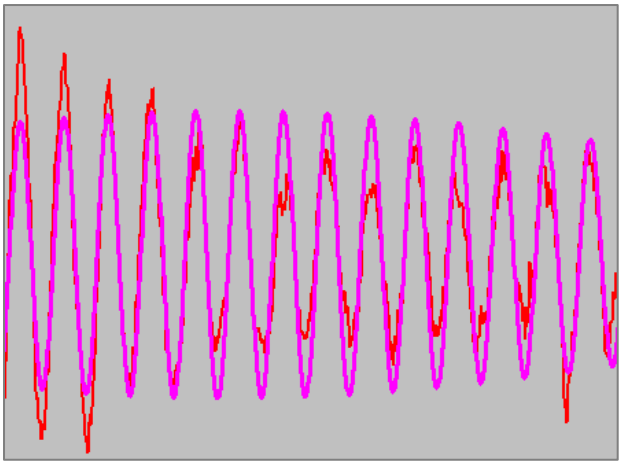

Frequency (Fourier Transform)	
0.506 THz	
1.076 THz	Dominant peak
Frequency (Manual Measure)	
1.064 THz	

Nanocylinder 7nm x 4nm (3955 Ce) - 250 Å/ps

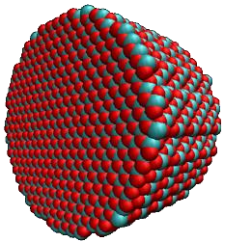

(Initial structure)

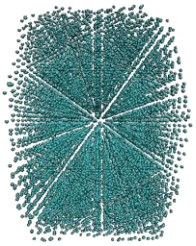

(Crystalline structure)

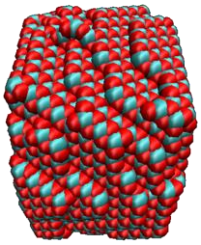

(Final cooled structure)

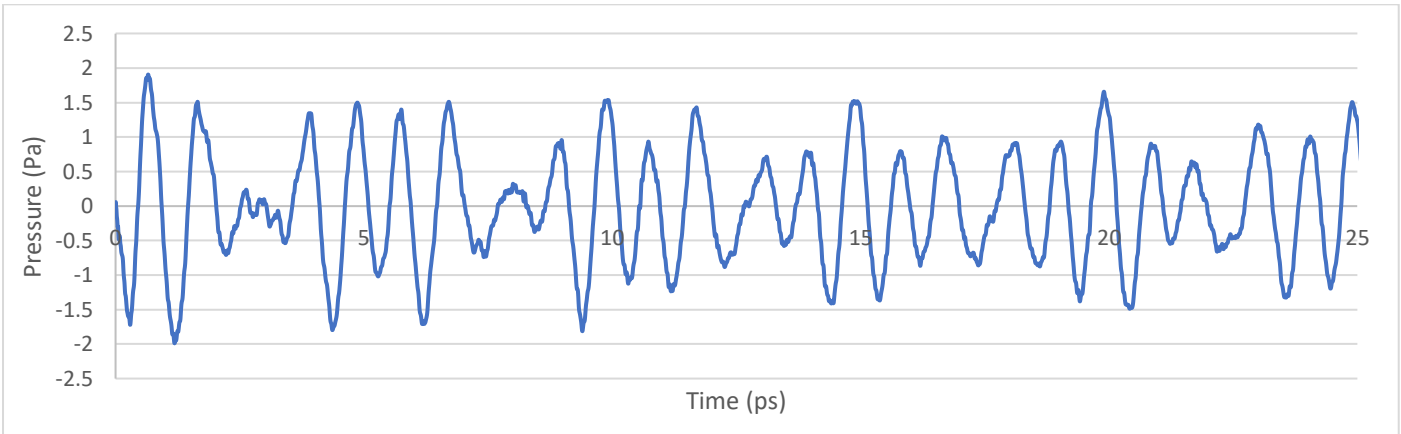

$$\frac{6.35\ ps}{5\ waves} = 1.27\ ps$$

$$\frac{1\ second}{1.27x10^{12}} = 7.874x10^{-13}Hz$$

1 second = 10^{-12} ps

$$\frac{7.874x10^{-13}Hz}{1x10^{-12}} = 0.787\ THz\ (Far\ Infrared\ range)$$

1 THz = $1x10^{-12}$Hz

Fourier Transform Analysis – Nanocylinder 7nm x 4nm

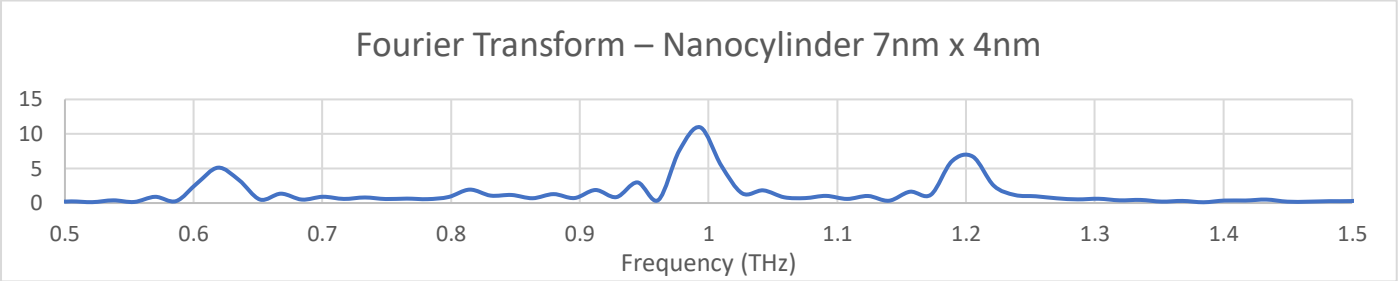

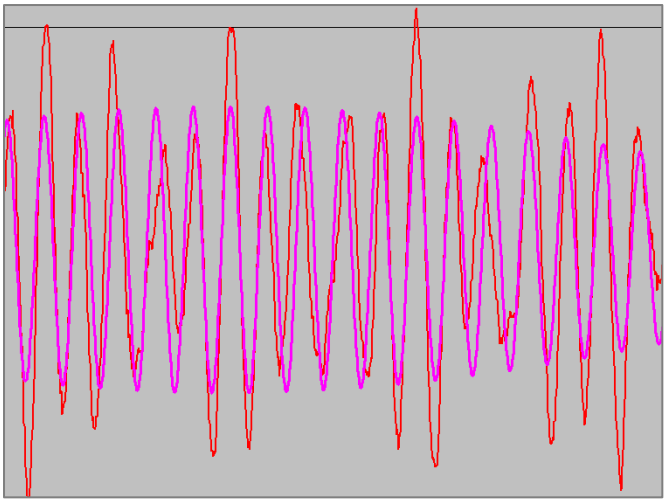

Frequency (Fourier Transform)	
0.619 THz	
0.993 THz	Dominant peak
1.207 THz	
Frequency (Manual Measure)	
0.787 THz	

Nanocylinder 7nm x 5nm (4868 Ce) - 250 Å/ps

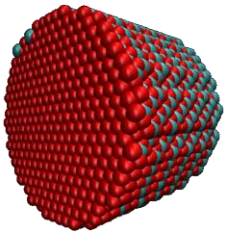

(Initial structure)

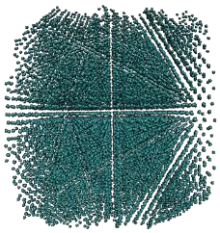

(Crystalline structure)

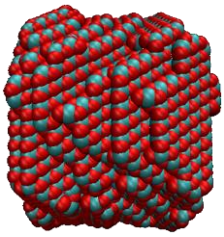

(Final cooled structure)

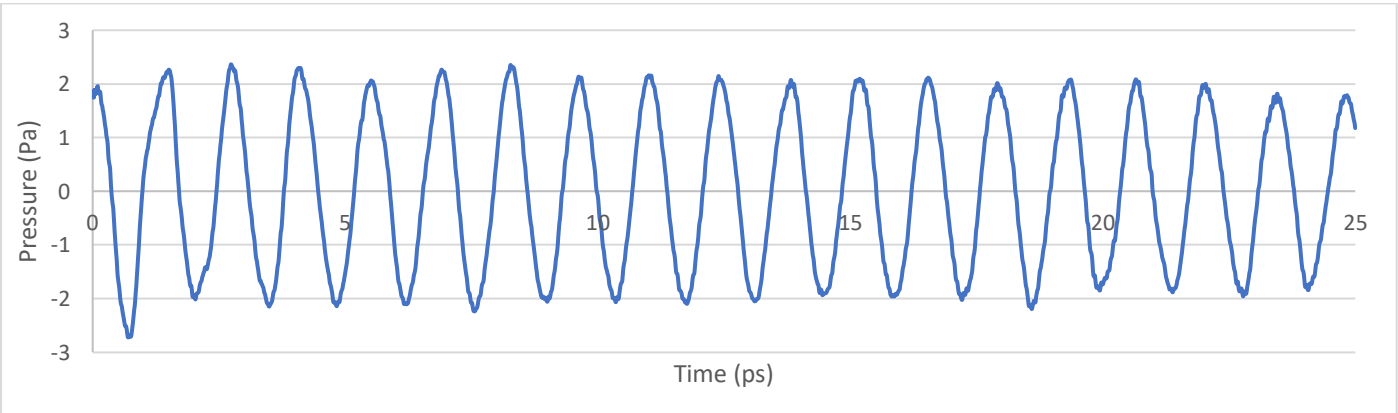

$$\frac{6.775\ ps}{5\ waves} = 1.36\ ps$$

$$\frac{1\ second}{1.36x10^{12}} = 7.353x10^{-13}Hz$$

1 second = 10^{-12} ps

$$\frac{7.353x10^{-13}Hz}{1x10^{-12}} = 0.735\ THz\ (Far\ Infrared\ range)$$

1 THz = $1x10^{-1}$Hz

Fourier Transform Analysis – Nanocylinder 7nm x 5nm

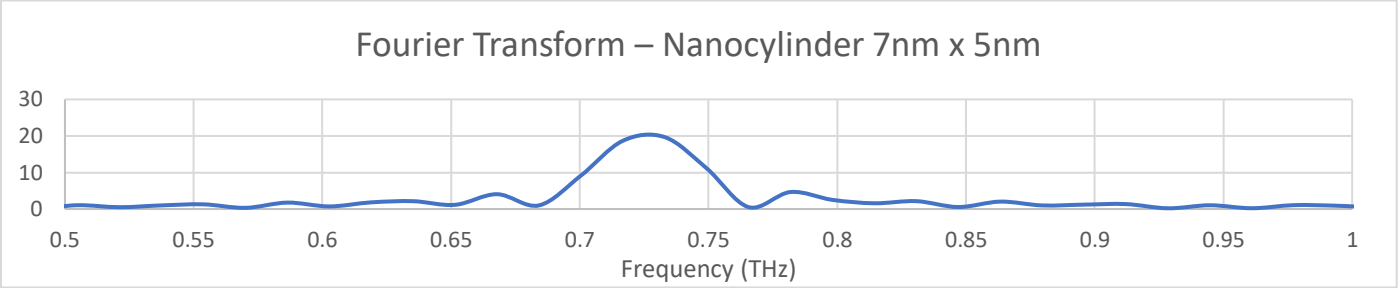

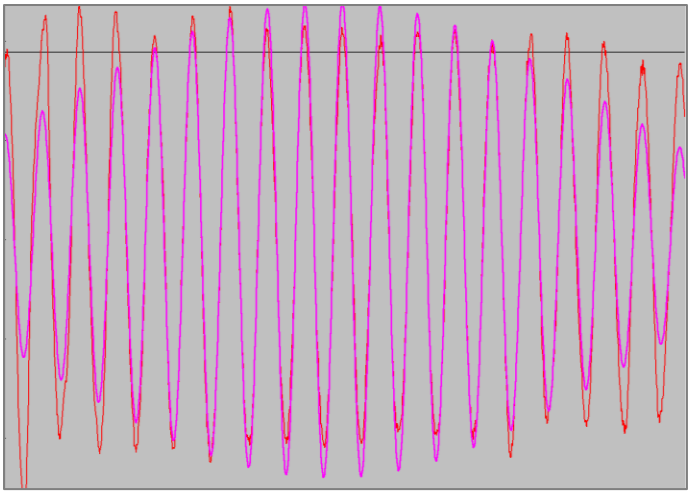

Frequency (Fourier Transform)	
0.732 THz	Dominant peak
Frequency (Manual Measure)	
0.735 THz	

Nanocylinder 7nm x 6nm (5781 Ce) - 250 Å/ps

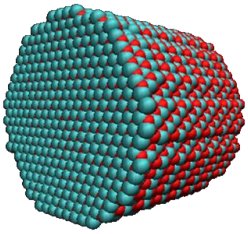

(Initial structure)

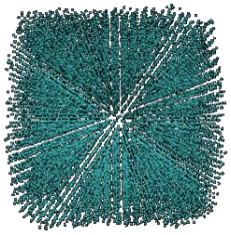

(Crystalline structure)

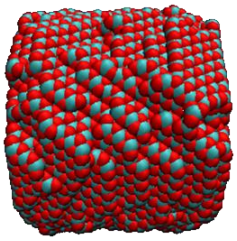

(Final cooled structure)

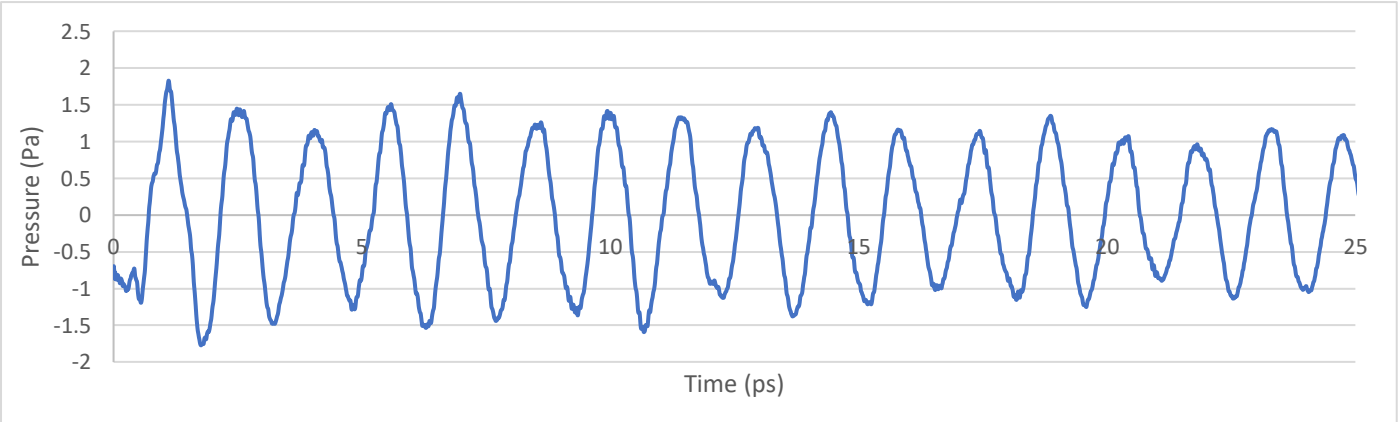

$$\frac{7.375\ ps}{5\ waves} = 1.475\ ps$$

$$\frac{1\ second}{1.475x10^{12}} = 6.779^{-13} Hz$$

1 second = 10^{-12} ps

$$\frac{6.779^{-13} Hz}{1x10^{-12}} = 0.677\ THz\ (Far\ Infrared\ range)$$

1 THz = $1x10^{-12}$Hz

Fourier Transform Analysis – Nanocylinder 7nm x 6nm

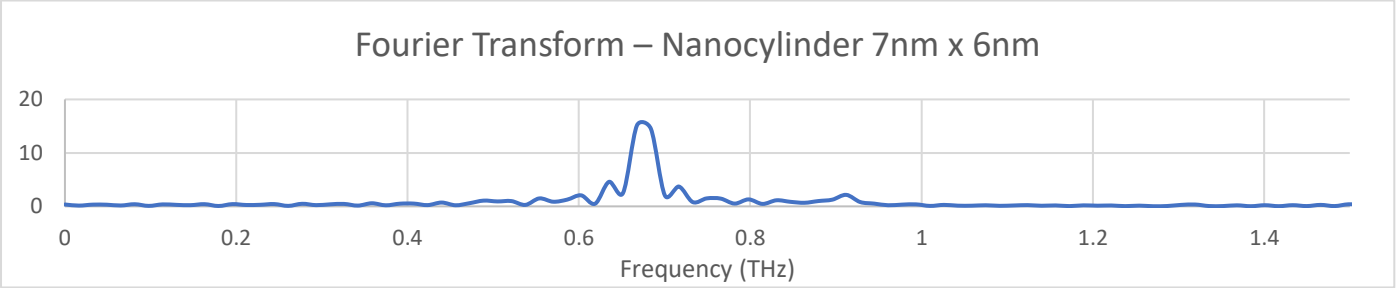

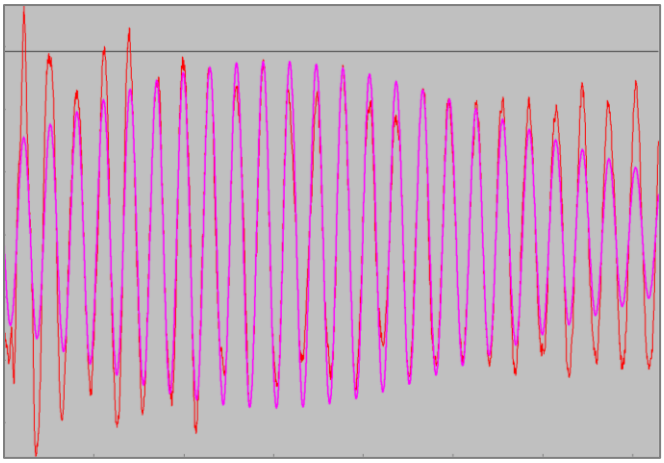

Frequency (Fourier Transform)	
0.671 THz	Dominant peak
Frequency (Manual Measure)	
0.677 THz	

Nanocylinder 7nm x 7nm (6721 Ce) - 250Å/ps

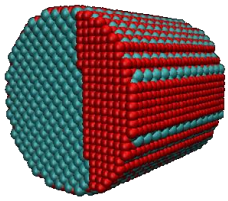

(Initial structure)

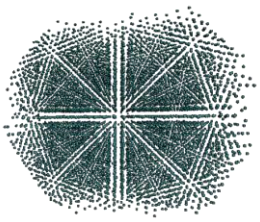

(Crystalline structure)

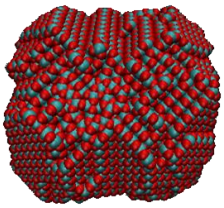

(Final cooled structure)

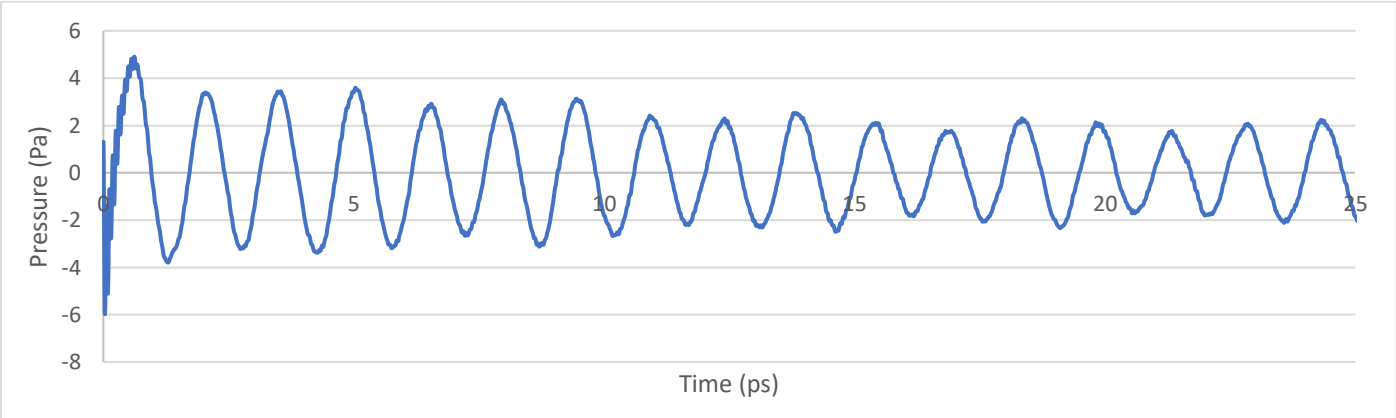

$$\frac{7.462\ ps}{5\ waves} = 1.492\ ps$$

$$\frac{1\ second}{1.492x10^{12}} = 6.702^{-13} Hz$$

1 second = 10^{-12} ps

$$\frac{6.702^{-13} Hz}{1x10^{-12}} = 0.670\ THz\ (Far\ Infrared\ range)$$

1 THz = $1x10^{-12}$Hz

Fourier Transform Analysis – Nanocylinder 7nm x 7nm

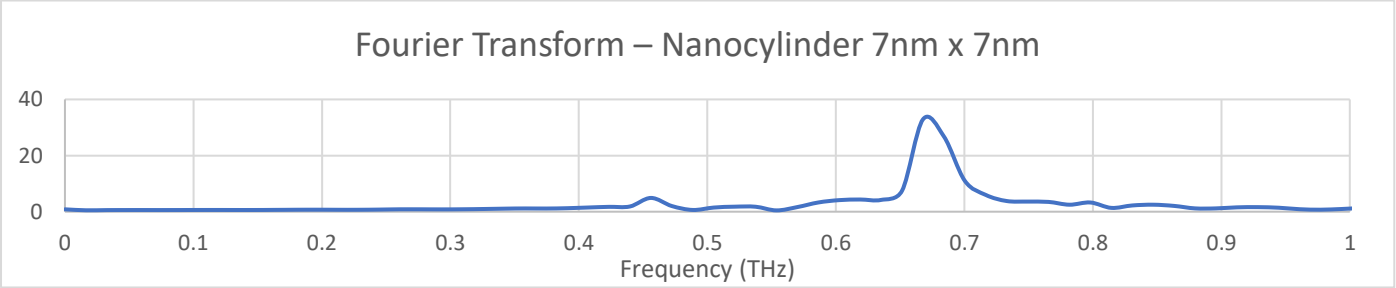

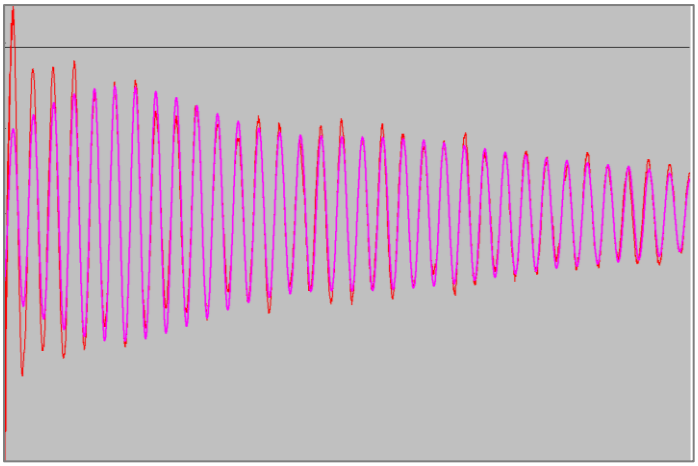

Frequency (Fourier Transform)	
0.667 THz	Dominant peak
Frequency (Manual Measure)	
0.670 THz	

Nanocylinder 8nm x 2nm (2576 Ce) - 250 Å/ps

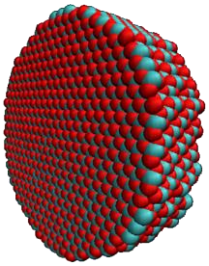

(Initial structure)

(Crystalline structure)

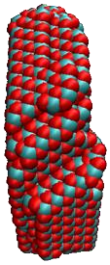

(Final cooled structure)

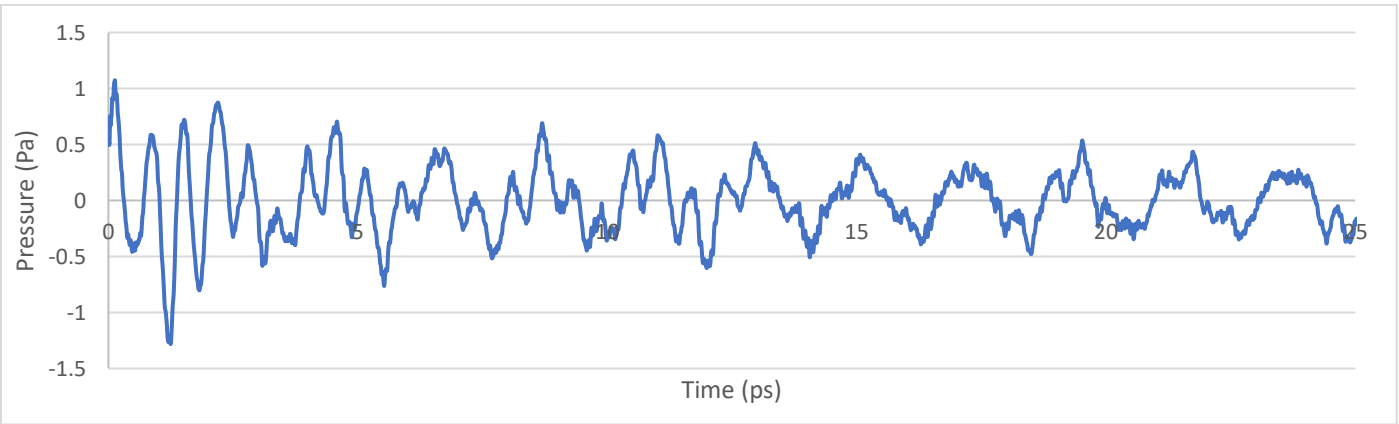

$$\frac{3.737\ ps}{5\ waves} = 0.747\ ps$$

$$\frac{1\ second}{0.747x10^{12}} = 1.338^{-12}Hz$$

1 second = 10^{-12} ps

$$\frac{1.338^{-12}Hz}{1x10^{-12}} = 1.338\ THz\ (Far\ Infrared\ range)$$

1 THz = $1x10^{-12}$Hz

Fourier Transform Analysis – Nanocylinder 8nm x 2nm

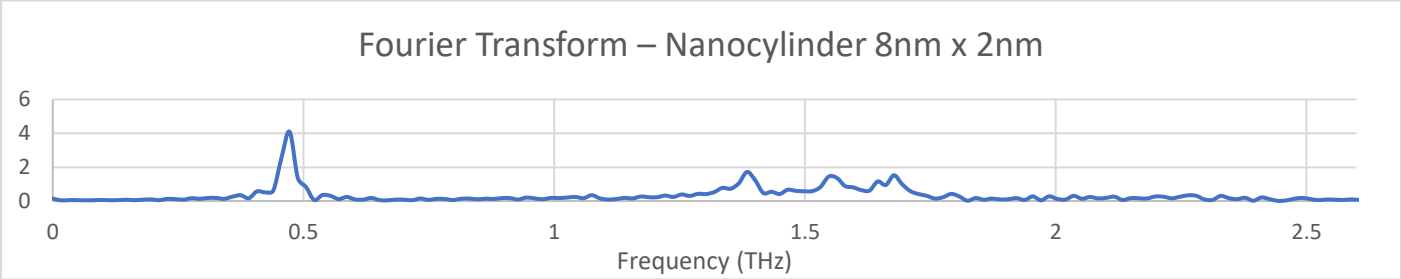

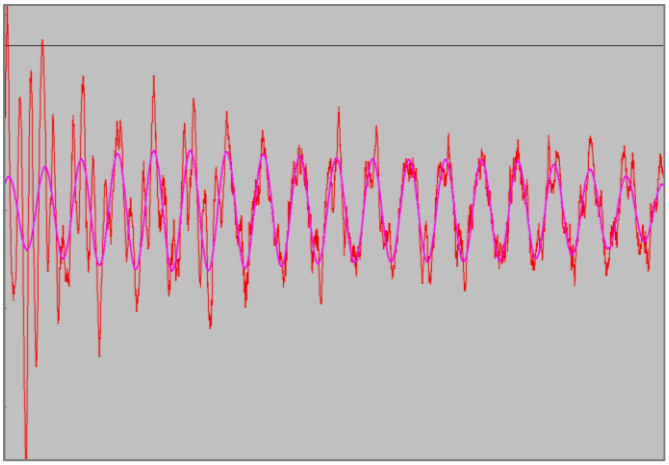

Frequency (Fourier Transform)	
0.470 THz	Dominant peak
1.383 THz	
1.550 THz	
1.678 THz	
Frequency (Manual Measure)	
1.338 THz	

Nanocylinder 10nm x 2nm (4047 Ce) - 250 Å/ps

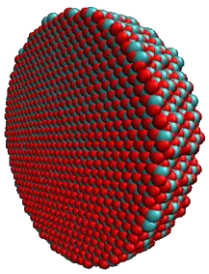

(Initial structure)

(Crystalline structure)

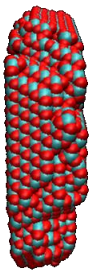

(Final cooled structure)

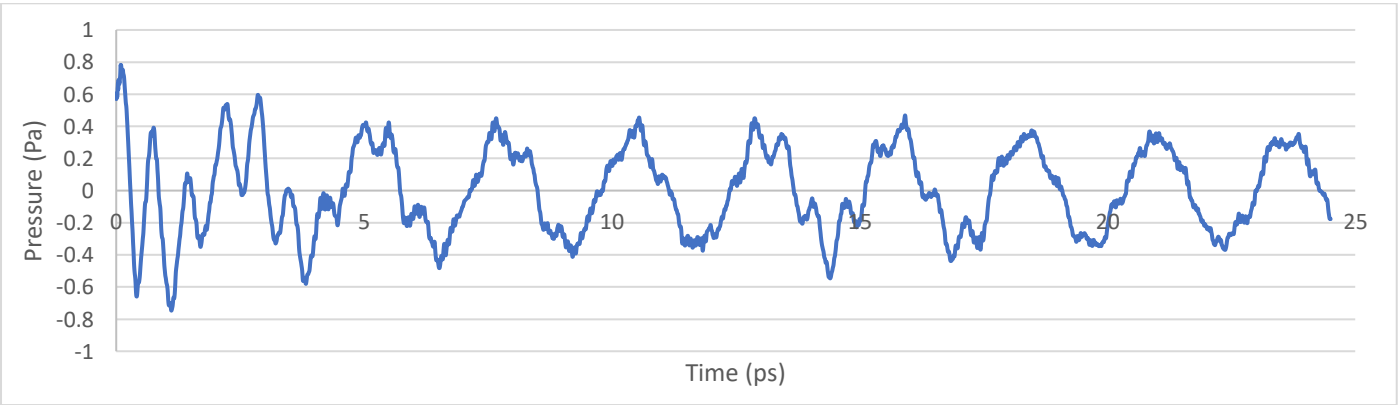

$\frac{4.587\ ps}{5\ waves} = 0.917\ ps$

$\frac{1\ second}{0.917x10^{12}} = 1.090^{-12} Hz$

1 second = 10^{-12} ps

$\frac{1.090^{-12} Hz}{1x10^{-12}} = 1.090\ THz\ (Far\ Infrared\ range)$

1 THz = $1x10^{-12}$Hz

Fourier Transform Analysis – Nanocylinder 10nm x 2nm

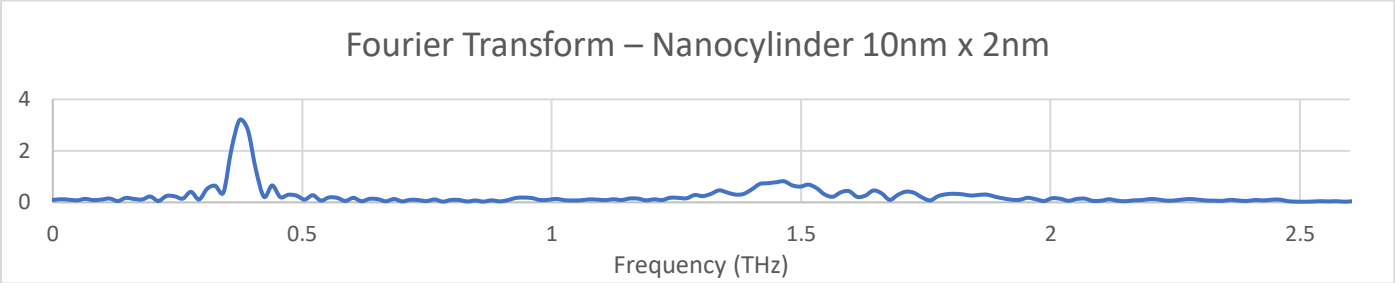

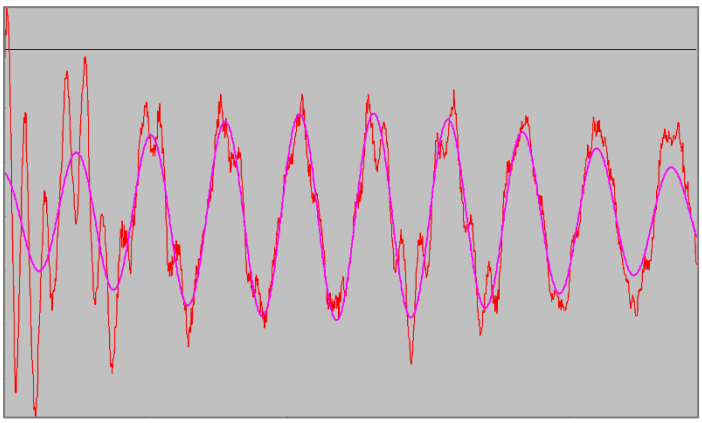

Frequency (Fourier Transform)	
0.377 THz	Dominant peak
1.470 THz	Broad
Frequency (Manual Measure)	
1.090 THz	